

DESIGN, FABRICATION, AND CHARACTERIZATION OF RECTANGULAR  
SPLIT-RING RESONATORS FOR SENSING APPLICATIONS

by

Shahrzad Zahertar

B.S., Electrical Engineering, University of Tehran, 2013

Submitted to the Institute for Graduate Studies in  
Science and Engineering in partial fulfillment of  
the requirements for the degree of  
Master of Science

Graduate Program in Electrical and Electronics Engineering  
Boğaziçi University

2016

## ACKNOWLEDGEMENTS

First and foremost, I would like to express my sincerest gratitude to my supervisor, Prof. Hamdi Torun, for his excellent guidance, patience, and continuous support throughout my Master's studies at Boğaziçi University. The door to his office was always open whenever I had a question or ran into a trouble spot about my research. I would never have been able to finish this thesis without his help and encouragements.

I would also like to thank Prof. Arda Deniz Yalçınkaya, and Prof. Onur Ferhanoğlu for taking part as committee members of my thesis defense and for their valuable comments to improve my thesis.

I would like to acknowledge The Scientific and Technological Research Council of Turkey (TÜBİTAK), which supported this work as a part of grant no. 112E250. I am also thankful to Mehmet Yumak, who helped me a lot during fabrication steps in cleanroom, to my lab mates in Bio AFM Laboratory, Sevil, Luying, Semih, and to my colleagues in Beta Lab, Ismail, and Berk who made the research more enjoyable.

Very special thanks go to my good and supportive friends Bahareh, Ida, Sina, Amir, Nader, Mohammad, Mohammad Ali, Mina, Mahsa, Varol, Deniz, and Hossein, who provided a very joyful environment for me, who were available whenever I needed help and made me feel like I am home.

Finally and most importantly, I would like to express my profound gratitude to my beloved parents and my dear sister, Anahita, for their endless support, encouragements, and unconditional love throughout my journey and I would like to dedicate this thesis to them.

## ABSTRACT

# DESIGN, FABRICATION, AND CHARACTERIZATION OF RECTANGULAR SPLIT-RING RESONATORS FOR SENSING APPLICATIONS

In this thesis, rectangular split ring resonators in microwave and terahertz frequencies are modeled, fabricated, and characterized. For microwave frequencies, rectangular split-ring resonators with one-split and two-splits are analyzed. The resonators are coupled with monopole antennas for excitation. The scattering parameters of the devices are investigated under different polarizations of  $\vec{E}$  and  $\vec{H}$  fields. The addition of the second split of the device is investigated considering different configurations of the excitation vectors. It is demonstrated that the one-split and the two-splits resonators exhibit identical transmission characteristics for a certain excitation configuration. The presented resonators can effectively function as frequency selective media for varying excitation conditions. For THz frequencies, different designs of rectangular split-ring resonators with single-split are proposed. Three types of devices are fabricated utilizing a mask. In the first type, the resonators are made of copper and are patterned on Silicon substrate. In the second type, the resonators are made of copper and are patterned on a substrate composed of a layer of parylene on a Silicon wafer. In the third type, the resonators are made of titanium and are patterned on a substrate composed of a layer of parylene on a Silicon wafer. Each type of the devices is characterized and compared to the simulation results. Bio-experiments utilizing glucose are done for one of the samples. Due to electrical properties of glucose, resonances are shifted towards higher frequencies. Devices have the potential to be utilized as biosensors.

## ÖZET

# DİKDÖRTGENSEL KESİK-HALKA REZONATÖRLERİNİN ALGILAMA UYGULAMALARI İÇİN TASARIMI, ÜRETİMİ VE KARAKTERİZASYONU

Bu tez çalışması kapsamında mikrodalga ve Terahertz frekans bantlarında çalışan kesik-halka rezonatörleri tasarlanmış, üretilmiş ve karakterize edilmiştir. Tek kesikli ve çift kesikli rezonatörler mikrodalga bandında incelenmiştir. Rezonatörler, tek-kutuplu antenlerle eşlenmiş bir şekilde tasarlanmıştır. Rezonatörlerin saçılım parametreleri elektrik ve manyetik alanın farklı polarizasyonları için incelenmiştir. Belli bir polarizasyondaki uyarılma altında, tek kesikli ve çift kesikli rezonatörlerin aynı şekilde davrandıkları gösterilmiştir. Geliştirilen kesik-halka rezonatörlerinin frekans seçici yüzeyler olarak kullanılması olasıdır.

Terahertz bandında tek kesikli, dikdörtgen şeklinde farklı kesik-halka rezonatörleri önerilmiştir. Üç farklı tipteki rezonatörler mikrofabrikasyon yöntemleri ve fotolitografi adımları kullanılarak üretilmiştir. Birinci tip cihazlar, silisyum alttaş üzerine bakır kullanılarak üretilmiştir. İkinci tip cihazlar, yine bakır kullanılarak Parylene film kaplı silisyum alttaşlar üzerinde üretilmiştir. Üçüncü tip cihazlar, Parylene film kaplı silisyum alttaşlar üzerinde titanyum kullanılarak üretilmiştir. Tüm cihazlar deneysel olarak karakterize edilmiştir ve karakterizasyon sonuçları geliştirilen modellerle karşılaştırılmıştır. Bu cihazların glukoz tespiti amacı ile kullanımları test edilmiştir. Glukoz moleküllerinin elektromanyetik özellikleri nedeniyle, cihazların rezonans frekansı glukoz moleküllerinin varlığıyla artmaktadır. Üretilen cihazların biyoalgılama uygulamaları için kullanım potansiyelleri ortaya konmuştur.

## TABLE OF CONTENTS

ACKNOWLEDGEMENTS . . . . .	iii
ABSTRACT . . . . .	iv
ÖZET . . . . .	v
LIST OF FIGURES . . . . .	viii
LIST OF TABLES . . . . .	xvi
LIST OF SYMBOLS . . . . .	xvii
LIST OF ACRONYMS/ABBREVIATIONS . . . . .	xix
1. INTRODUCTION . . . . .	1
1.1. History of Metamaterials . . . . .	3
1.2. Background and Concepts . . . . .	4
1.2.1. Electromagnetic Waves . . . . .	4
1.2.2. Index of Refraction . . . . .	8
1.2.3. Operating Frequencies of Metamaterials . . . . .	10
1.2.4. Terahertz Spectrum . . . . .	12
1.3. Contributions of This Thesis Work . . . . .	13
2. SPLIT RING RESONATORS AT MICROWAVE FREQUENCIES . . . . .	14
2.1. Structure and Design of the Resonators . . . . .	14
2.2. Experimental Characterization . . . . .	21
2.3. Discussion . . . . .	25
2.4. Summary of the Effects of Different Orientations of Electric and Magnetic Fields on the Resonators . . . . .	26
3. SPLIT RING RESONATORS AT TERAHERTZ FREQUENCIES . . . . .	28
3.1. Structure and Design of the Resonators . . . . .	28
3.1.1. Simulation Results for Sample One . . . . .	30
3.1.2. Simulation Results for Sample Two . . . . .	31
3.1.3. Simulation Results for Sample Three . . . . .	32
3.1.4. Simulation Results for Sample Four . . . . .	34
3.1.5. Simulation Results for Sample Five . . . . .	35
3.1.6. Designing the Mask . . . . .	36

3.2. Fabrication Process . . . . .	39
3.2.1. Fabrication of the First Type of the Devices: Copper Patterned on Silicon . . . . .	39
3.2.2. Fabrication of the Second Type of the Devices: Copper Patterned on Parylene and Silicon . . . . .	42
3.2.3. Fabrication of the Third Type of the Devices: Titanium Pat- terned on Parylene and Silicon . . . . .	46
3.3. Experimental Characterization . . . . .	49
3.3.1. Experiment Results for the First Type of Devices: Copper Pat- terned on Silicon . . . . .	50
3.3.2. Experimental Results for the Second Type of Devices: Copper Patterned on Parylene and Silicon . . . . .	53
3.3.3. Experimental Results for the Third Type of Devices: Titanium Patterned on Parylene and Silicon . . . . .	56
3.3.4. Bio-experiments with Glucose . . . . .	60
3.4. Discussion . . . . .	62
3.5. Future Work . . . . .	64
4. CONCLUSIONS . . . . .	65
REFERENCES . . . . .	68
APPENDIX A: LAYOUTS AND DETAILED SIMULATIONS RESULTS . . . . .	75
A.1. Detailed Simulation Results for Sample One . . . . .	78
A.2. Detailed Simulation Results for Sample Two . . . . .	82
A.3. Detailed Simulation Results for Sample Three . . . . .	86
A.4. Detailed Simulation Results for Sample Four . . . . .	90
A.5. Detailed Simulation Results for Sample Five . . . . .	92

## LIST OF FIGURES

Figure 1.1.	The coordinate system for permittivity and permeability [28]. . . .	7
Figure 1.2.	An illustration of the coordinate system in a) right-handed materials b) left-handed materials. . . . .	8
Figure 1.3.	a) an illustration of positive and negative refraction b) negative refraction c) positive refraction . . . . .	9
Figure 1.4.	The structure of a circular split-ring resonator. . . . .	10
Figure 2.1.	The schematic of the proposed device. . . . .	14
Figure 2.2.	a) s21 spectrum of the single-split resonator for the excitation setting shown in the figure. b) Distribution of the current density at the first resonance of 0.65 GHz. c) Distribution of the electric field at the second resonance of 3.28 GHz . . . . .	15
Figure 2.3.	a) s21 spectrum of the single-split resonator for the related excitation setting. Distribution of current densities at b) the first resonance of 0.61 GHz and c) at the second of 1.14 GHz. d) Distribution of electric field at the third resonance of 3.73 GHz. . . .	16
Figure 2.4.	a) s21 spectrum of the single-split resonator for the excitation setting shown in the figure. b) Distribution of current density at the first resonant frequency of 1.86 GHz c) Distribution of electric field at the second resonant frequency of 4.73 GHz. . . . .	17

Figure 2.5.	a) s21 spectrum of the single-split resonator for the excitation setting shown in the figure. b) Distribution of current density at the first resonance of 0.81 GHz. Distributions of electric field at c) the second resonance of 2.59 GHz and d) at 3.77 GHz. . . . .	18
Figure 2.6.	s21 spectra of the single-split resonator for different orientations of the electric field. . . . .	20
Figure 2.7.	a) s21 spectrum of the two-splits resonator for the excitation setting shown in the figure, compared to that of Figure 2.4. b) Distribution of current density at the first resonant frequency of 1.87 GHz. . .	21
Figure 2.8.	The experimental setup . . . . .	22
Figure 2.9.	Spectrum of s21 for a single-split resonator in an excitation setting similar to that of Figure 2.5. The measured values of resonant frequencies are 0.82 GHz, 2.1 GHz and 4.29 GHz. . . . .	23
Figure 2.10.	Spectrum of s21 for a single-split resonator in an excitation setting similar to that of Figure 2.4. The measured value of resonant frequency is 2.14 GHz. . . . .	24
Figure 2.11.	Spectrum of s21 for a two-splits resonator in an excitation setting similar to that of Figure 2.7. The measured value of resonant frequency is 2.12 GHz. . . . .	25
Figure 2.12.	Current density patterns caused by different orientations of electric and magnetic field . . . . .	27

Figure 3.1.	The schematic of the proposed devices operating at THz frequencies. (a-c) rectangular split-ring resonators, (d-c) square split-ring resonators. . . . .	29
Figure 3.2.	Simulation results of different boundary conditions for sample one.	31
Figure 3.3.	Simulation results of different boundary conditions for sample two.	32
Figure 3.4.	Simulation results of different boundary conditions for sample three.	33
Figure 3.5.	Simulation results of different boundary conditions for sample four.	34
Figure 3.6.	Simulation results of different boundary conditions for sample five.	35
Figure 3.7.	Illustration of the wafer and the dies. The wafer is filed with the randomly placed dies. $d_1$ is the distance of the short sides of the consecutive rings, and is 50 micron. $d_2$ is the distance between the long sides of two consecutive rings. . . . .	36
Figure 3.8.	a) Sample one b) Sample two c) Sample three d) Sample four e) Sample five that are patterned on the mask and their dimensions.	37
Figure 3.9.	The defects in the fabricated mask for: a) Sample one b) Sample two c) Sample three d) Sample four e) Sample five. . . . .	38
Figure 3.10.	Fabrication Process of the first type of the devices. . . . .	40
Figure 3.11.	Fabricated First Type of the Devices: a) Sample one b) Sample two c) Sample three d) Sample four e) Sample five. . . . .	41

Figure 3.12. Defects of the First Type of the Fabricated Devices: a) Sample one b) Sample two c) Sample three d) Sample four e) Sample five . . . . .	42
Figure 3.13. Fabrication process of the second and the third type of the devices.	43
Figure 3.14. Fabricated Second Type of the Devices: a) Sample one b) Sample two c) Sample three d) Sample four e) Sample five. . . . .	44
Figure 3.15. Defects of the Second Type of the Fabricated Devices: a) Sample one b) Sample two c) Sample three d) Sample four e) Sample five.	45
Figure 3.16. Fabricated Third Type of the Devices: a) Sample one b) Sample two c) Sample three d) Sample four e) Sample five. . . . .	47
Figure 3.17. Defects of the Third Type of the Fabricated Devices: a) Sample one b) Sample two c) Sample three d) Sample four e) Sample five.	48
Figure 3.18. Setup for the transmission mode of the terahertz time-domain spec- troscopy. . . . .	49
Figure 3.19. Transmission characteristics of a) dry air b) humid air and c) Si at THz frequencies [54]. . . . .	50
Figure 3.20. Experiment and simulation results of device one. Red graphs are experiment results of the samples one to five, while the blue graphs are the simulation results of the samples one to five. . . . .	52
Figure 3.21. Experiment and simulation results of device two. Red graphs are experiment results of the samples one to five, while the blue graphs are the simulation results of the samples one to five. . . . .	55

Figure 3.22. Experiment result for a device containing samples one, three, four and five. . . . .	56
Figure 3.23. Experiment result the individual samples on a device containing sample one, three, four, and five. a) experiment result of sample one. b) Experiment result of sample three. . . . .	57
Figure 3.24. Experiment results of different orientations for a device containing samples one, two, three, and four. . . . .	58
Figure 3.25. Experiment results for a device containing samples one, two, three, and four a) without and b) with the deposition of the extra layer of the paryelene. . . . .	59
Figure 3.26. Experiment results for a device containing samples one, two, three, and five. . . . .	60
Figure 3.27. Bio-experiment results for sample three. a) Raw data obtained from the THz time domain spectroscope. b) Transmission characteristics of the device. . . . .	61
Figure A.1. The layout of the designed mask. . . . .	75
Figure A.2. The layout of the dies containing sample one. . . . .	76
Figure A.3. The layout of the dies containing sample two. . . . .	76
Figure A.4. The layout of the dies containing sample three. . . . .	77
Figure A.5. The layout of the dies containing sample four. . . . .	77

Figure A.6.	The layout of the dies containing sample five. . . . .	78
Figure A.7.	a) s21 Spectrum of the sample one for the excitation setting shown in the figure. b) Distribution of current density at 1.92 THz. . . .	78
Figure A.8.	a) s21 Spectrum of the sample one for the excitation setting shown in the figure. b) Distribution of current density at 0.9 THz. c) Distribution of electric field at 2.48 THz. . . . .	79
Figure A.9.	a) s21 Spectrum of the sample one for the excitation setting shown in the figure. Distribution of current density at b) 0.8 THz and c) 1.17 THz. . . . .	80
Figure A.10.	a) s21 Spectrum of the sample one for the excitation setting shown in the figure. b) Distribution of current density at 0.9 THz. c) Distribution of electric field at 3 THz. . . . .	81
Figure A.11.	a) s21 Spectrum of the sample two for the excitation setting shown in the figure. Distribution of current density at b) 0.89 THz and c) 1.81 THz. Distribution of electric field at d) 2.32 THz and e) 2.86 THz. . . . .	82
Figure A.12.	a) s21 Spectrum of the sample two for the excitation setting shown in the figure. Distribution of current density at b) 0.89 THz and c) 1.88 THz. Distribution of electric field at d) 2.45 THz and e) 2.83 THz. . . . .	83
Figure A.13.	a) s21 Spectrum of the sample two for the excitation setting shown in the figure. Distribution of current density at b) 0.71 THz, c) 1.06 THz. Distribution of electric field at d) 2.21 THz, e) 3 THz. .	84

Figure A.14. a) s21 Spectrum of the sample two for the excitation setting shown in the figure. Distribution of current density at b) 0.87 THz and c) 2.38 THz. d) Distribution of electric field at 3 THz. . . . .	85
Figure A.15. a) s21 Spectrum of the sample three for the excitation setting shown in the figure. b) Distribution of current density at 1.87 THz. . . .	86
Figure A.16. a) s21 Spectrum of the sample three for the excitation setting shown in the figure. b) Distribution of current density at 0.85 THz. c) Distribution of electric field at 2.53 THz. . . . .	87
Figure A.17. a) s21 Spectrum of the sample three for the excitation setting shown in the figure. b) Distribution of current density at 0.77 THz. Distribution of electric field at c) 1.48 THz, d) 2.39 THz, and e) 2.8 THz. . . . .	88
Figure A.18. a) s21 Spectrum of the sample three for the excitation setting shown in the figure. Distribution of current density at b) 0.79 THz and c) 2.59 THz. . . . .	89
Figure A.19. a) s21 Spectrum of the sample four for the excitation setting shown in the figure. b) Distribution of current density at 1.79 THz. . . .	90
Figure A.20. s21 Spectrum of the sample four for the excitation setting shown in the figure. . . . .	90
Figure A.21. a) s21 Spectrum of the sample four for the excitation setting shown in the figure. b) Distribution of current density at 1.78 THz. . . .	91
Figure A.22. a) s21 Spectrum of the sample four for the excitation setting shown in the figure. b) Distribution of current density at 1.61 THz. . . .	91

Figure A.23. a) s21 Spectrum of the sample five for the excitation setting shown in the figure. b) Distribution of current density at 0.84 THz. c) Distribution of electric field at 2.79 THz. . . . .	92
Figure A.24. a) s21 Spectrum of the sample five for the excitation setting shown in the figure. b) Distribution of current density at 2.04 THz. . . .	93
Figure A.25. a) s21 Spectrum of the sample five for the excitation setting shown in the figure. b) Distribution of current density at 0.76 THz. . . .	93
Figure A.26. a) s21 Spectrum of the sample five for the excitation setting shown in the figure. b) Distribution of current density at 0.65 THz. c) Distribution of electric field at 2.27 THz. . . . .	94

## LIST OF TABLES

Table 2.1.	Summary of simulation results under different excitations . . . . .	19
------------	---	----

## LIST OF SYMBOLS

$\vec{B}$	Magnetic Flux Density
$C$	Capacitance
$C_{eff}$	Effective Capacitance
$C_{gap}$	Gap Capacitance
$C_{surf}$	Surface Capacitance
$c$	Speed of Light in Vacuum
$\vec{D}$	Electric Flux Density
$\vec{E}$	Electric Field
$f$	Resonant frequency
$f_0$	Magnetic Resonant frequency
$g$	Gap of the Ring
$\vec{H}$	Magnetic Field
$h$	Thickness of the Ring
$\vec{J}$	Current Density
$\vec{k}$	Wave or Propagation Vector
$k$	Propagation Constant
$L$	Inductance
$L_{eff}$	Effective Inductance
$n$	Refractive Index
$R$	Radius of Inner Ring
$S$	Poynting Vector
$S_{21}$	Forward Voltage Gain
$V$	Speed of Light in Medium
$w$	Width of the Ring
$\epsilon$	Permittivity
$\epsilon_0$	Free-space (Vacuum) Permittivity
$\epsilon_{eff}$	Effective or Relative Permittivity

$\mu$	Permeability
$\mu_0$	Free-space (Vacuum) Permeability
$\mu_{eff}$	Effective or Relative Permeability
$\rho$	Electric Charge Density
$\omega$	Angular Frequency

## LIST OF ACRONYMS/ABBREVIATIONS

2D	Two Dimensional
Cu	Copper
HRFZ-Si	High Resistivity Float Zone Silicon
LHM	Left-handed Material
NIM	Negative Refractive Index Material
RHM	Right-handed Material
THz-TDS	Terahertz Time Domain Spectroscopy
Ti	Titanium
VNA	Vector Network Analyzer

## 1. INTRODUCTION

Metamaterials are artificially engineered structures that can manipulate electromagnetic waves and exhibit unnatural and unique properties such as having negative values of permittivity and permeability simultaneously in a specific frequency band, resulting in negative values of index of refraction [1–3]. Metamaterials can have very simplistic designs; yet can exhibit very sharp resonances. The geometry of the metamaterials determines their resonant frequencies. Therefore, depending on the application, one can design metamaterials that can function in a specific frequency band in electromagnetic spectrum. Metamaterials have been demonstrated in a wide range of frequencies, spanning from GHz to optical frequencies [4] for various applications such as cloaking [5,6], super lenses [7,8], sub-diffraction focusing [9], perfect absorption [10], and biosensing [11–16]. Split-ring resonators (SRR) are among the basic building blocks to realize metamaterials [17]. SRRs are thin metallic rings or square loops with a split on top of a dielectric substrate. SRRs are one of the first metamaterial-based microwave resonators whose geometries are smaller than the wavelength of exciting electromagnetic waves [18].

In this thesis, rectangular split-ring resonators that operate at microwave and terahertz frequencies are presented. In section 2, the split ring resonators with single split and two-splits are modeled in microwave frequencies in the range of 0-5 GHz. Different polarizations of electric and magnetic fields are imposed to the rings resulting in different resonant frequencies and different modes of resonances. The resonators are fabricated on an FR4 substrate and then are characterized in transmission mode using a network analyzer. The behavior of the resonators for different orientations of the fields based on simulation and experimental results are explained and also the addition of the second split to the resonators is investigated. Magnetic resonances are observed where a circulating current pattern is induced along the conductor of the resonators. Circulating current is supported by a properly aligned magnetic field and this happens when magnetic field is perpendicular to the plane of the resonator or when the electric field is polarized along the gap of the resonator. Another mode of magnetic resonance

is also present in the rings when the electric field is polarized along the short sides of the rectangle. In this case, two circulating current paths in opposite directions are induced on top and bottom halves of the rectangle, creating two virtual nodes one in the gap and the other in the opposite side of the gap. Then the second split in the rectangular resonators is placed exactly in the location of the second virtual node so that the circulating current paths are not altered. Therefore, regardless of the number of the gaps in the structure of the resonator, it is shown that under a certain orientation of the fields, the transmission characteristics of split ring resonators with single split and two-splits are identical, which is counterintuitive. Based on the simulation and experimental results, we verify that the proposed devices can be utilized as frequency selective media for different excitation configurations.

In section 3, five different samples of rectangular split-ring resonators with single split that operate at terahertz frequencies are proposed. The simulation results for the resonators under different orientations of electric and magnetic fields are obtained and discussed similar to section 2. The structures are simulated using CST Studio Suite and the frequency range is 0-3 THz. Afterwards, dies consisting of arrays of each sample, and accordingly a mask on which the dies are placed randomly are designed. Three types of devices utilizing the mask are fabricated. In the first type of devices, the copper is patterned on a Silicon substrate through lift-off process. In the second type of devices, the Silicon wafer is coated with a parylene layer and the metallic rings made of copper are patterned on the substrate. In the third type of the devices, the Silicon wafer is coated with a layer of parylene and the metallic rings made of titanium are patterned on the substrate. The devices are characterized in transmission mode utilizing a terahertz time domain spectroscopy (THz-TDS). The experimental results for each sample of the first and the second types of the devices are obtained individually, however, for the third type of the devices, multiple samples are characterized simultaneously. Comparisons are made between simulation and experimental results afterwards. Since the transmission mode in the THz-TDS is used, the focus is mostly on the simulation results where the propagation vector is perpendicular to the plane of the resonators. The possible sources of errors in the case of discrepancies between simulation and experimental results are discussed.

The devices are evaluated for the application of biosensing. Biological specimens located on the surface of the resonators result in shifts in the resonant frequency of the devices and the amount of shift can be measured to assess the concentration or the quantity of the present specimen. Bio-experiments are performed for one of the samples of the second type of the devices. To get the bio-experiment, a high-concentration solution of glucose in DI water is prepared, and the sample is dipped in the solution. The sample is characterized in THz-TDS afterwards when it is dried. It is observed that the resonant frequency of the sample shifts towards higher frequencies after the application of the glucose. Experimental results show that the designed structures have the potential to be utilized effectively as biosensors if the specificity and sensitivity parameters are extracted in the future. At the end, the future work is proposed and the studies are concluded in section 4.

### 1.1. History of Metamaterials

In the last decades, there has been a great interest in the study of metamaterials. Unnatural materials regarded as metamaterials are engineered structures with simultaneously negative permeability and permittivity over a certain frequency band leading to a negative value of the refractive index. Victor Veselago was the first who introduced the theory of negative index materials in 1968 [19]. He gave descriptions of right-handed materials (RHM) and left-handed materials (LHM). He titled negative index materials as LHM because of the formed left-handed triad by electric field, magnetic field, and propagation vector. He claimed that in LHM, the Poynting vector and propagation vectors are in opposite directions and such materials support backward waves, whereas in RHM the Poynting vector is in the same direction with the propagation vector. However, since these behaviors are not readily available in natural materials, his studies were not realized experimentally over about 30 years. For the first time in 2000, D. R. Smith et al. experimentally verified the existence of metamaterials by combining 2D split-ring resonators and 2D wires based on the work of J. B. Pendry [3, 20–22]. The first fabricated metamaterials were functioning at microwave frequencies and since then the efforts have been made to design the metamaterial

in order to span the operating frequencies up to optical range of the electromagnetic spectrum.

So far, different designs have been introduced in the field of metamaterials and the most conventional ones are circular and rectangular split-ring resonators. These are investigated regarding different performance parameters such as sensitivity for sensing applications. Rectangular designs are capable of providing higher sensitivity when they are employed for sensing applications [23]. Furthermore, rectangular resonators are more suitable for miniaturization and dense packing as compared to circular structures [23]. In addition, some modifications have been introduced to conventional designs such as fabricating multi-gap rectangular or circular split-ring resonators. It is shown that additional gaps to the structures prevent magnetic resonance due to the induced current by the electric field [24–26] and also the resonant frequency usually shifts towards higher values.

## 1.2. Background and Concepts

### 1.2.1. Electromagnetic Waves

Electromagnetic wave is a transverse wave consisting of perpendicular vibrations of electric and magnetic fields that propagate with the speed of light through vacuum. In electromagnetic waves, the electric and magnetic fields are perpendicular to each other and also perpendicular to the direction of the wave propagation. The electromagnetic waves are characterized either by their frequency or their wavelength.

The basis of the study and the application of the wave propagation in a medium starts with Maxwell's equations, which show the relation between electric and magnetic fields through coupled spatial and temporal differential equations. The important issue in Maxwell's equation is the identification of the sources and the properties of the medium in the region of the interest. Sources generate waves and waves propagate through the medium and scatter between the boundaries of the different media. Therefore, to better understand the behavior of left-handed metamaterials, Maxwell's

equations are investigated. The following equations present Maxwell's equations in an isotropic medium;

$$\nabla \times E = -\frac{\partial B}{\partial t} \quad (1.1)$$

$$\nabla \times H = \frac{\partial D}{\partial t} + J \quad (1.2)$$

$$\nabla \cdot D = \rho \quad (1.3)$$

$$\nabla \cdot B = 0 \quad (1.4)$$

Where in the equations, E and H are electric and magnetic fields;  $\rho$  is the charge density and J is the current density. The values of  $\rho$  and J for a non-conducting medium are zero. D and B are electric and magnetic flux densities respectively. B and D can be written as:

$$D = \epsilon E = \epsilon_{eff} \epsilon_0 E \quad (1.5)$$

$$B = \mu H = \mu_{eff} \mu_0 H \quad (1.6)$$

Where  $\epsilon$  is the electrical permittivity,  $\epsilon_{eff}$  is the effective or relative permittivity,  $\epsilon_0$  is permittivity in the vacuum with the value of  $8.854 \times 10^{-12}$  farads/meter,  $\mu$  is the magnetic permeability,  $\mu_{eff}$  is the effective relative permeability, and  $\mu_0$  is the permeability in the vacuum with the value of  $4\pi \times 10^{-7}$  henrys/meter.

By replacing the  $\partial/\partial t$  with  $j\omega$ , and inserting the equation 1.5 and 1.6 into the equations 1.1 and 1.2, the mentioned equations can be rewritten as:

$$\nabla \times E = -j\omega\mu H \quad (1.7)$$

$$\nabla \times H = j\omega\epsilon E \quad (1.8)$$

Taking the curl of equation 1.1 and using the equation 1.2,  $B$  can be eliminated as shown in equation 1.9.

$$\nabla \times (\nabla \times E) = -\frac{\partial(\nabla \times B)}{\partial t} = -\mu\epsilon\frac{\partial^2 E}{\partial t^2} \quad (1.9)$$

On the other hand, using vector identities and extracting the curl of the curl for a vector, the equation below is valid for a given vector,  $A$ :

$$\nabla \times (\nabla \times A) = \nabla(\nabla \cdot A) - (\nabla^2 A) \quad (1.10)$$

Using equation 1.10 and inserting equation 1.9 into it can extract equation 1.11 for electric field;

$$-\mu\epsilon\frac{\partial^2 E}{\partial t^2} = \nabla(\nabla \cdot E) - (\nabla^2 E) \quad (1.11)$$

By inserting equation 1.3 for a non-conducting medium and replacing the  $\partial/\partial t$  with  $j\omega$ , equation 1.11 is rewritten as equation 1.12:

$$\nabla^2 E + \omega^2\mu\epsilon E = 0 \quad (1.12)$$

The wave vector,  $k$ , is then defined as:

$$k = \omega\sqrt{\epsilon\mu} \quad (1.13)$$

In order for electromagnetic waves to propagate through a medium, the real parts of the permittivity and permeability should have the same algebraic sign [19,27]. Therefore, electromagnetic waves will propagate in a medium where both of the effective permittivity and permeability are either positive or negative at the same time. In other words, the propagation of the wave will not happen in a medium where the permittivity and permeability are of the opposite algebraic sign. Whenever effective permittivity and permeability are negative simultaneously over a certain frequency band for a material, a left-handed triad of electric field, magnetic field, and wave vector is formed and the material is considered to be a left-handed material. However, the material is regarded as right-handed material whenever both of the effective permittivity and permeability are positive. Figure 1.1 shows the coordinate system for permittivity and permeability [28].

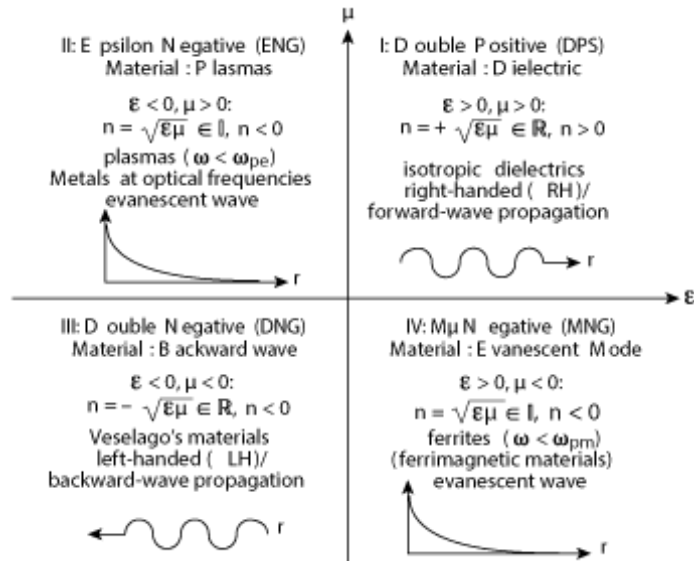


Figure 1.1. The coordinate system for permittivity and permeability [28].

The power transferred per unit area is known as Poynting vector and is defined as:

$$S = E \times H \quad (1.14)$$

Regardless of the signs of the permittivity and permeability, the Poynting vector always forms a right-handed coordinate system together with electric and magnetic fields. Therefore, in a left-handed material the propagation vector and the Poynting vectors are in opposite directions and the wave is considered to be a backward wave. However, in a right-handed material, the propagation vector is in the same direction with the Poynting vector and the wave is called as forward wave. Figure 1.2 presents the coordinate system for the LHM and RHM.

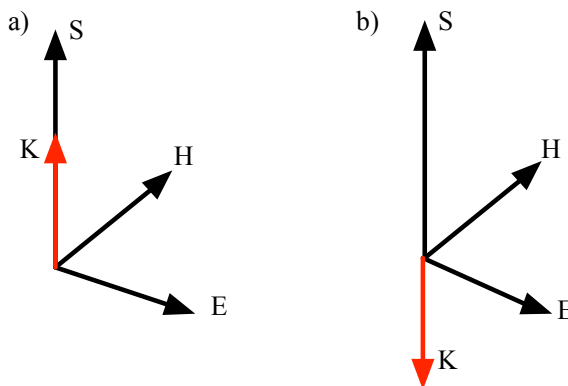


Figure 1.2. An illustration of the coordinate system in a) right-handed materials b) left-handed materials.

### 1.2.2. Index of Refraction

Velocity of light in the vacuum,  $c$ , and in the medium,  $V$ , is defined based on Maxwell's theoretical treatment as equations 1.15 and 1.16 respectively:

$$c = \frac{1}{\sqrt{\epsilon_0 \mu_0}} \quad (1.15)$$

$$V = \frac{1}{\sqrt{\epsilon\mu}} \quad (1.16)$$

The absolute refractive index is defined accordingly as equation 1.17:

$$n = \frac{c}{V} = \pm(\sqrt{\epsilon_{eff}\mu_{eff}}) \quad (1.17)$$

The sign in the equation 1.17 is to indicate the sign of the wave vector. If both values of the permittivity and permeability are positive, the refractive index will be positive. However, in a left-handed material where the values of the permittivity and permeability are negative simultaneously, the sign of the refractive index will be negative.

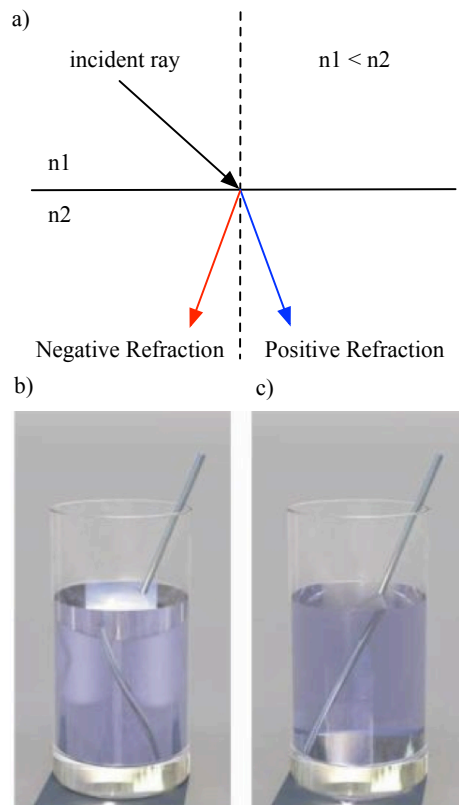


Figure 1.3. a) an illustration of positive and negative refraction b) negative refraction  
c) positive refraction

The reflection and refraction phenomena in the interface of two different materials with different dielectric constants are explained based on Snell's law. Figure 1.3 indicates the behavior of a negative refractive index material (NIM).

### 1.2.3. Operating Frequencies of Metamaterials

The resonant frequency and the resonance intensity are the most important parameters of a metamaterial which determine the working bandwidth and the performance of the metamaterial structure respectively. However, these parameters are not investigated systematically and thoroughly up to now. So far, the most widely used model for metamaterials is LC-resonance circuit model, however it only takes into account the fundamental resonant frequency and does not give information about higher order resonances that appear in the simulation and experimental results. LC-resonance circuit model do not predict the related intensities for different metamaterials either [29,30]. Other models that can be used to predict higher order frequencies include Mie resonance model [31], plasmonic resonance model [32], and high order harmonic model [33]. In this part, LC-resonance model is investigated for split-ring resonators. The shape of the structures can be circular or rectangular, however, the gap is common in their design. The designs can be modeled as lumped elements. Since these elements are dependent on the dimensions of the structures, therefore by changing the scaling, the fundamental operating frequency will change. Equations below indicate the relationship between the geometry of the design and the magnetic frequency in a circular split ring resonator [14,18]. The structure of the device is shown in Figure 1.4.

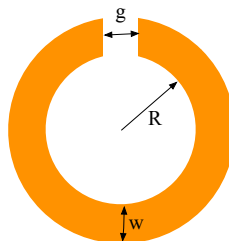


Figure 1.4. The structure of a circular split-ring resonator.

The fundamental frequency of the proposed circular SRR is defined in equation 1.18 where  $f_0$  is the magnetic resonant frequency of the device,  $L_{eff}$  is the effective inductance and  $C_{eff}$  is the effective capacitance of the ring.  $C_{eff}$  is composed of two parts; the capacitance of the gap,  $C_{gap}$ , and the surface capacitance  $C_{surf}$ .  $R$  is the radius of the ring,  $h$  is the thickness of the ring,  $w$  is the width of the ring, and  $g$  is the gap of the ring [14,18].

$$f_0 = \frac{1}{2\pi\sqrt{L_{eff}C_{eff}}} \quad (1.18)$$

$$L_{eff} = \mu_0 R_m \left( \log\left(\frac{8R_m}{h+w}\right) - \frac{1}{2} \right) \quad (1.19)$$

where

$$R_m = R + \frac{w}{2} \quad (1.20)$$

and

$$C_{eff} = C_{gap} + C_{surf} \quad (1.21)$$

$$C_{gap} = \epsilon_{eff} \frac{hw}{g} + \epsilon_{eff}(h+w+g) \quad (1.22)$$

$$C_{surf} = \frac{2\epsilon_{eff}(h+w)}{\pi} \left( \log \frac{4R}{g} \right) \quad (1.23)$$

The value of the magnetic resonant frequency for other similar designs can be roughly calculated according to equation 1.18 for the case where the magnetic field is perpendicular to the plane of the ring and a circulating current path is induced in the ring. The equations of the inductance and capacitance will be different based on the

design of the split-ring resonators. Also it should be taken into account that many of the various designs do not have analytical expressions in the literature. As a result, the frequencies of the resonators are mostly obtained by numerical simulations.

#### 1.2.4. Terahertz Spectrum

Terahertz radiation relates to a part of electromagnetic spectrum, which lies between microwave and infrared wavelengths. The wavelength corresponding to this regime is 1000-30  $\mu\text{m}$  and the frequency is ranging from 300 GHz to 3 THz [34]. Historically, sub-millimeter or THz radiation is referred to as THz gap since traditional electronic and optical devices do not operate efficiently at these frequency ranges. For example, electronic radiation sources such as crystal oscillators generally operate at frequencies below 100 GHz, while laser radiation sources are generally confined to operate at frequencies above 30 THz [35]. However, THz waves have unique and very valuable specifications that make it suitable for various applications like spectroscopy, sensing, and imaging [36–38]. THz radiation has non-ionizing nature when compared to x-rays. Therefore, devices operating at THz frequencies are harmless to human beings and can be safely used for biomedical imaging purposes [39]. Although designing and fabricating structures in microwave frequencies are more feasible, THz radiation has the ability to resolve details that overmatch the corresponding resolution from sensors functioning in microwave frequencies [40]. In addition, THz radiation can penetrate most dry, non-metallic, non-polar materials. Therefore, variety of imaging and spectroscopy applications in terahertz band has been increasing rapidly for security purposes including detection of explosives, surveillance or quality control purposes [36, 41–46]. On the other hand, since water content in the atmosphere attenuates THz radiation, it restricts its utilization in radio communication systems. However, applications such as medical imaging exploit THz band, relying on the difference in absorptivity between normal and cancer cells [47–49]. Considering the merit of the THz band, it is essential to develop devices functioning in this regime. There has been significant improvement on metamaterial designs for terahertz applications [40, 50–52].

### 1.3. Contributions of This Thesis Work

- The effects of different excitation configurations on rectangular split-ring resonators are investigated.
- It is shown that rectangular split-ring resonators with one-split and two-split can have identical behaviors under a certain excitation condition, which is counterintuitive.
- The presented split-ring resonators at microwave frequencies can effectively function as frequency selective media for varying excitation conditions.
- The proposed designs operating at THz frequencies have the potential to be utilized as biosensors.

## 2. SPLIT RING RESONATORS AT MICROWAVE FREQUENCIES

### 2.1. Structure and Design of the Resonators

The device is composed of a 35  $\mu\text{m}$ -thick metallic rectangular loop on a 0.8 mm thick FR-4 substrate as shown schematically in Figure 2.1. Two types of devices are defined with a single split (Figure 2.1(a)) and two splits (Figure 2.1(b)). Side  $A$  and side  $B$  of the outer rectangle are 30 and 60 mm, respectively. The width,  $w$ , of the loop is 6 mm and the gap of the split,  $g$ , is 2 mm. The resonators are modeled with different

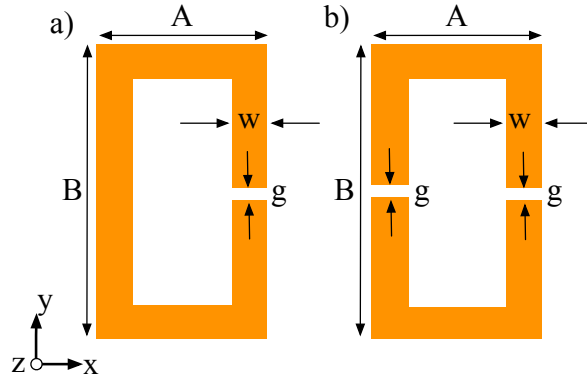


Figure 2.1. The schematic of the proposed device.

boundary conditions using commercially available electromagnetic simulation software (CST Studio Suite, Darmstadt Germany). First, the wave vector,  $\vec{k}$ , is aligned with the x-axis (see Figure 2.1), electric field ( $\vec{E}$ ) and magnetic field ( $\vec{H}$ ) vectors are aligned with the y-axis and the z-axis, respectively. The results of the simulation for the single-split resonator are shown in Figure 2.2. Magnetic field is perpendicular to the loop, so it supports circulating current along the conductive path. In addition, electric field is polarized along the gap that also contributes a circulating current. The combined effect results in the first resonant frequency, which can be identified as magnetic resonance at 0.65 GHz. The vectors for current density at this frequency are shown in Figure 2.2(b). The second resonant frequency is observed at 3.28 GHz, which is identified as

an electric resonant frequency due to the electric field aligned along the side B of the resonator. The distribution of the electric field at this frequency is shown in Figure 2.2(c).

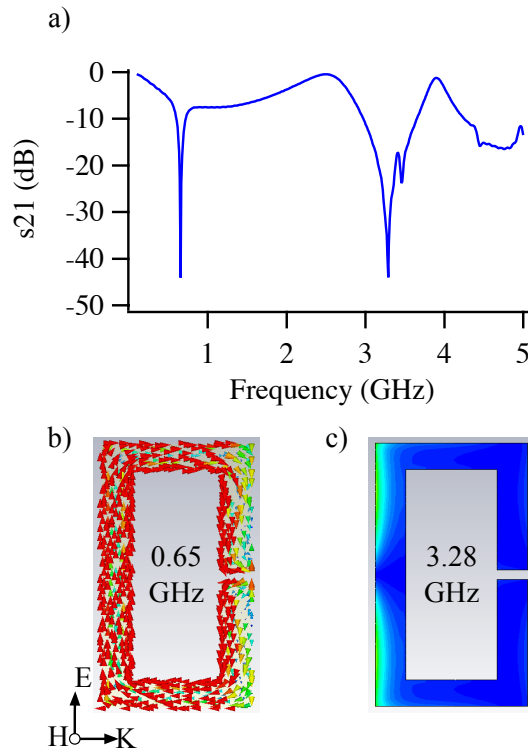


Figure 2.2. a)  $s_{21}$  spectrum of the single-split resonator for the excitation setting shown in the figure. b) Distribution of the current density at the first resonance of 0.65 GHz. c) Distribution of the electric field at the second resonance of 3.28 GHz

In the second setting,  $\vec{E}$  is aligned with the x-axis,  $\vec{k}$  and  $\vec{H}$  are aligned with the y-axis and the z-axis, respectively. The resultant spectrum of  $s_{21}$  for the single-split resonator is shown in Figure 2.3(a). In this case, magnetic field is perpendicular to the loop similar to the previous setting. This results in a resonant behavior that supports a circulating current along the conducting path. Consequently, the first resonant frequency is observed at 0.61 GHz and the current field distribution for this resonance is plotted in Figure 2.3(b). The first resonant frequency for this setting is almost the same with the one for the first setting. However, the electric field is now along the x-axis and is polarized along the side A of the resonator. This supports a certain

circulating current pattern as will be explained for the third setting (see Figure 2.4). The magnetic resonance is induced due to the combinatory effect of the electric and the magnetic field. The resonant frequency is 1.14 GHz, for which a density of current vectors as shown in Figure 2.3(c). So, changing the polarization of the electric field and the propagation vector results in an additional magnetic resonance. The third resonant frequency is due to electric resonance at 3.73 GHz. At this frequency, the electric field is aligned along with the side A of the resonator as shown in Figure 2.3(b).

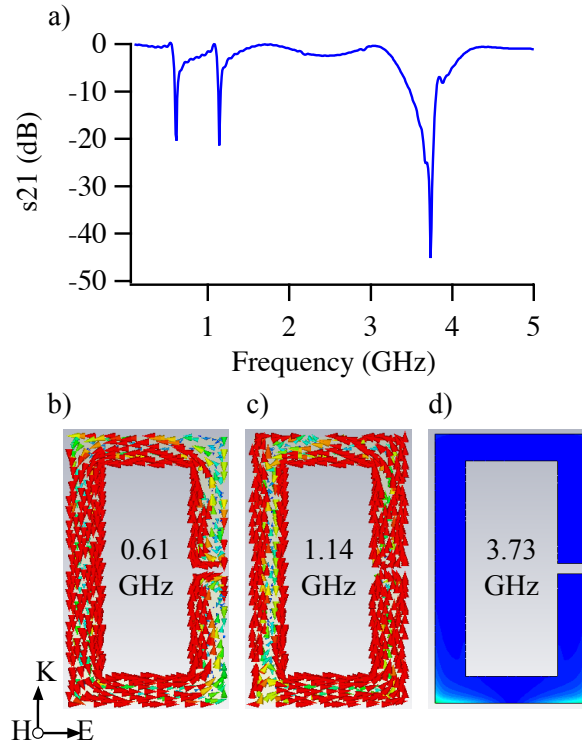


Figure 2.3. a)  $s_{21}$  spectrum of the single-split resonator for the related excitation setting. Distribution of current densities at b) the first resonance of 0.61 GHz and c) at the second of 1.14 GHz. d) Distribution of electric field at the third resonance of 3.73 GHz.

In the third setting,  $\vec{E}$  is aligned with the x-axis,  $\vec{H}$  and  $\vec{k}$  are aligned with the y-axis and the z-axis, respectively. The results of the simulation for the single-split resonator are shown in Figure 2.4. Unlike the previous settings, the magnetic field is not perpendicular to the loop. Thus, a circulating current stemming from the magnetic

field is not expected in this case. However, the electric field is polarized along the side A of the device. Left and right hand sides of the structure are polarized with opposite charges at resonance and the presence of the split defines a symmetry axis along the x-axis through the split. This results in two identical circulating current loops in opposite directions in the upper and lower halves of the resonator as shown in Figure 2.4(b). The rectangular shape of the resonator and relatively short length of side A support the circulation of the current paths shown in Figure 2.4(b). The lengths of the current loops are shorter as compared to the previous cases. Thus, the resonant frequency for the magnetic resonance is higher at 1.86 GHz. The second resonant frequency of 4.73 GHz is due to the electric resonance as a result of electric field along with the side A of the resonator.

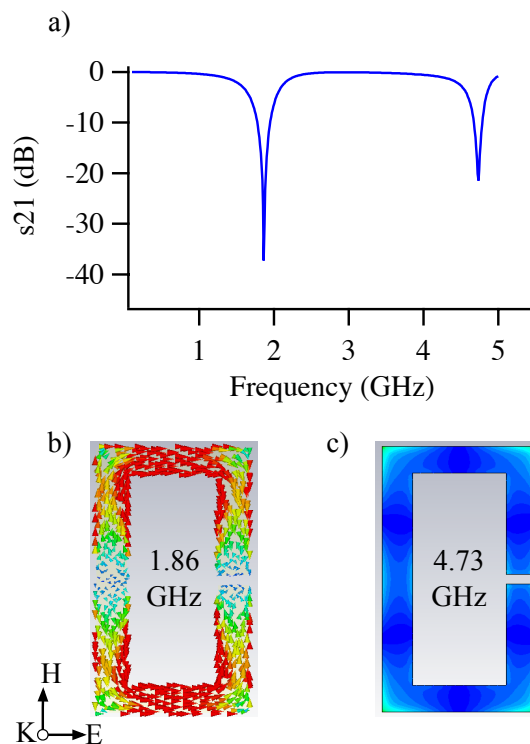


Figure 2.4. a)  $s_{21}$  spectrum of the single-split resonator for the excitation setting shown in the figure. b) Distribution of current density at the first resonant frequency of 1.86 GHz c) Distribution of electric field at the second resonant frequency of 4.73 GHz.

In the fourth setting,  $\vec{H}$  is aligned with the x-axis,  $\vec{E}$  and  $\vec{k}$  are aligned with the y-axis and the z-axis, respectively. The results of the simulation for a single-split resonator are shown in Figure 2.5. Similar to the third setting, the magnetic field is not perpendicular to the device. So, circulating current along the loop is not expected due to the magnetic field. However, the electric field is polarized along the split, inducing a single path of circulating current in the loop. The resonant frequency of this magnetic resonance is 0.81 GHz for which the distribution of current vectors is shown in Figure 2.5(b). The first resonant frequency is 25% larger than the one obtained for the case of magnetic field that is perpendicular to the loop (the first and the second settings), because of the smaller length of the equivalent conductor path as observed in Figure 2.5(b). The second and the third resonant frequencies are due to electric resonances. The distributions of the electric field for the electric resonances are shown in Figure 2.5(c-d).

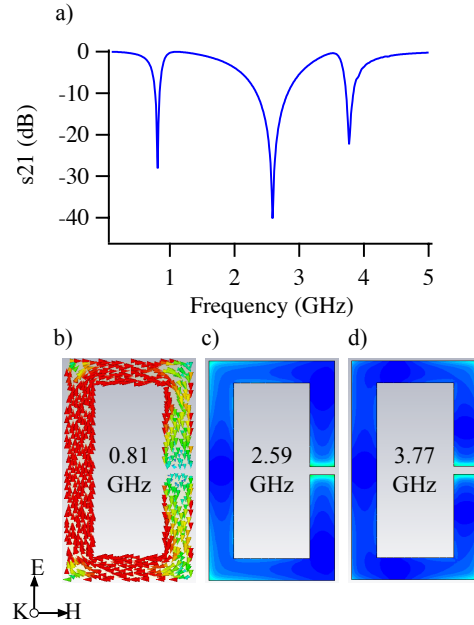


Figure 2.5. a)  $s_{21}$  spectrum of the single-split resonator for the excitation setting shown in the figure. b) Distribution of current density at the first resonance of 0.81 GHz. Distributions of electric field at c) the second resonance of 2.59 GHz and d) at 3.77 GHz.

All the simulation results obtained for the single-split resonator under different excitations are summarized in Table 2.1. The orientation for E, H and k vectors are defined with respect to the coordinate axes and device orientation defined in Figure 2.1.

Table 2.1. Summary of simulation results under different excitations

<b>Orientation</b>	<b>1<sup>st</sup> Resonance</b>	<b>2<sup>nd</sup> Resonance</b>	<b>3<sup>rd</sup> Resonance</b>	<b>Figure</b>
<b>k:x, E:y, H:z</b>	0.65 GHz	3.28 GHz	-	Figure 2.2
<b>E:x, k:y, H:z</b>	0.61 GHz	1.14 GHz	3.73 GHz	Figure 2.3
<b>E:x, H:y, k:z</b>	1.86 GHz	4.73 GHz	-	Figure 2.4
<b>H:x, E:y, k:z</b>	0.81 GHz	2.59 GHz	3.77 GHz	Figure 2.5

Figure 2.6 shows the dependency of the resonant behavior to the orientation of the electric field. Inset to the Figure 2.6, an angle  $\theta$  is defined between the electric field and the side B of the resonator. An angle of zero degrees corresponds to the case of fourth setting (see Figure 2.5) whereas an angle of ninety degrees corresponds to the case of third setting (see Figure 2.4). The first and the second resonant frequencies shown in Figure 2.6 correspond to the magnetic resonances as explained before. The third resonant frequency corresponds to the electric resonance. The magnetic resonances are induced based on the presence of the electric field vector along the x-axis and the y-axis (see Figure 2.1). For the extreme angles of zero and ninety, the electric field is aligned either along the y-axis or the x-axis. So, only one of the magnetic resonances is excited. On the other hand, for an oblique angle, the electric field has components on both axes that results in magnetic resonance at both frequencies. The resonant frequencies for magnetic resonances are the same for different orientations of the incident. A slight variation in the second resonant frequency has been observed due to a change in the conduction path that is determined by the electric field vector along the x-axis. On the other hand, the electric resonant frequency is varying with the angle as observed in Figure 2.6. The frequency shifts with the effective conductor length along the direction of electric field vector. The effective conductor length is the shortest for the angle of

zero and this corresponds to the largest resonant frequency.

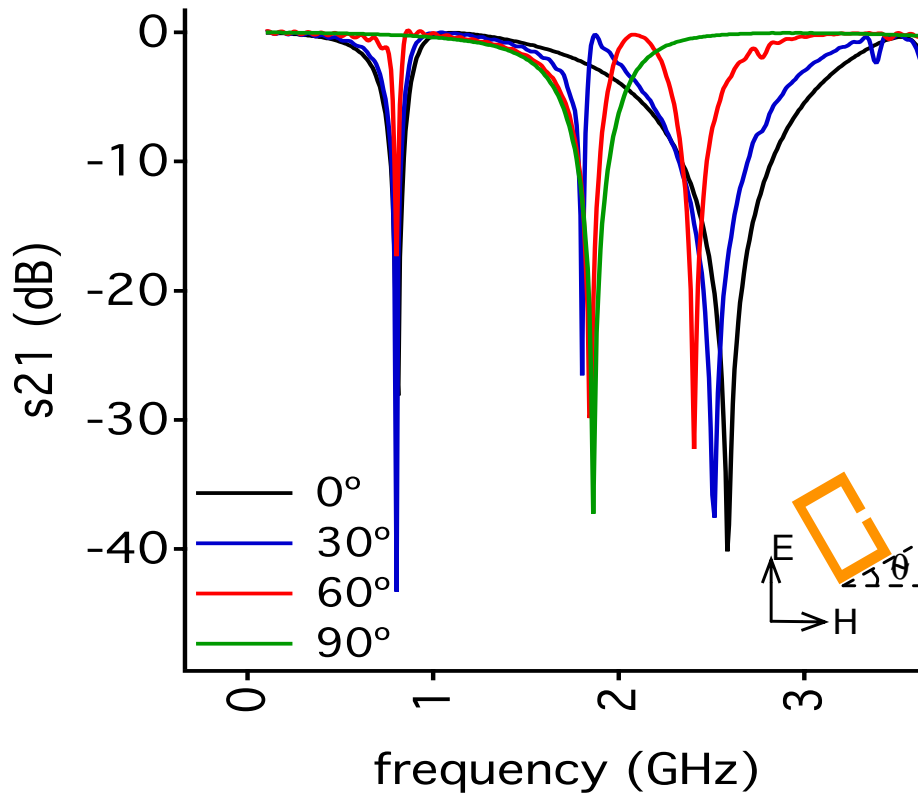


Figure 2.6.  $s_{21}$  spectra of the single-split resonator for different orientations of the electric field.

In the fifth setting, two-splits resonator (see Figure 2.1(b)) was simulated. The resultant spectrum of  $s_{21}$  for the two-splits resonator is shown in Figure 2.7(a) for a case where  $\vec{E}$  is aligned with the x-axis while  $\vec{H}$  and  $\vec{k}$  are aligned with the y-axis and the z-axis, respectively. The magnetic field is not perpendicular to the resonator, preventing the occurrence of magnetic resonance due to a circulating current. On the other hand, the electric field is along with the side A of the device. The settings of the field vectors are the same with the third case presented in Figure 2.4. The first resonant frequency is at 1.87 GHz and the resultant distribution of current vectors is shown in Figure 2.7(b). The frequency and the distribution of current vectors are identical with the results presented in Figure 2.4. It is surprising to observe an identical response for a two-

splits device as compared to a single-split one considering the first resonant frequency. The resonators are functionally identical considering the electric field polarization. The electric field supports two paths of circulating current in opposite directions in bottom and top halves of both resonators. Hence, two virtual nodes are defined along the x-axis passing through the split, regardless of the number of splits as verified in Figure 2.4(b) and Figure 2.7(b).

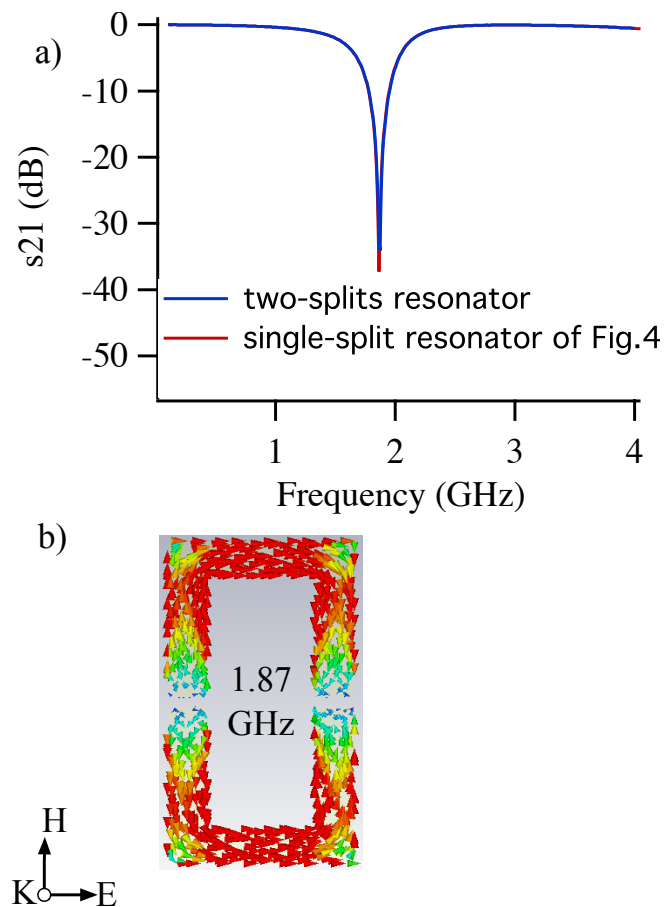


Figure 2.7. a)  $s_{21}$  spectrum of the two-splits resonator for the excitation setting shown in the figure, compared to that of Figure 2.4. b) Distribution of current density at the first resonant frequency of 1.87 GHz.

## 2.2. Experimental Characterization

The resonators were fabricated on an FR4 substrate with a thickness of 0.8 mm utilizing standard printing circuit board manufacturing techniques. The thickness of

the metal lines is  $35 \mu\text{m}$ . A pair of monopole patch antennas was used with a length of 30 mm and a width of 3.5 mm to excite the resonators. The distance between two antennas is 10 cm. The resonators and the antennas were placed on an aluminum back plate, which was used as a ground plane. The antennas were connected a vector network analyzer (Rohde and Schwarz, Munich, Germany) to obtain the transmission parameters. The setup is shown in Figure 2.8. In this orientation, the propagation vector,  $\vec{k}$ , is along the short sides of the rectangle as shown in the figure.

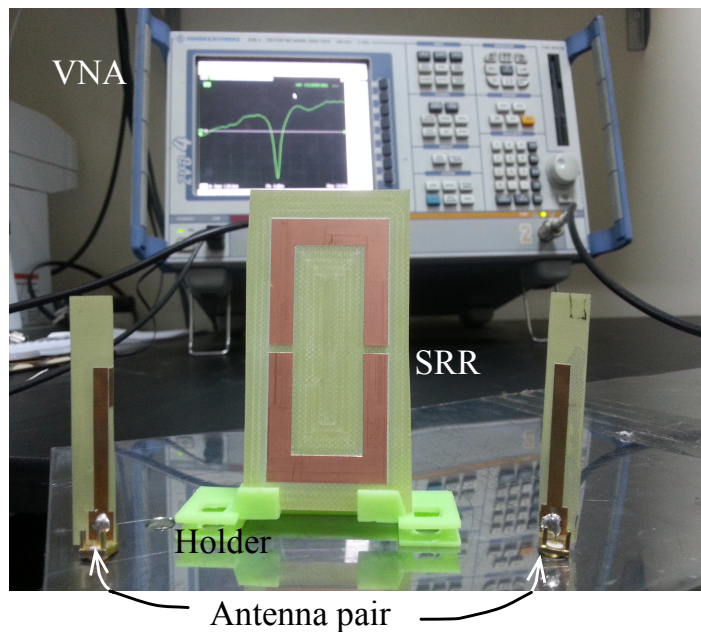


Figure 2.8. The experimental setup

The antennas have omnidirectional radiation pattern. Therefore, the location and the orientation of the resonators between the antennas can be adjusted to excite the resonators in a desired setting. Figure 2.9 shows the spectrum of  $s_{21}$  for the single-split resonator in a certain configuration where the excitation is the same with the case explained in Figure 2.5. The simulated  $s_{21}$  spectrum of Figure 2.5 is also plotted in Figure 2.9 for convenience. The measured values of the resonant frequencies are 0.82 GHz, 2.1 GHz and 4.29 GHz. The first resonant frequency is due to the magnetic resonance because of the electric field that is polarized along the gap of the

device. The measured value is 1% larger than the simulation result. The second and the third resonant frequencies are due to the electric resonance as explained before. The measured value for the second resonant frequency is smaller than the simulation result by 19%, whereas the measured value for the third resonant frequency is higher than the simulation result by 14%.

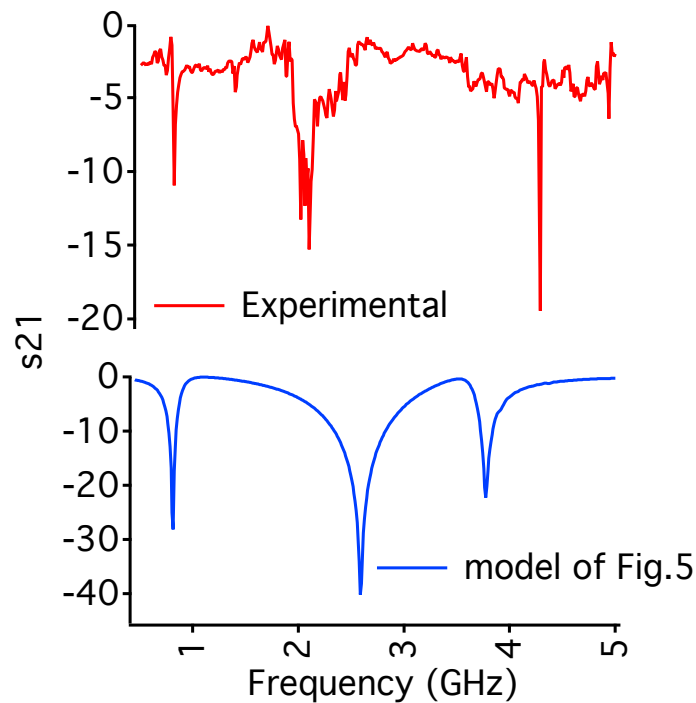


Figure 2.9. Spectrum of  $s_{21}$  for a single-split resonator in an excitation setting similar to that of Figure 2.5. The measured values of resonant frequencies are 0.82 GHz, 2.1 GHz and 4.29 GHz.

Then, the orientation of the single-split resonator was changed to have the electric field aligned with side A similar to the case explained in Figure 2.4. Figure 2.10 shows the spectrum of  $s_{21}$  in this configuration. The simulated  $s_{21}$  spectrum of Figure 2.4 is also plotted in Figure 2.10 for convenience. A single resonance within 0-4 GHz range at 2.14 GHz was observed. This corresponds to the magnetic resonance due to the electric field along side A. The measured value of the resonant frequency is larger than the simulation result by 15%.

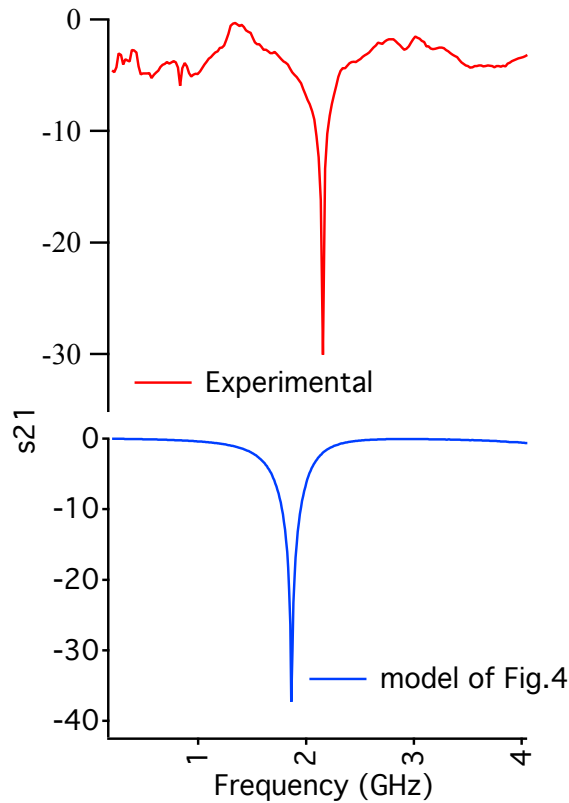


Figure 2.10. Spectrum of  $s_{21}$  for a single-split resonator in an excitation setting similar to that of Figure 2.4. The measured value of resonant frequency is 2.14 GHz.

This measurement configuration for the two-splits resonator was repeated and a very similar spectrum of  $s_{21}$  as compared to the single-split device of Figure 2.10 was observed. The spectrum is shown in Figure 2.11 with a single resonance at 2.12 GHz. This value is larger than the simulation result of Figure 2.7 by 13%. The simulated  $s_{21}$  spectrum of Figure 2.7 is also plotted in Figure 2.11 for convenience. The experimental results verify the resonance behavior of the single-split and two-splits resonators are the same for the specific excitation configuration shown in Figure 2.4 and 2.7.

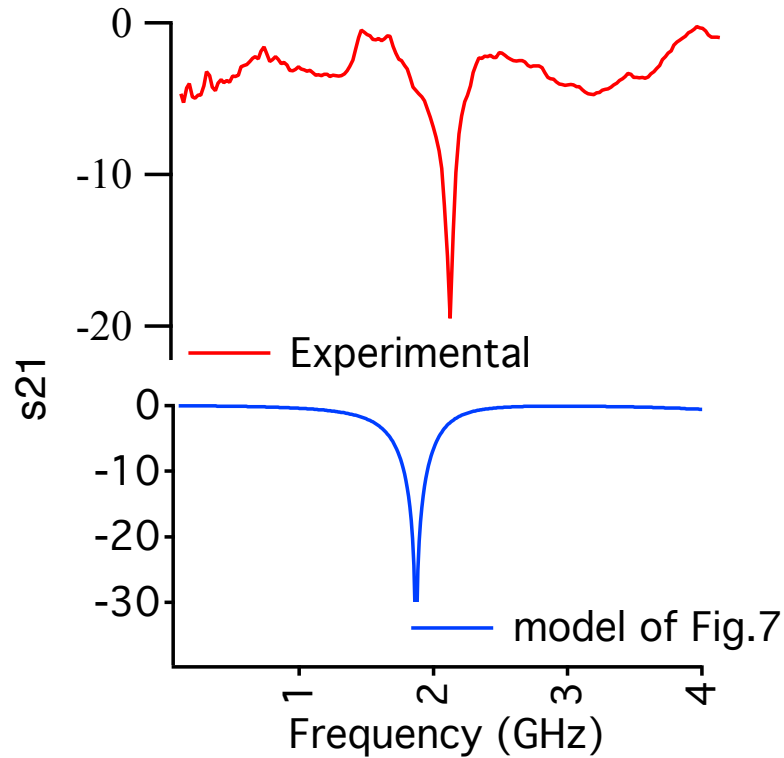


Figure 2.11. Spectrum of  $s_{21}$  for a two-splits resonator in an excitation setting similar to that of Figure 2.7. The measured value of resonant frequency is 2.12 GHz.

### 2.3. Discussion

An important conclusion of this section as mentioned previously is that the two-split and one-split rectangular rings can have identical behaviors under specific  $\vec{E}$  field polarization. It can be inferred from Figure 2.4 and Figure 2.7 that electric field generates two circulating current paths on top and bottom halves of the rings and thus generating two virtual nodes on long sides (side B, see Figure 2.1) of each rectangle. So, the first resonant frequency, which is due to magnetic resonance, is the same for both devices regardless of the number of splits. The experimental characteristics of these devices are presented in Figure 2.10 and Figure 2.11, which show the experimental results are in a good agreement with simulation results.

The discrepancies between resonant frequencies in experimental results and simulation results vary from 1% in the case of magnetic resonant frequencies to 19% in the case of second electric resonance in Figure 2.9. The possible sources of errors include the possibility of slight geometrical differences between the fabricated rings and the simulated ones. Specifically, differences in the effective path length shown in Figure 2.5(c) and 2.5(d) between the simulated and experimentally characterized devices can result in a discrepancy between electric resonances as observed in Figure 2.9.

Monopole antennas have been used since they allow us to control different excitations in a single setup by manipulating the position of the devices. Also, these compact antennas can be effectively coupled with the devices. However, because of omnidirectional radiation paths of these antennas, it is difficult to have control in a very strict sense over the orientations of  $\vec{E}$  and  $\vec{H}$  fields and this contributes to the minor divergence between the simulation and experimental results. In addition, it has been observed that the resonant dips in simulations are generally sharper than the ones in experimental results indicating that the fabricated rings are lossier than the models used in simulation settings.

#### 2.4. Summary of the Effects of Different Orientations of Electric and Magnetic Fields on the Resonators

Figure 2.12 shows the current density patterns caused by different orientation of electric and magnetic fields. When the magnetic field,  $\vec{H}$ , is perpendicular to the plane of the resonator, a circulating current path is generated through the ring as shown in Figure 2.12(a) and the generated resonant frequency is magnetic. This is the same case where the electric field,  $\vec{E}$ , is polarized along the long sides of the rectangle. As shown in Figure 2.12(b), circulating current path is generated due to  $\vec{E}$  being polarized along the gap and the resonant frequency is magnetic. In Figure 2.12(c), the electric field is polarized along the short sides of the rectangle and induces two circulating current paths in opposite directions in top and bottom halves of the rectangle. The circulating current paths and also the conduction lengths in Figure 2.12(c) are smaller than the circulating current path and the conduction lengths in Figure 2.12(b). Therefore,

the magnetic and electric resonant frequencies caused by the electric field would shift towards higher frequencies.

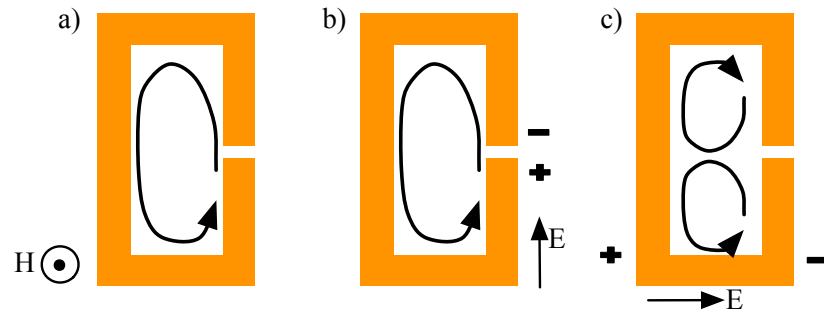


Figure 2.12. Current density patterns caused by different orientations of electric and magnetic field

### 3. SPLIT RING RESONATORS AT TERAHERTZ FREQUENCIES

As previously mentioned in the introduction section, THz regime has very unique and valuable properties that make it very flourishing. The THz technology has various applications in spectroscopy, imaging, and sensing. Due to its non-ionizing nature, the devices operating at this range are harmless to human beings and can be safely used for biomedical purposes. In addition, most of the materials have unique fingerprints in this frequency band. Since, the THz technology is flourishing, the aim of this part of the thesis is to design the devices that can operate at this regime. In this section, different designs of rectangular split-ring resonators operating in THz band are proposed, simulated, fabricated and characterized. The goal is to design the resonators that can function in 0-3 THz range because of the limitation of the THz time domain spectroscope. Scaling down the rectangular split-ring resonators with one split, which is presented in Section 2, to obtain the higher resonant frequencies is the starting point. An asymmetry is also introduced to the rings to analyze its effect. To reduce the possible coupling between two sides of the rectangle, the gap is placed in the short sides of the rectangle in one of the designs. The simplest type of rectangular resonators, square resonators, is proposed as well.

#### 3.1. Structure and Design of the Resonators

Five types of rectangular devices with single split are introduced in this part as shown in Figure 3.1.

In sample one, two, and three shown in Figure 3.1 (a-c), side A and side B of the outer rectangle are 25 and 75  $\mu\text{m}$  respectively. The width of the loop,  $w$ , and the gap of the split,  $g$ , is 5  $\mu\text{m}$  for each one. In sample one in Figure 3.1 (a), the gap is placed at the center of long side of the rectangle B1. In sample two in Figure 3.1 (b), the gap defines an asymmetry in side B2 of the rectangle and, C, the distance of

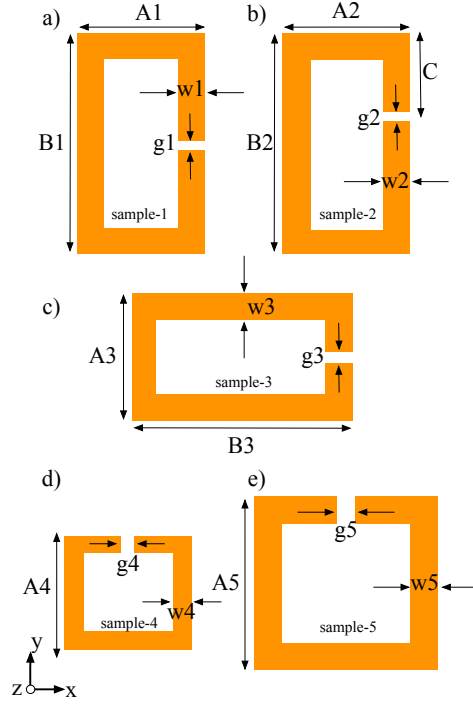


Figure 3.1. The schematic of the proposed devices operating at THz frequencies. (a-c) rectangular split-ring resonators, (d-e) square split-ring resonators. .

the center of the gap to the upper part of the rectangle is  $25 \mu\text{m}$ . In sample three in Figure 3.1 (c), the gap is defined in the short side of the rectangle  $A3$ . Sample four and five in Figure 3.1 (d) and (e) are square structures with the sides of  $25$  and  $50 \mu\text{m}$  respectively. The width of the sample four,  $w4$ , is  $2.5$  and the width of the sample five,  $w5$ , is  $5 \mu\text{m}$ . The gap of both devices is  $5 \mu\text{m}$ .

The split ring resonators were modeled using commercially available electromagnetic simulation software (CST Studio Suite, Darmstadt, Germany). Different boundary conditions were applied similar to section 2.1. The frequency range of the simulations was 0-3 THz. The simulation results were obtained for the most simplified case, where the rings were not mounted on any substrate and the environment was vacuum. However, in reality, as will be explained in the fabrication section, each ring is patterned on either (Silicon) substrate or (parylene and Silicon) substrate. Since the loss of high resistivity float zone Silicon (HRFZ-Si) is low in THz regime, its transmission characteristics are similar to the air [53, 54]. Therefore, a shift in resonant frequencies

of the rings is expected between the simulation and experimental results due to the change in dielectric constant.

The results for each sample are discussed in the following sections.

### 3.1.1. Simulation Results for Sample One

The simulation results of different boundary conditions for sample one is shown in Figure 3.2.

In the first setting shown in Figure 3.2 (a), the electric field vector,  $\vec{E}$  is aligned with the x-axis. The magnetic field vector,  $\vec{H}$ , and the wave vector  $\vec{k}$ , are aligned with y-axis and z-axis respectively. As discussed in section 2.1 and similar to Figure 2.4 (b), while magnetic field is not perpendicular to the device, the electric field creates two circulating current paths on the top and bottom halves of the resonator. It results in a magnetic resonance of  $f = 1.92$  THz in the range of 0-3 THz. In the second setting,  $\vec{H}$  is aligned with the x-axis.  $\vec{E}$  and  $\vec{k}$ , are aligned with y-axis and z-axis respectively. The simulation result is shown in Figure 3.2 (b). The electric field polarized with the gap induces a circulating current loop in the ring and results in a magnetic resonance of  $f_1 = 0.9$  THz, while the second resonance  $f_2 = 2.48$  THz is an electric resonance. In the third setting shown in Figure 3.2 (c),  $\vec{E}$  is aligned with the x-axis.  $\vec{H}$  and  $\vec{k}$ , are aligned with y-axis and z-axis respectively. Magnetic field being perpendicular to the ring combined with the effect of electric field being polarized along the short side of the ring, induces two magnetic resonances and an electric resonance at  $f_1 = 0.8$ ,  $f_2 = 1.17$ , and  $f_3 = 2.27$  THz respectively. In the fourth setting in Figure 3.2 (d),  $\vec{k}$  is aligned with the x-axis;  $\vec{E}$  is aligned with the y-axis and  $\vec{H}$  is aligned with the z-axis. Magnetic field is perpendicular to the plane of the ring and induces a magnetic resonance at  $f_1 = 0.9$  THz and electric field is along the gap and induces an electric resonant frequency at  $f_2 = 3$  THz.

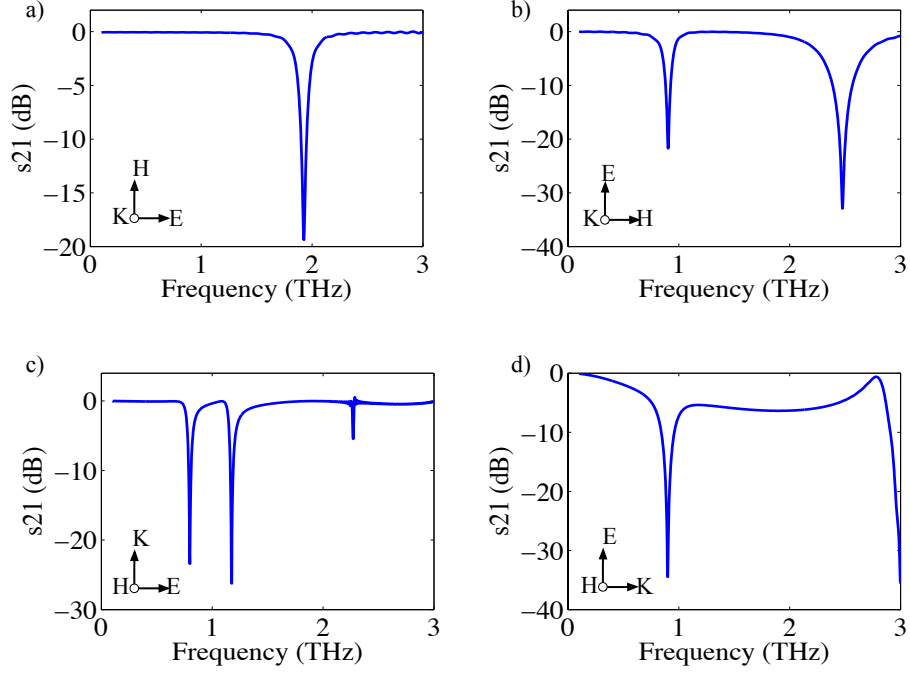


Figure 3.2. Simulation results of different boundary conditions for sample one.

### 3.1.2. Simulation Results for Sample Two

Figure 3.3 shows the simulation results for sample two for different boundary conditions. Figure 3.3(a) represents the results for the first setting, in which  $\vec{E}$  is aligned with the x-axis,  $\vec{H}$ , and  $\vec{k}$ , are aligned with y-axis and z-axis respectively. Electric field that is along the short side of resonator polarizes right and left sides of the rectangle with opposite charges and induces circulating current. The first resonant frequency  $f_1 = 0.89$  THz and the second resonant frequency  $f_2 = 1.81$  THz are magnetic. However, The third and the fourth resonances  $f_3 = 2.32$ ,  $f_4 = 2.86$  THz are electric. Also, the dips of the first and fourth frequencies are not pronounced. In the second setting in Figure 3.3 (b), where  $\vec{H}$  is aligned with the x-axis,  $\vec{E}$  and  $\vec{k}$ , are aligned with y-axis and z-axis respectively, the proposed ring has four resonant frequencies. Similar to the previous setting, the first and the second resonances,  $f_1 = 0.89$  and  $f_2 = 1.88$  THz, are magnetic. While the third and the fourth resonance,  $f_3 = 2.45$  and  $f_4 = 2.83$  THz are electric. In the third setting in Figure 3.3 (c),  $\vec{E}$  is aligned with the x-axis,  $\vec{k}$  and  $\vec{H}$ , are aligned with y-axis and z-axis respectively. The resonances are  $f_1 = 0.71$ ,

$f_2 = 1.06$  THz as magnetic, and  $f_3 = 2.21$  and  $f_4 = 3$  THz as electric resonances. In the fourth setting,  $\vec{k}$  is aligned with the x-axis;  $\vec{E}$  is aligned with the y-axis and  $\vec{H}$  is aligned with the z-axis as shown in Figure 3.3 (d). The pronounced frequencies in this case are  $f_1 = 0.87$  and  $f_2 = 2.38$  THz as magnetic resonances, and  $f_3 = 2.99$  THz as electric resonance.

Comparing the results of this design to the previous design, introducing asymmetry along the x-axis results in additional resonant frequencies in the range of 0-3 THz for applied boundary conditions.

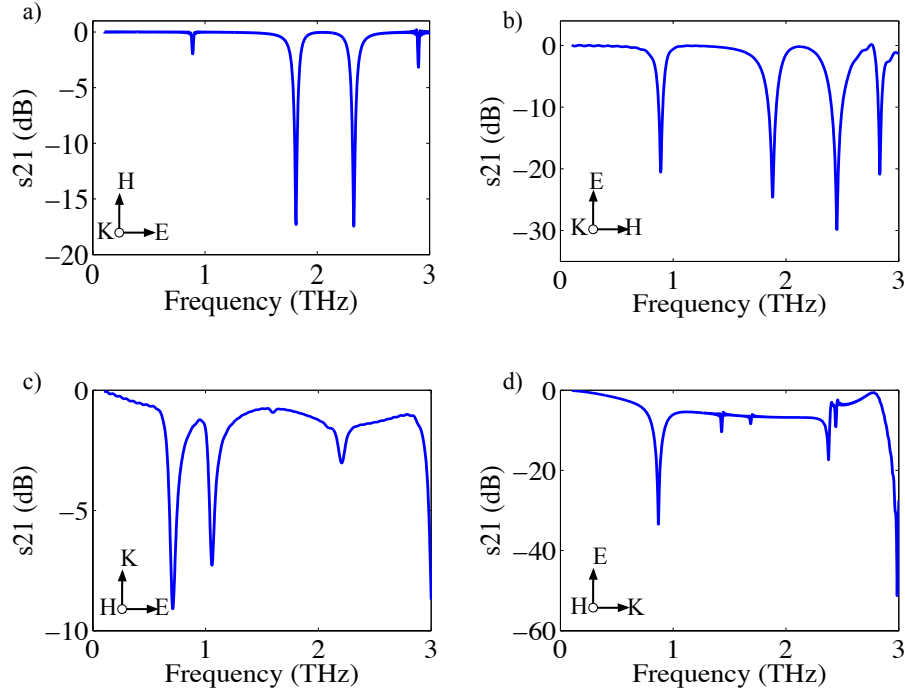


Figure 3.3. Simulation results of different boundary conditions for sample two.

### 3.1.3. Simulation Results for Sample Three

Figure 3.4 represents the simulation results of different boundary conditions for sample three. In the first setting as shown in Figure 3.4 (a),  $\vec{E}$  is aligned with the x-axis,  $\vec{H}$ , and  $\vec{k}$ , are aligned with y-axis and z-axis respectively. The electric field polarizes right and left sides of the ring and induces two circulating current paths at the top and bottom halves of the ring. The resonant frequency corresponding to

this is orientation is  $f_1 = 1.87$  THz and magnetic. In the second setting as shown in Figure 3.4,  $\vec{H}$  is aligned with the x-axis,  $\vec{E}$  and  $\vec{k}$ , are aligned with y-axis and z-axis respectively. At the first resonant frequency, which is magnetic and  $f_1 = 0.85$  THz, the electric field is along the gap and supports a single circulating current path through the ring. While the second resonant frequency,  $f_2 = 2.53$  THz is an electric resonance. In the third setting shown in Figure 3.4 (c),  $\vec{E}$  is aligned with the x-axis,  $\vec{k}$  and  $\vec{H}$ , are aligned with y-axis and z-axis respectively. The resonant frequencies are  $f_1 = 0.77$  THz as magnetic,  $f_2 = 1.48$ ,  $f_3 = 2.39$ , and  $f_4 = 2.8$  THz as electric resonances. In the fourth setting shown in Figure 3.4 (d),  $\vec{k}$  is aligned with the x-axis;  $\vec{E}$  is aligned with the y-axis and  $\vec{H}$  is aligned with the z-axis. This boundary condition results in two resonant frequencies; There is a circulating current path through the ring at the first resonant frequency,  $f_1 = 0.79$  THz, stemming from magnetic field that is perpendicular to the plane of the ring combined with the effect of electric field that is along the gap. At the second resonant frequency,  $f_2 = 2.59$  THz, there are two virtual nodes in the each long side of the rectangle, creating two circulating current paths in opposite direction. Therefore, both frequencies are considered to be magnetic.

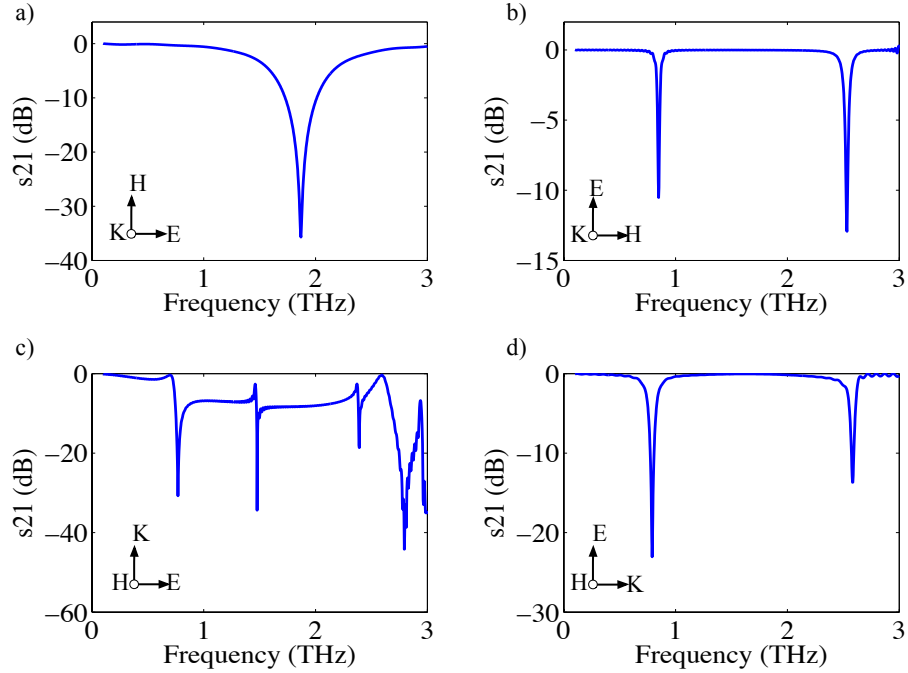


Figure 3.4. Simulation results of different boundary conditions for sample three.

### 3.1.4. Simulation Results for Sample Four

The simulation results of sample four for different boundary conditions are presented in Figure 3.5. The dimensions of sample four is relatively smaller than other designed samples, which results in higher resonant frequencies compared to the other proposed designs. Similar to previous sections, Figure 3.5 (a) shows the first setting, where  $\vec{E}$  is aligned with the x-axis,  $\vec{H}$ , and  $\vec{k}$ , are aligned with y-axis and z-axis respectively. The resonant frequency corresponding to this boundary condition is  $f = 1.79$  THz and is magnetic due to the presence of the electric field along the gap. In the second setting in Figure 3.5 (b), where  $\vec{H}$  is aligned with the x-axis,  $\vec{E}$  and  $\vec{k}$ , are aligned with y-axis and z-axis respectively, the corresponding resonant frequency is beyond 3 THz. In the third setting in Figure 3.5 (c),  $\vec{E}$  is aligned with the x-axis,  $\vec{k}$  and  $\vec{H}$ , are aligned with y-axis and z-axis respectively. The resonant frequency is  $f = 1.78$  THz and is magnetic. In the fourth setting,  $\vec{k}$  is aligned with the x-axis;  $\vec{E}$  is aligned with the y-axis and  $\vec{H}$  is aligned with the z-axis as shown in Figure 3.5 (d). The resonant frequency,  $f = 1.61$  THz, is magnetic.

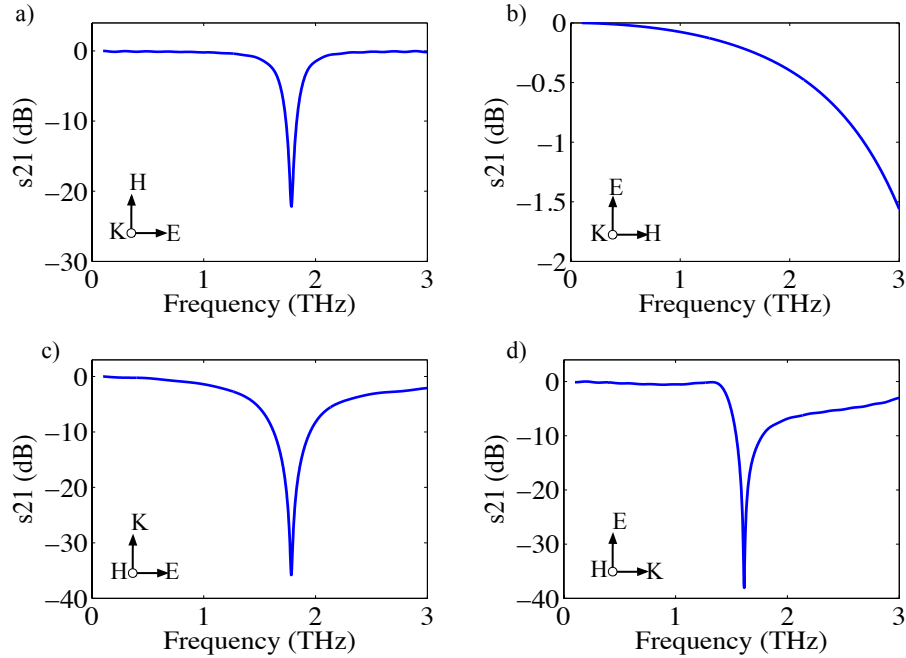


Figure 3.5. Simulation results of different boundary conditions for sample four.

### 3.1.5. Simulation Results for Sample Five

Figure 3.6 represents the simulation results of different boundary conditions for sample five. The shapes of the sample four and five are similar, however, sample five has larger dimensions compared to sample four. Therefore, sample five behaves the same way as sample four while the resonances shift to lower frequencies. As shown in Figure 3.6 (a) in the first setting,  $\vec{E}$  is aligned with the x-axis,  $\vec{H}$ , and  $\vec{k}$ , are aligned with y-axis and z-axis respectively. There are two resonant frequencies,  $f_1 = 0.84$  THz as magnetic, and  $f_2 = 2.79$  THz as electric resonances. In the second setting in Figure 3.6 (b), where  $\vec{H}$  is aligned with the x-axis,  $\vec{E}$  and  $\vec{k}$ , are aligned with y-axis and z-axis respectively, the corresponding magnetic resonant frequency is  $f = 2.04$  THz originating from two circulating current paths in opposite directions at the right and left sides of the ring. In the third setting in Figure 3.6 (c),  $\vec{E}$  is aligned with the x-axis,  $\vec{k}$  and  $\vec{H}$ , are aligned with y-axis and z-axis respectively. The corresponding resonant frequency,  $f = 0.76$  THz, is magnetic. In the fourth setting,  $\vec{k}$  is aligned with the x-axis;  $\vec{E}$  is aligned with the y-axis and  $\vec{H}$  is aligned with the z-axis as shown in Figure 3.6 (d). The resonant frequencies are  $f_1 = 0.65$  as magnetic, and  $f_2 = 2.27$  THz as electric resonances.

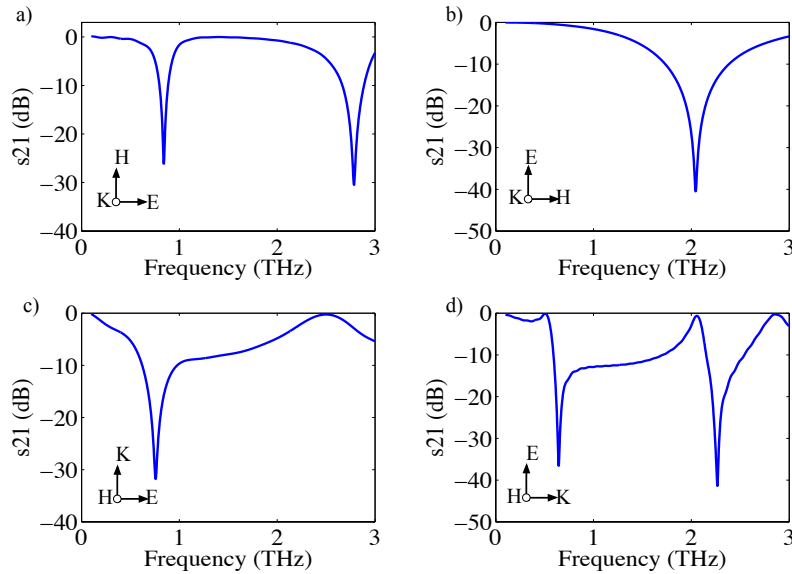


Figure 3.6. Simulation results of different boundary conditions for sample five.

Figures of the simulations with current density and electric field distributions are shown in appendix for more details.

### 3.1.6. Designing the Mask

A mask was designed to use in the fabrication process. The size of the mask is  $5'' \times 5''$  and is filled with dies. The dies have the size of the  $1 \text{ cm} \times 1 \text{ cm}$  each. On each die, one of the proposed samples is patterned as arrays. Figure 3.7 shows an illustration of the wafer and the dies. The distance between the samples of a die in the array is shown in Figure 3.7.  $d_1$  is the distance between the short sides of the two consecutive rings and is 50 micron, while  $d_2$  is the distance between the long sides of the two consecutive rings and is 100 micron. Dies corresponding to each sample are placed randomly in the mask. The layout of the mask is shown in appendix for more details.

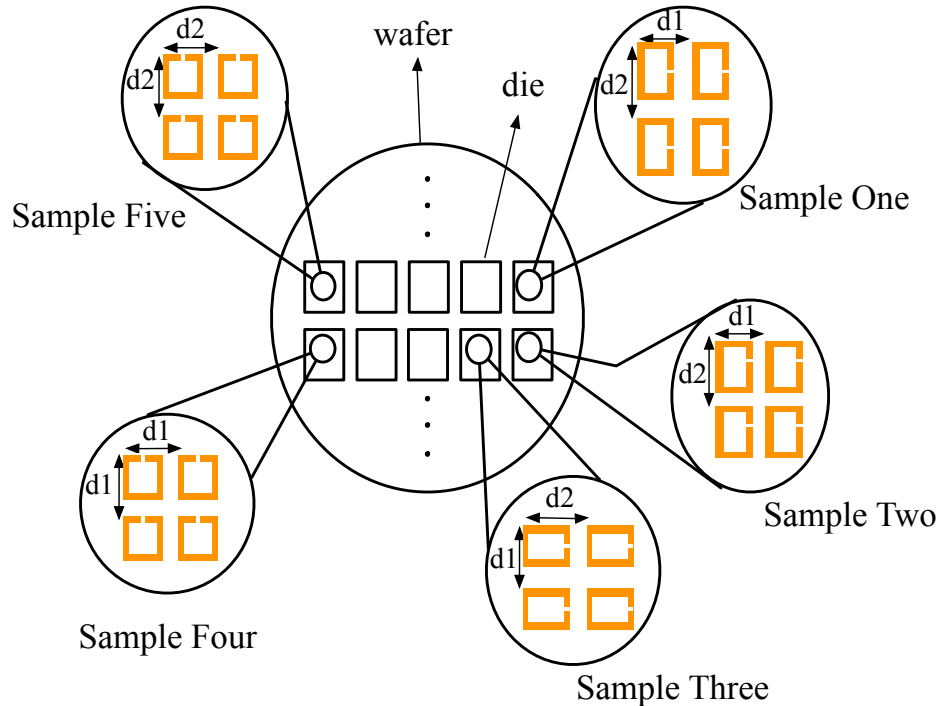


Figure 3.7. Illustration of the wafer and the dies. The wafer is filled with the randomly placed dies.  $d_1$  is the distance of the short sides of the consecutive rings, and is 50 micron.  $d_2$  is the distance between the long sides of two consecutive rings.

Figure 3.8. (a-e) shows the samples (1-5) and their dimensions under microscope.

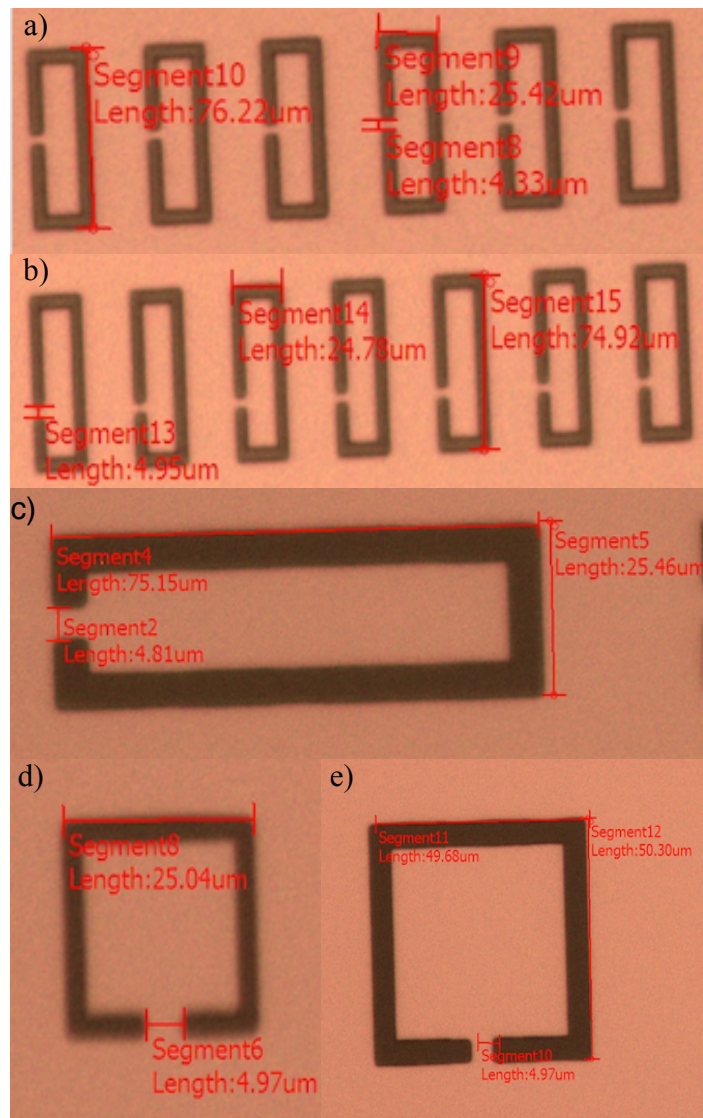


Figure 3.8. a) Sample one b) Sample two c) Sample three d) Sample four e) Sample five that are patterned on the mask and their dimensions.

There are some problems associating with the fabrication of the mask. Figure 3.9 shows the defects in the fabricated mask. Some of the designs were not carried out very well in some parts as can be seen in Figure 3.9.

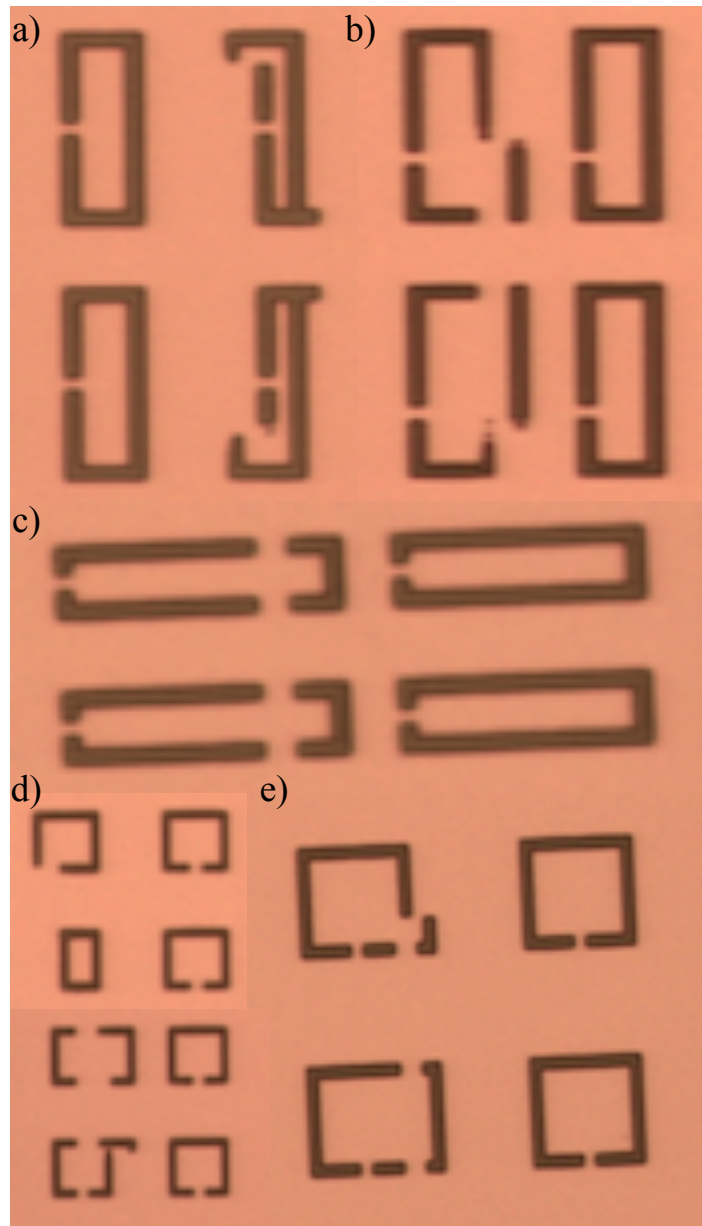


Figure 3.9. The defects in the fabricated mask for: a) Sample one b) Sample two c) Sample three d) Sample four e) Sample five.

## 3.2. Fabrication Process

Three types of devices were fabricated utilizing the mask. The first type is split ring resonators made of copper that are patterned on a Silicon wafer. In the second type, the Silicon wafer is coated with a layer of parylene and then split ring resonators made of copper are patterned on the substrate. In the third type, the Silicon wafer is coated with a thinner layer of parylene and then split ring resonators made of titanium are patterned on the substrate. Therefore, the principal fabrication steps include parylene deposition, photolithography, Cu/Ti sputtering, and chemical etching.

### 3.2.1. Fabrication of the First Type of the Devices: Copper Patterned on Silicon

A Silicon wafer with a diameter of 4" and with the resistivity of 100 ohm.cm was used as the substrate. The copper was patterned on the substrate through lift-off process. The starting point is photolithography. In this step, the substrate was spin-coated with Ti Prime to promote the adhesion of the photoresist to the substrate and then was pre-baked for 2 minutes on a hot plate at 120 °C. It took three minutes for the wafer to cool down. Then a layer of AZ5214 was spin-coated as the photoresist. AZ5214 is an image reversal resist, which means it can behave as both positive and negative photoresist depending on the purpose. It was used as a negative one in this work. Afterwards, the wafer was put on the hot plate at 110 °C for 50 seconds. It took 30 seconds for cooling. Then the wafer was exposed to UV light. The wavelength of the light is between 350-450 nm. Since AZ5214 is needed to act as a negative photoresist for lift-off, the exposure would be a two-step process. For the first step, the wafer was exposed to UV light together with the mask and the used energy was 40 joules. Then the wafer was put on the hot plate for 2 minutes at 120 °C. It took several minutes for the wafer to cool down. Afterwards for the second step in exposure, the mask was removed; the wafer was exposed to UV light. The used energy for the second step of the exposure was 200 joules. Later on, the pattern was developed utilizing a solution of AZ 400k. The developer solvent was prepared by diluting 4:1 of DI water and AZ 400k. The wafer was put in the solvent and it took 50 seconds. Then the wafer was

taken out, was put it in a container of DI water, and was dried afterwards.

The next step of fabrication was Cu sputtering. The rate of sputtering for Cu is 4.3 nm/min, the source is DC, and the power is 30 watts. In our case after photolithography, the substrate was coated with a layer of 500 nm Cu. Therefore it took 116 minutes for the substrate to be coated.

At the final step of fabrication, the photoresist was etched by putting the wafer in an ultrasonic bath of acetone. Then the wafer was put in DI water for a while and was dried afterwards. The wafer was diced at the end of the process. Fabrication process is shown in Figure 3.10 and Fabricated devices are shown in Figure 3.11.

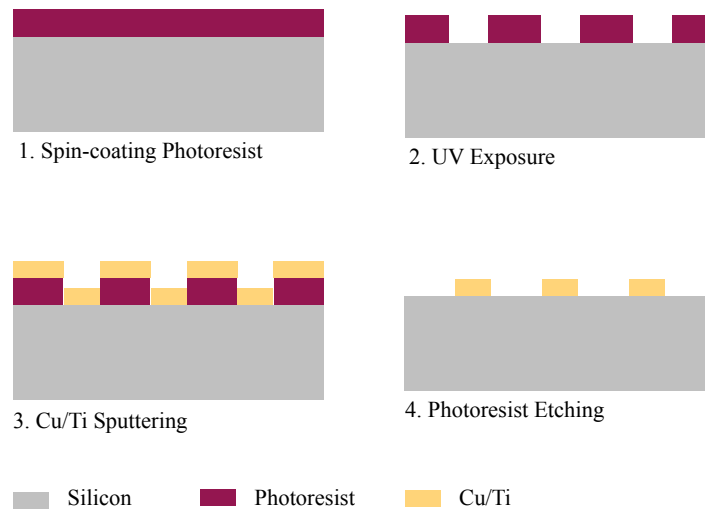


Figure 3.10. Fabrication Process of the first type of the devices.

Figure 3.12 shows problems through fabrication. Fabricated devices can easily be scratched and it can affect the measurements. Therefore it is essential to be very careful during experimental measurements or while placing the devices into the holder. As can be seen in Figure 3.12, some parts of the designs in fabricated devices are etched away. It can be due to several reasons. First, the defects in the fabricated mask can cause this problem. Second, it can be because of being in contact with other devices in the holder and the possible impacts. Third, it can be due to developing and chemical etching steps in the fabrication process; which means that pattern of the mask would

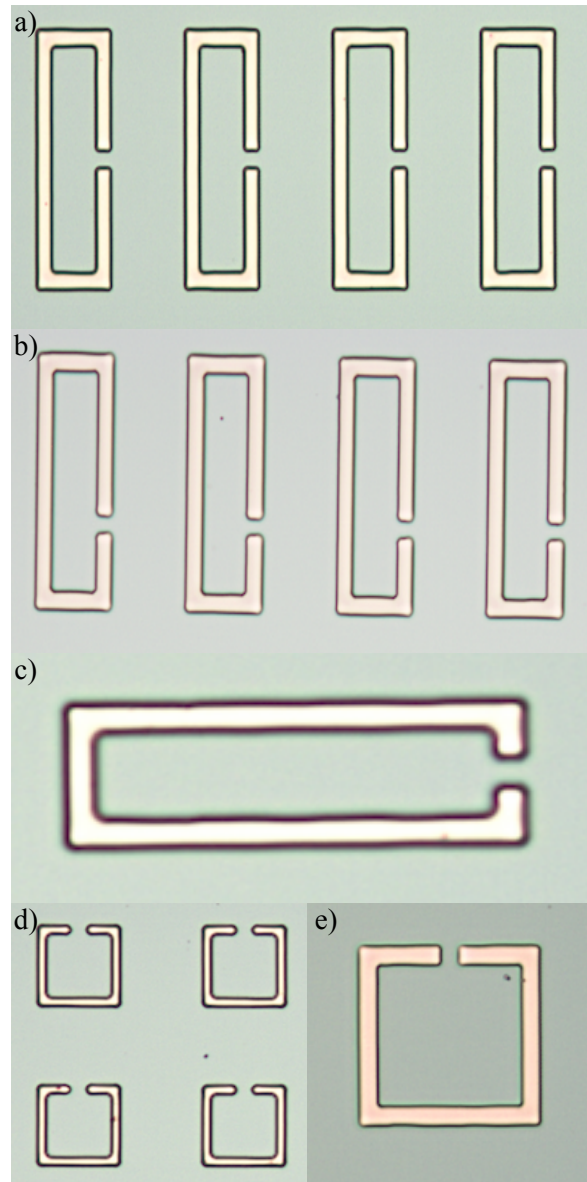


Figure 3.11. Fabricated First Type of the Devices: a) Sample one b) Sample two c) Sample three d) Sample four e) Sample five.

have not been developed sufficiently and therefore during the etching of the photoresist, some parts of the metal are etched away as well.

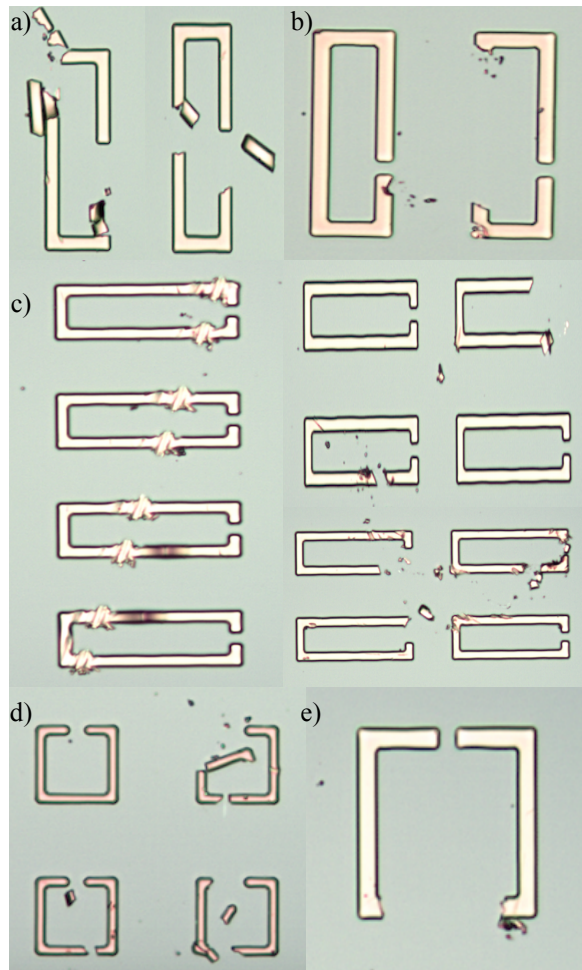


Figure 3.12. Defects of the First Type of the Fabricated Devices: a) Sample one b) Sample two c) Sample three d) Sample four e) Sample five

### 3.2.2. Fabrication of the Second Type of the Devices: Copper Patterned on Parylene and Silicon

A Silicon wafer with the diameter of 4" and with the resistivity of 100 ohm.cm was used as the substrate. A layer of parylene with the thickness of 500 nm was deposited on the Silicon substrate through chemical vapor deposition (CVD). The wafer was put in the chamber, waited for the vacuum pressure to reach 20 millitorr and the temperature of the hot path to reach 698 °C. Then the temperature of the container

of the parylene reached 175 °C, which meant that the coating was started. The whole process of parylene coating took three hours.

The second step of the fabrication was photolithography. The steps taken were the same as what was described in section 3.2.1. The pattern of the mask was developed on the wafer at the end of photolithography.

For the third step of the fabrication, the wafer was put in the chamber for Cu sputtering. The thickness of the Cu was aimed to be 500 nm. Since the rate of the operation is 4.3 nm/min, the source is DC, and the power is 30 watts, it took 116 minutes to coat the wafer with copper.

In the fourth step, the photoresist was etched away by putting the wafer in an ultrasonic bath of acetone for a while, and then was put in DI water. The wafer was dried and diced in the final step of the fabrication. Figure 3.13 presents the fabrication process and Figure 3.14 shows fabricated devices.

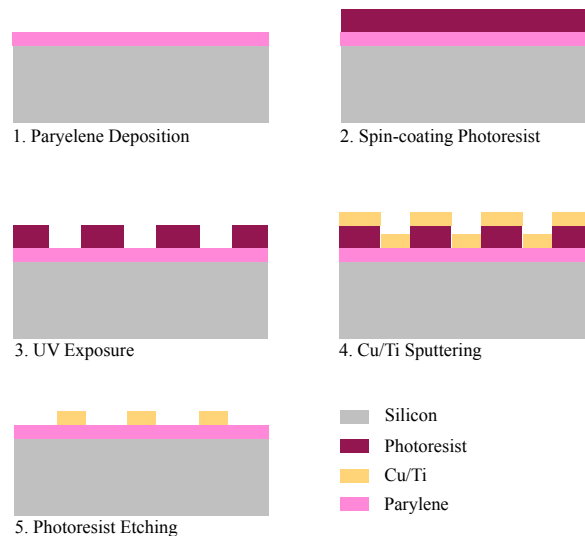


Figure 3.13. Fabrication process of the second and the third type of the devices.

Figure 3.15 shows defects in some parts of the fabricated devices. The problems raised through and after fabrication are discussed in detail in section 3.2.1.

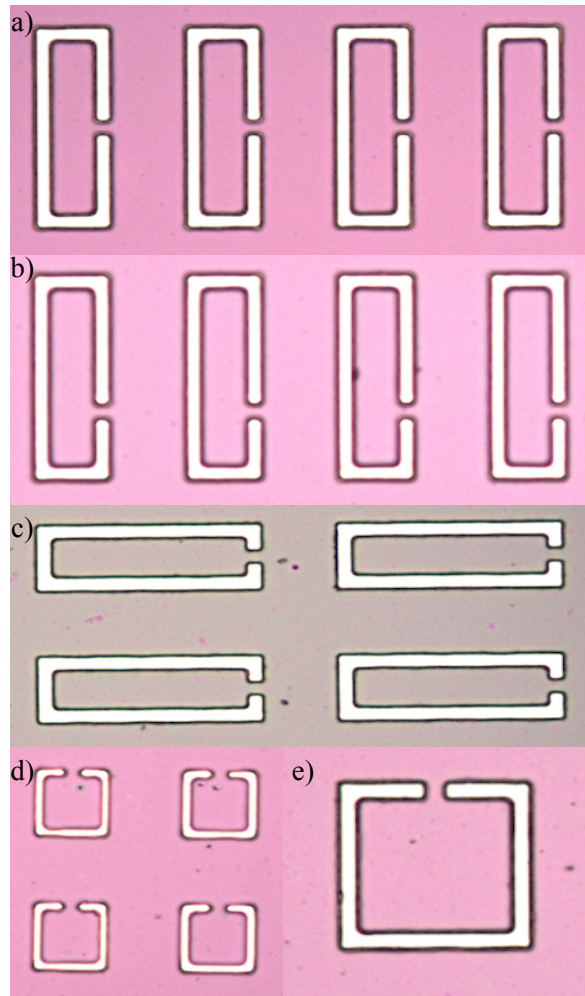


Figure 3.14. Fabricated Second Type of the Devices: a) Sample one b) Sample two c) Sample three d) Sample four e) Sample five.

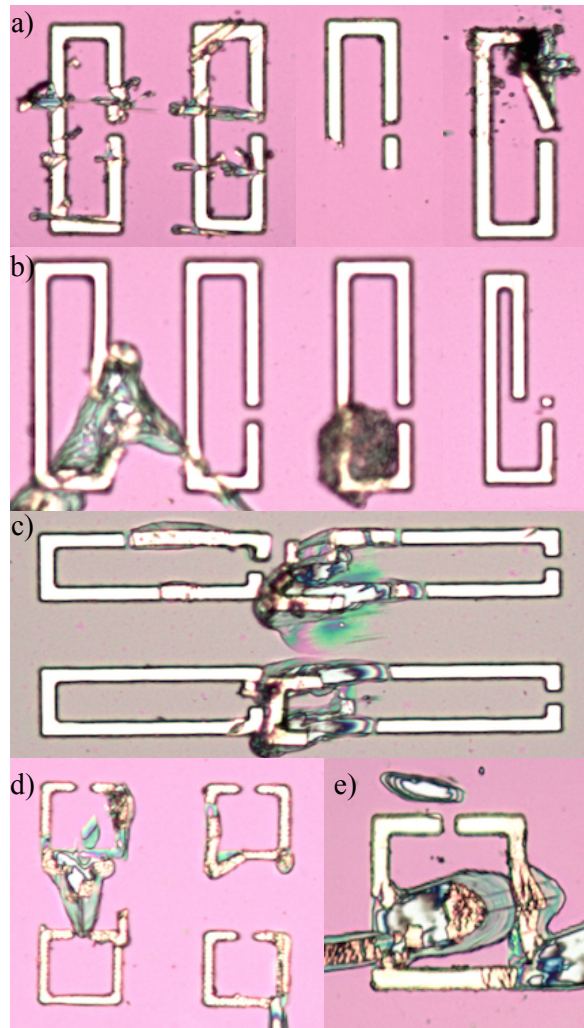


Figure 3.15. Defects of the Second Type of the Fabricated Devices: a) Sample one b) Sample two c) Sample three d) Sample four e) Sample five.

### 3.2.3. Fabrication of the Third Type of the Devices: Titanium Patterned on Parylene and Silicon

A Silicon wafer with a diameter of 4" and with the resistivity of 100 ohm.cm was used as the substrate. A layer of parylene was deposited on the Silicon substrate through chemical vapor deposition (CVD). The intended thickness for parylene was 250 nm. The wafer was put into the chamber, was waited for the vacuum pressure to reach 20 millitorr and the temperature of hot path to reach 698 °C. Parylene coating was started where the temperature of the parylene container reached 175 °C. It took three hours for the coating to be finished.

The second step of the fabrication was photolithography. The steps taken were the same as what was described in section 3.2.1. The pattern of the mask was developed on the wafer at the end of photolithography.

The third step was titanium sputtering. The intended thickness of titanium was 250 nm. The source was RF, the power was 130 watt, and the coating rate was 4.3 nm/min. Therefore, it took 58 minutes to deposit a layer of 250 nm Ti on the wafer.

In the final step, the wafer was put in an ultrasonic bath of acetone in order to etch away the photoresist present on the wafer. Then the wafer was put in DI water for a while. It was dried and diced at the end of the fabrication process.

Figure 3.13 and 3.16 show the fabrication process and fabricated devices respectively. Figure 3.17 shows defects in some parts of the fabricated devices. The problems raised through and after fabrication are discussed in detail in section 3.2.1.

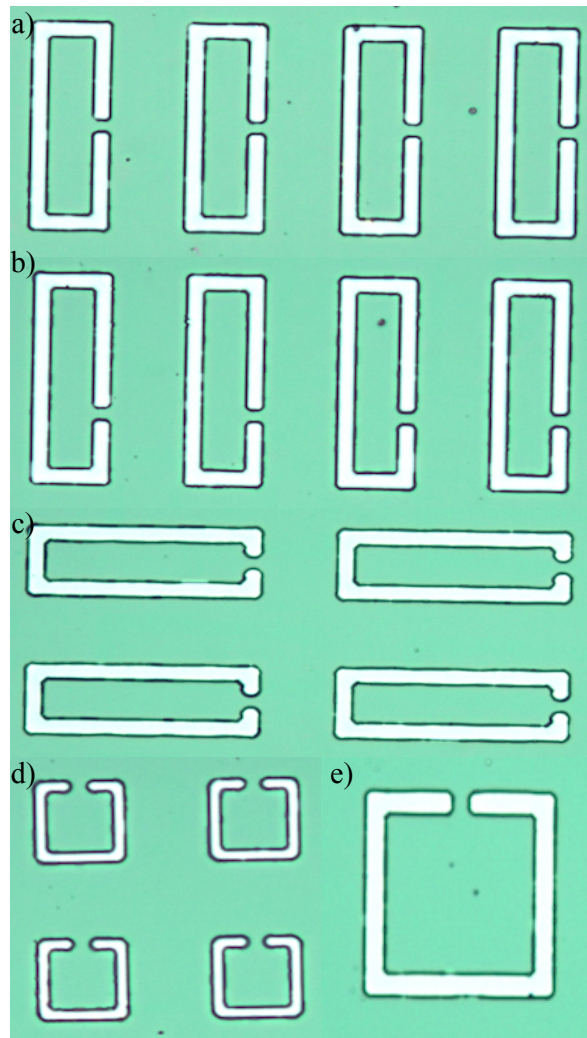


Figure 3.16. Fabricated Third Type of the Devices: a) Sample one b) Sample two c) Sample three d) Sample four e) Sample five.

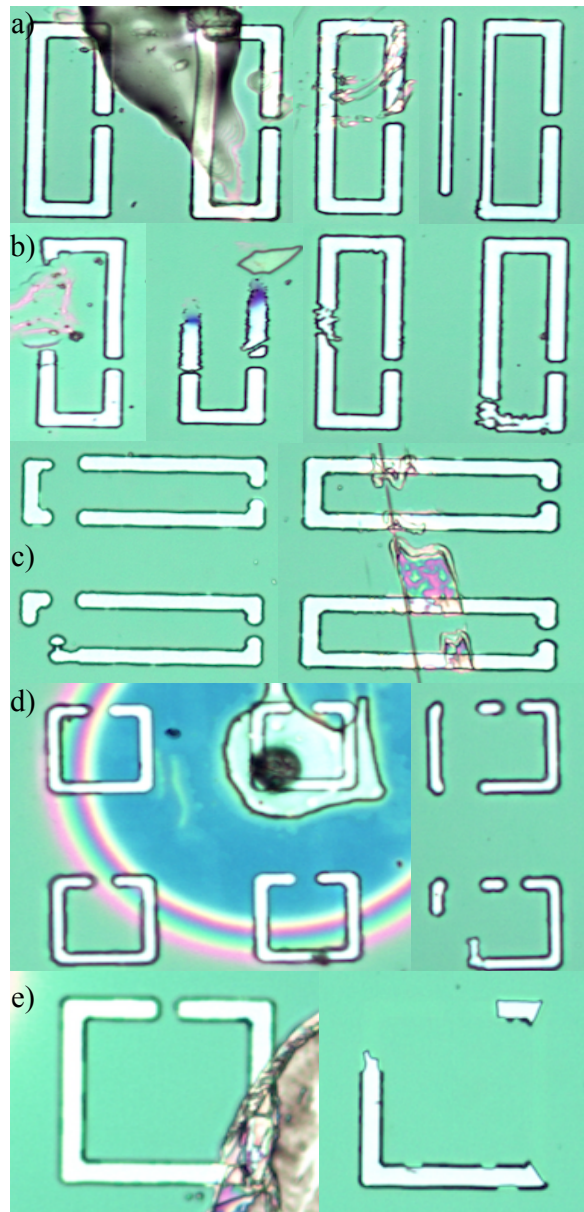


Figure 3.17. Defects of the Third Type of the Fabricated Devices: a) Sample one b) Sample two c) Sample three d) Sample four e) Sample five.

### 3.3. Experimental Characterization

In this section, the experimental results of the fabricated devices are presented and discussed. The devices were characterized using a terahertz time-domain spectroscopy (THz-TDS, TERA K15, Menlo Systems GmbH, Martinsried, Germany) with maximum optical power of 80 mW, employing a 1550 nm femtosecond fiber laser with a spot size of 2 mm., Laser repetition rate is from 80 MHz to 250 MHz for the transmitter and the receiver. Spectral range is 3 THz, and spectral resolution is 5 GHz. The devices were illuminated in transmission mode and the transmission spectra were obtained using reference measurements. The setup is shown in Figure 3.18.

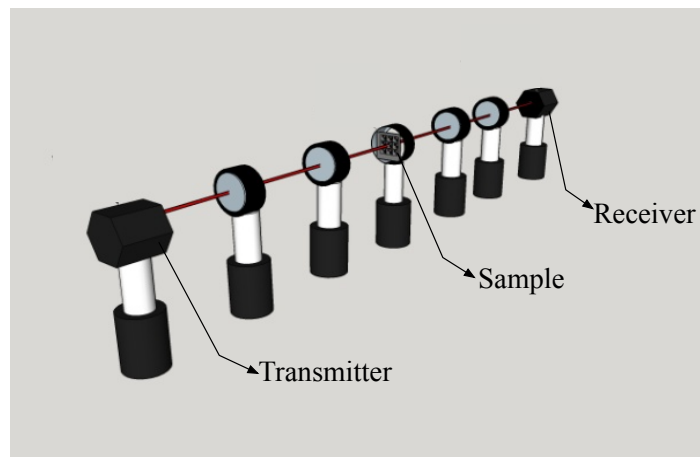


Figure 3.18. Setup for the transmission mode of the terahertz time-domain spectroscopy.

Since the experiments are not performed in the vacuum, the humidity of the air can influence the measurements and can be a restriction [54, 55]. Figure 3.19 (a-c) shows the transmission characteristics of dry air, humid air and Si respectively.

During the experiments, the error caused by water absorption was minimized by placing silica gels in the THz-TDS chamber, and pumping  $N_2$  gas before characterizing the samples.

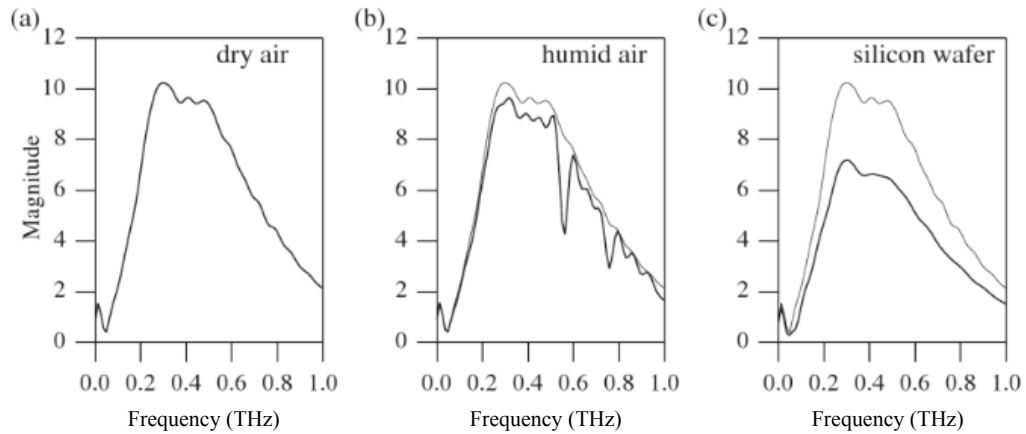


Figure 3.19. Transmission characteristics of a) dry air b) humid air and c) Si at THz frequencies [54].

### 3.3.1. Experiment Results for the First Type of Devices: Copper Patterned on Silicon

The experimental results for the device one, where copper is patterned on the Silicon is shown in Figure 3.20. The frequency range of the setup is 0-2.4 THz. The results for samples one to five correspond to Figure 3.20 (a-e) respectively. The red graphs are the experiment results. Whereas, the blue graphs are the simulation results.

Figure 3.20(a) shows the experiment and simulation results for sample one. The first resonant frequency considered to be magnetic is  $f_1 = 0.82$  THz, the second frequency is electric and is  $f_2 = 1.92$  THz. As shown in the figure, it corresponds to the simulation results of sample one in Figure 3.2(b). The first frequency is 8.89% smaller than the simulation result, whereas the second resonant frequency is smaller than the simulation result by 22%.

Figure 3.20(b) presents the experiment and simulation results for sample two. In the top graphs of Figure 3.20(b), the experiment result is similar to the simulation result in Figure 3.3(b). While in the bottom graphs of Figure 3.20(b), the experiment result is similar to the simulation result in Figure 3.3(a). For the experiment result of the

top graph, the resonant frequencies are  $f_1 = 0.83$  THz,  $f_2 = 1.37$  THz,  $f_3 = 1.59$ , and  $f_4 = 2.09$  THz. The measured first, second, third, and fourth resonant frequencies are smaller than the resonant frequencies obtained from the simulation by 6.74%, 27.13%, 35.1%, and by 26.15% respectively. In the bottom graphs of the Figure 3.20(b), the first and second measured frequencies in the experiment are  $f_1 = 1.42$  THz, and  $f_2 = 2.13$  THz. The values of the measured resonant frequencies in this case are smaller than the corresponding resonant frequencies in the simulation, Figure3.3(a), by 24.47%, and 13.06% respectively.

In Figure 3.20(c), the experiment and simulation result for sample three are shown. In this case, the experiment result is similar to the simulation result in Figure 3.4(b). The measured values of the resonant frequencies are  $f_1 = 0.87$  THz, and  $f_2 = 2.07$  THz. The first resonant frequency is magnetic and is larger than the simulation result by 2.35%. While, the second resonant frequency is electric and is smaller than the simulation result by 18.18%.

Figure 3.20(d) shows the experiment and simulation results for sample four. The experimental result is similar to the simulation result in Figure 3.5(a). In the experiment result, there are two frequencies as  $f_1 = 1.58$  THz, and  $f_2 = 2.18$  THz. The value of the first measured resonant frequency is smaller than the simulation result by 15.5%. The second resonant frequency in the experiment is not apparent in the simulation result. It might be due to the substrate or might be arising from the setup.

Figure 3.20(e) illustrates the experiment and simulation results for sample five. In this case, the experimental result is similar to the simulation result in Figure 3.6(a). The values of the measured resonant frequencies are  $f_1 = 0.85$  THz and  $f_2 = 2.18$  THz. The value of the first resonant frequency in the experiment is larger than the simulation result by 1.19%. However, the value of the second resonant frequency in the experiment is smaller than the simulation result by 21.86%.

Since the characterization of the samples has been done in transmission mode, comparisons between the experimental results to the simulation results will be investi-

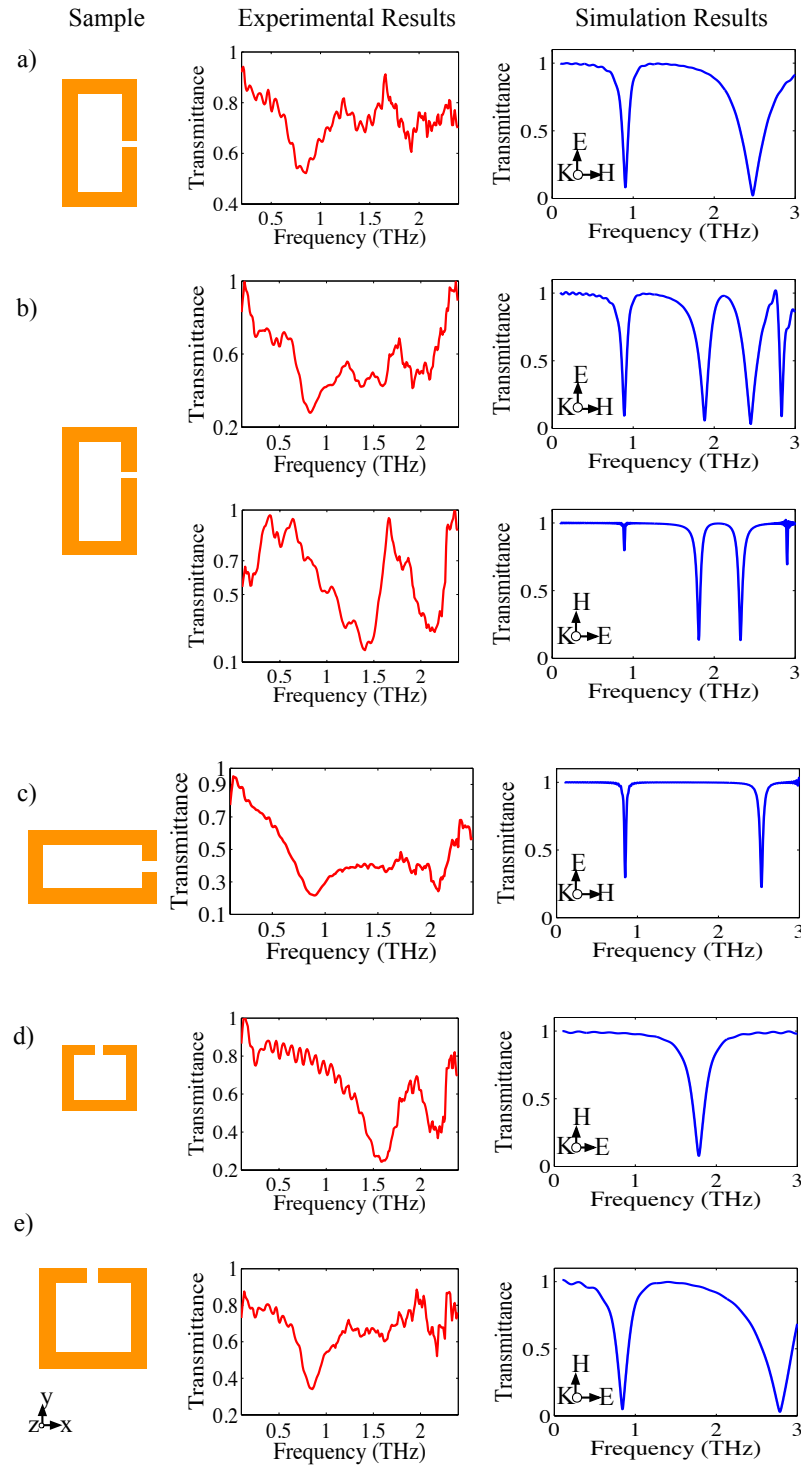


Figure 3.20. Experiment and simulation results of device one. Red graphs are experiment results of the samples one to five, while the blue graphs are the simulation results of the samples one to five.

gated for the excitation configurations, where the propagation vector,  $\vec{k}$ , is perpendicular to the plane of the samples. Comparing the simulation and experiment results, it can be stated that there are discrepancies between the measured values and simulations. One reason is that the samples were modeled in the CST Studio in the most simplified case, where the substrate is vacuum. However, for the experiment results the substrate is Silicon. Therefore it changes the capacitance of the rings and the frequencies shift. The other reason is that the direction of the electric and magnetic field are not controllable in the experimental setup. In addition, there are some defects related to the mask and the fabricated samples that drag the measurements apart from the ideal case in the simulations. Therefore, the defects in the fabricated samples may cause additional errors for the measured values.

### 3.3.2. Experimental Results for the Second Type of Devices: Copper Patterned on Parylene and Silicon

The experimental results in the range of 0-2.4 THz for device two, where copper is patterned on a substrate of parylene and Silicon, is shown in Figure 3.21. The results for samples one to five correspond to Figure 3.21 (a-e) respectively. The red graphs are the experiment results. Whereas, the blue graphs are the simulation results.

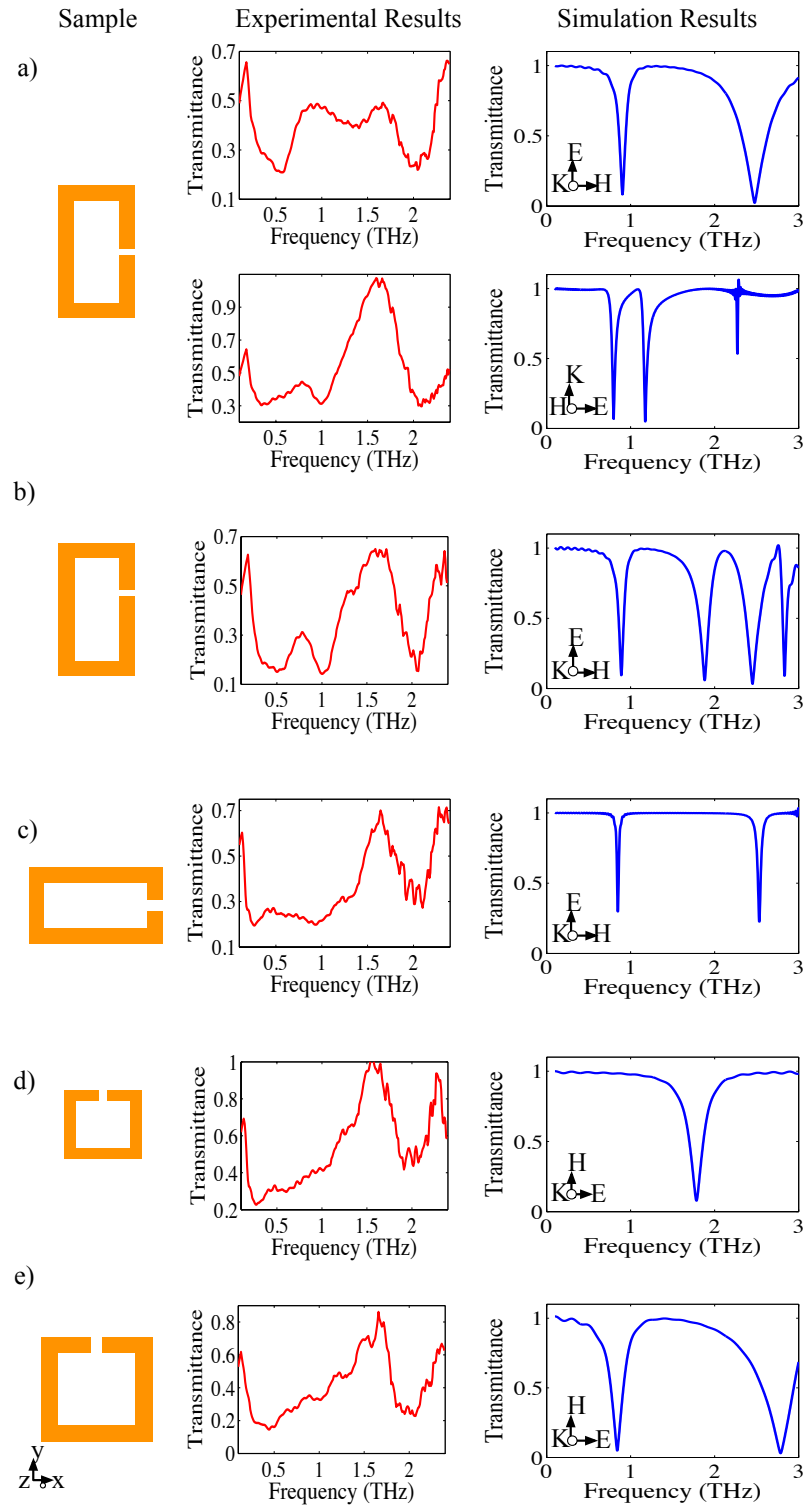
Figure 3.21(a) represents the experiment and simulation results for sample one. In the top graphs of Figure 3.21(a), the experiment result is similar to the simulation result in Figure 3.2(b). While in the bottom graphs of Figure 3.21(a), the experiment result is similar to the simulation result in Figure 3.2(c). For the experiment result of the top graph, the resonant frequencies are  $f_1 = 0.54$  THz, and  $f_2 = 2.04$  THz. The measured first, and the second resonant frequencies are smaller than the resonant frequencies obtained from the simulation by 40%, and 17.74% respectively. In the bottom graphs of the Figure 3.21(a), the first, the second, and the third measured resonant frequencies in the experiment are  $f_1 = 0.39$  THz,  $f_2 = 0.98$  THz, and  $f_3 = 2.1$  THz. The values of the measured resonant frequencies in this case are smaller than the corresponding resonant frequencies in the simulation, Figure 3.2(c), by 51.25%, 16.24%, and 7.49% respectively.

Figure 3.21(b) shows the experiment and simulation results for sample two. The first resonant is  $f_1 = 0.49$  THz, the second and the third resonant frequencies are  $f_2 = 1.01$  THz and  $f_3 = 2.07$  THz respectively. As shown in the figure, it corresponds to the simulation results of sample two in Figure 3.3(b). The measured values of the first, the second, and the third resonant frequencies are smaller than the simulation result by 44.94%, 46.28%, and 15.51% respectively.

In Figure 3.21(c), the experiment and simulation results of sample three are illustrated. The experiment result for this case corresponds to the simulation result in Figure 3.4(b). The measured values of resonant frequencies are  $f_1 = 0.25$  THz,  $f_2 = 0.94$  THz, and  $f_3 = 2.09$  THz. Since molecules can be trapped in the parylene layer, the first resonant frequency is supposed to be coming from possibly trapped particles or molecules in the parylene layer rather than the split ring resonators. However, the second resonant frequency is similar to the first resonant frequency in the simulation and is larger by 10.59%. Also, the value of the third resonant frequency is similar to the second resonant frequency in the simulation and is smaller than it by 17.39%.

Figure 3.21(d) presents the experiment and simulation results of sample four. The experiment result is comparable to the simulation result in Figure 3.5(a). The measured values of the first and the second resonant frequencies in the experiment are  $f_1 = 0.28$  THz, and  $f_2 = 1.91$  THz respectively. Similar to the previous case, the first resonant frequency is supposed to be arising from the possibly trapped molecules in the parylene layer. However, the second resonant frequency in the experiment corresponds to the first resonant frequency in the simulation and is larger than it by 11.69%.

Figure 3.21(e) shows the experiment and simulation result for sample five. As shown in the figure, the experiment result corresponds to the simulation result of sample five in Figure 3.6(a). The measured value of the first resonant frequency is  $f_1 = 0.44$  THz and is smaller than the simulation result by 47.62%. The measured value of the second resonant frequency in the experiment is  $f_2 = 2.05$  THz and is smaller than the simulation result by 26.52%.



Similar to what explained in section 3.3.1, discrepancies between experimental and simulation results are due to several reasons. First, the simulations in CST were done in the most simplified environment, where the substrate was vacuum. However, the actual substrate in this case was Silicon with a layer of parylene on top of it. Therefore, the frequency would shift because of the change in the dielectric and the capacitance of the split ring resonators. Second, electric and magnetic fields cannot be controlled during the experiments. Third, there are some defects both in the mask, and also additional errors in the fabricated samples. Lastly, as time passes or during the fabrication process, other particles or molecules can be trapped in the layer of the parylene and may add additional frequencies while characterizing the samples.

### 3.3.3. Experimental Results for the Third Type of Devices: Titanium Patterned on Parylene and Silicon

The experimental results in the range of 0-2 THz for device three, where titanium is patterned on a substrate of parylene and Silicon are shown in this section. After the fabrication, the wafer was diced in such a way that each piece contained multiple numbers of the samples. Figure 3.22 shows the experiment result for a device that contained sample one, three, four and five. In this case, the whole device was illuminated using the THz time domain spectroscopy in the transmission mode. The resonant frequencies are  $f_1 = 1.19$  THz, and  $f_2 = 1.78$  THz.

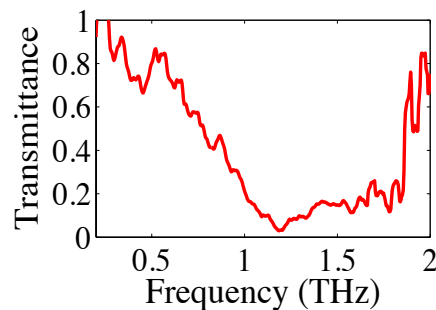


Figure 3.22. Experiment result for a device containing samples one, three, four and five.

Then the window of the holder was limited in order to illuminate the samples individually. Figure 3.23 shows the experiment results of sample one and three. Figure 3.23(a) presents the experiment result of the sample one. The measured value of the resonant frequency is  $f = 1.21$  THz and is similar to the simulation result in 3.2(a). Figure 3.23(b) shows the experiment result for sample three. The measured resonant frequency is  $f = 1.76$  THz and is similar to simulation result in Figure 3.4(a). It can be inferred that by illumination the whole device, the result in Figure 3.22 has been obtained, which is the superposition of the individual experimental results of sample one and sample three.

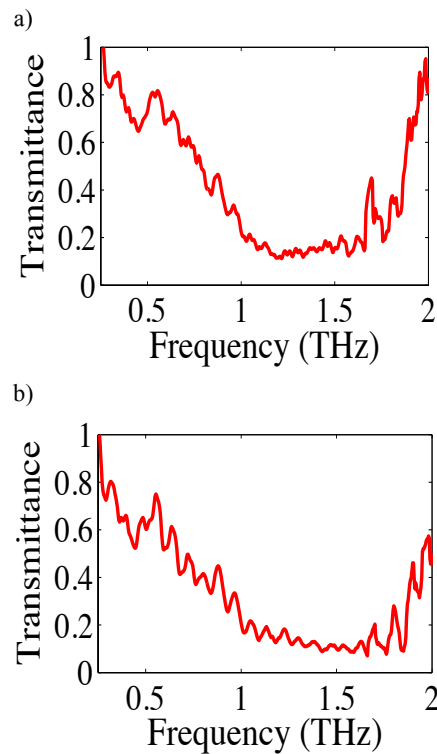


Figure 3.23. Experiment result the individual samples on a device containing sample one, three, four, and five. a) experiment result of sample one. b) Experiment result of sample three.

In Figure 3.24, the experiment results of a device that contains sample one, two, three, and four is shown. In Figure 3.24(a) the measured values of the frequencies are  $f_1 = 1.2$  THz, and the  $f_2 = 1.79$  THz. The experiment result of this device is

very similar to the result in Figure 3.22. By comparing Figure 3.24(a) and 3.22, it can be deduced that sample one and sample three are the illuminated samples. Then the orientation of the device was changed and the transmission spectrum was extracted in Figure 3.24(b). The measured values of frequencies are  $f_1 = 0.28$  THz,  $f_2 = 1.12$  THz, and  $f_3 = 1.71$  THz. The obtained result in this case is very similar to the experiment results in 3.21(c-d), which infers that samples three and four are the illuminated sample.

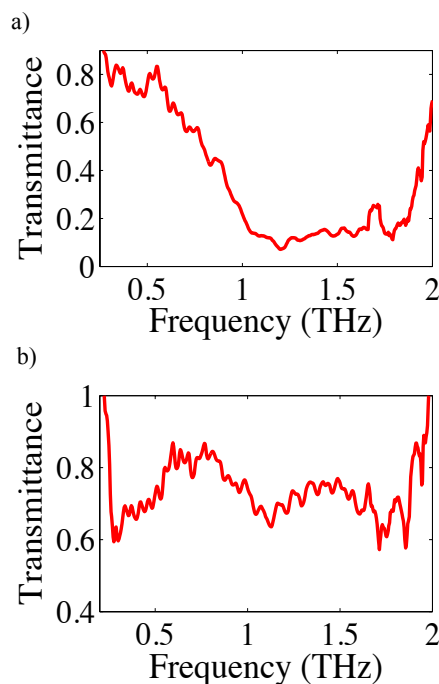


Figure 3.24. Experiment results of different orientations for a device containing samples one, two, three, and four.

After dicing the wafer at the end of the fabrication process, an extra layer of parylene was deposited on top of the split ring resonators for some of the diced devices. The thickness of the extra layer of the parylene is 250 nm. Figure 3.25 shows the experiment results of a device that contains sample one, two, three, and four before and after the deposition of the extra layer of parylene. Figure 3.25(a) is the experiment result of the proposed device before the addition of the extra layer of the parylene. The measured values of resonant frequencies are  $f_1 = 1.2$  THz and  $f_2 = 1.79$  THz. Figure

3.25(b) is the experiment result of the proposed device with the extra layer of the parylene. The measured values of the resonant frequencies are  $f_1 = 1.2$  THz,  $f_2 = 1.62$  THz,  $f_3 = 1.78$  THz. The deposition of the additional parylene layer on top of the split ring resonators affects the results due to the Fabry-Perot interference. Also, it makes the second resonant frequency,  $f_2 = 1.62$  THz, more pronounced.

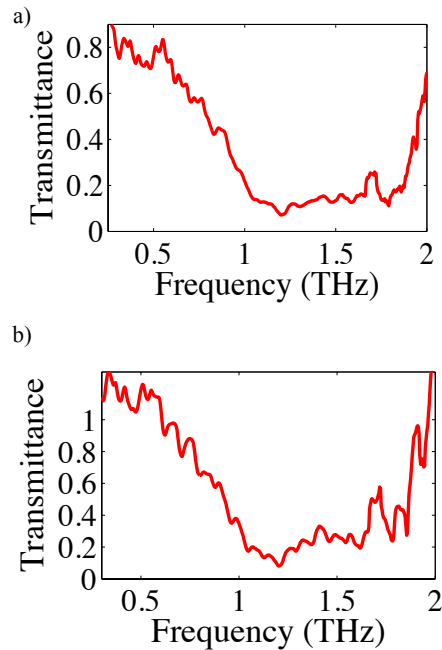


Figure 3.25. Experiment results for a device containing samples one, two, three, and four a) without and b) with the deposition of the extra layer of the parylene.

Figure 3.26 shows the experiment result for a device that contains sample one, sample two, sample three, and sample five. The measured values of the resonant frequencies are  $f_1 = 0.34$  THz,  $f_2 = 1.16$  THz,  $f_3 = 1.83$  THz. Comparing the experiment result of this device with Figure 3.22 and Figure 3.23, it can be stated that the illuminated samples are sample one, sample two, and sample three.

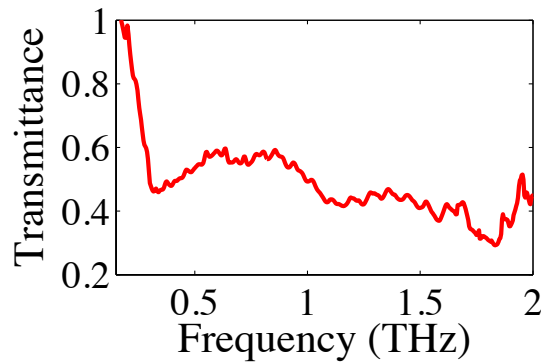


Figure 3.26. Experiment results for a device containing samples one, two, three, and five.

#### 3.3.4. Bio-experiments with Glucose

Sample three of the second type of the devices was chosen for bio-experiments and was characterized in transmission mode for the first step. Then 9 grams of the glucose was added to a 20 ml DI water and a high concentration solution of the glucose with DI water was prepared. The chosen sample was dipped in the solution. It was characterized after it got dried. Figure 3.27 shows the experiment results. The blue graphs are the experiment result where glucose is not yet added. While the red graphs are the experiment results after dipping the samples into the glucose solution.

The experiment results are shown in the frequency range of 0-1 THz. Figure 3.27(a) shows the raw data extracted from the THz time domain spectroscope. Then the raw data was divided to the reference data and the transmission measurements were extracted as shown in Figure 3.27(b). The measured values of the resonant frequencies before adding glucose to the sample are  $f_1 = 0.21$  THz,  $f_2 = 0.42$  THz,  $f_3 = 0.79$  THz, and  $f_4 = 0.97$  THz and are shown in blue graphs. However, the measured values of the frequencies after adding glucose to the sample are  $f_1 = 0.21$  THz,  $f_2 = 0.6$  THz,  $f_3 = 0.78$  THz, and  $f_4 = 0.99$  THz and are shown in red graphs. The effective permittivity of the glucose decreases by increasing the frequency, leading to a reduction in the effective capacitive behavior of it. It is also observed that the higher the concentration of the glucose, the lower the value of the effective permittivity [56–58]. Therefore, it can

be claimed that the high concentration of the glucose reduces the total capacitance of the rings and shifts the resonant frequency to a higher resonant frequency (the second resonance in this case). Experimental result presented in Figure 3.27 verifies the expectation. By comparing the blue and the red graphs in Figure 3.27, the value of the shift is calculated to be 0.18 THz. It means that the fabricated sensors have the potential to be utilized as biosensors. It is needed to carry out more experiments and to extract the sensitivity and specificity of the sensors in order to confirm their ability to function as biosensors.

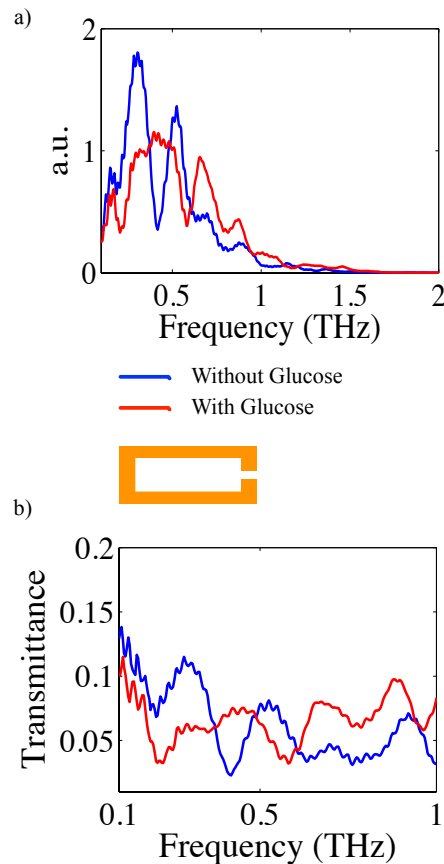


Figure 3.27. Bio-experiment results for sample three. a) Raw data obtained from the THz time domain spectroscopy. b) Transmission characteristics of the device.

### 3.4. Discussion

In this part, the observations from the simulation and experimental results are summed up. Every sample will be analyzed individually and comparisons will be made among the proposed devices.

In the first type of fabricated devices as shown in Figure 3.20, the total expectations over the behavior of the fabricated resonators are fulfilled in comparison with the simulation results except for sample four. In sample one, two, three, and five, the behavior of the resonators in the experiments nearly match the simulation results, however, the quality factor of some of the experimental resonant frequencies is not very high as it was in the simulations. Also in sample four, it was expected to observe a single resonance according to the simulations, nonetheless, two resonant frequencies that were close to each other were appeared in the experiments and the exact reason is unknown. Also by comparing different designs, it can be seen that sample two provides more resonant frequency compared to sample one, which is in agreement with the expectations. It was predicted to see a shift in the resonant frequencies of sample three compared to sample one. The reason is that replacing the gap to the short sides of the rectangle is believed to reduce the coupling effect between the sides of the rectangle and therefore, decrease the total capacitance of the resonators. On the other hand, the reduction in the capacitance will lead to an increase in the value of the resonant frequencies. By observing the simulation and experimental results, it can be stated that the expectations are met for the case of the experiments, however, comparing the simulation results of sample one and three indicates that the behavior of the resonances remained unchanged. Since the dimensions of the sample four is scaled down compared to other samples, it was expected for the first occurring frequency of sample four to be higher in value compared to the first resonances of other samples. The simulation and experimental results verify the expectation. In the fifth sample compared to the first sample, the first resonant frequencies are almost the same, and are mainly due to the same gap capacitance. However, the second resonant frequency is shifted to higher values in the case of sample five, which is an indication of the less coupling effect between the sides of the square with respect to the sides of the rectangle.

In the second type of fabricated devices, the total expectations from the behavior of the designed samples are met except for sample three and four. In the mentioned samples, there is an additional frequency of 0.25 THz observed in the experiments, however, it is not present in the simulation results. The addition of the parylene layer to the device is assumed to cause this mismatch. In addition, the quality factors for some resonances in the fabricated samples are not as high as the simulations. Due to the introduced asymmetry, it was also expected to observe more resonances in sample two compared to sample one where the magnetic field is polarized along the short sides of the rectangle and the electric field is polarized along the gap. The experimental and simulation results confirm the expectation. Comparing the sample three and sample one, a shift towards higher frequencies in sample three was expected due to the decreased coupling between the sides of the rectangle and decreased conduction path, nevertheless, the first frequency of sample one shifted toward the lower frequencies and the second frequency is almost remained unchanged in both cases (ignoring the resonance of 0.25 THz present in sample three). Disregarding the first frequency apparent in the experiment results of sample four, the expectation of having higher resonance in this sample compared to others is met. Comparing the resonances between sample one and five, it was expected to see a shift towards higher frequencies for the second resonance of sample five (due to the less coupling effect in the square design). However, the total behavior and the resonances are almost the same for both cases.

The addition of the parylene layer to the second type of fabricated devices compared to the first fabricated devices was expected to shift the fundamental frequencies of all samples towards lower frequencies due to water absorption in parylene layer and also an increase in the effective permittivity of the devices. The expectation is met for all of the samples, except sample three in the second type of fabricated devices.

Comparing the third type of devices with the first type of devices, it was expected to see a shift in resonant frequencies towards lower frequencies because of the change in the effective dielectric of the third type. In addition, comparing the third type of devices with the second type of devices, it was predicted to see identical behaviors. However, none of the expectations are met since the value of the fundamental resonant

frequency in the third type shifted towards higher values compared to the other two cases.

For the bio-experiment measurement done for one of the samples of the second type of devices, it was expected to see a shift in resonant frequency towards higher values because of the electrical properties of the glucose. Comparing the experimental results before and after the addition of the glucose confirms that the expectation is fulfilled.

### **3.5. Future Work**

According to the comparisons between simulation and experimental results in section 3, the first type of fabricated devices matches the best with the simulation results. Therefore, new experiments will be done with devices in which copper is patterned on the Silicon substrate. Also, doing so will eliminate the errors coming from the parylene layer. In order to decrease the errors arising from humidity into the minimum, it is recommended to use a vacuum chamber during the experiment. For bio-experiments, different concentrations of glucose and DI water will be utilized and the impact of the glucose on the resonators will be analyzed more precisely. Furthermore, the sensitivity and specificity of the devices will be extracted. New devices of the first type will be fabricated in addition to the previously characterized samples; however, the wafer will be diced in a way that each device will contain multiple samples. The operating range of the resonators will be broader in this case and it may make the observations in bio-experiments easier.

## 4. CONCLUSIONS

In summary, in section 2, the modeling and the experimental characterization results were presented for rectangular split-ring resonators with a single split and two-splits, which operate at microwave frequencies between 0 and 5 GHz. Different excitation conditions are imposed on the resonators that result in different resonance behavior. The orientation of the electric and the magnetic field determines the resonant mode and the frequency as explained with electromagnetic simulations. Magnetic resonance was observed as a result of magnetic field perpendicular to the plane of the resonator. This induces a circulating current pattern along the conductor of the resonator. A similar current pattern is obtained when the electric field is polarized along with the gap of the resonator. A different mode of magnetic resonance was also observed when the electric field is along with the short side of the resonator. In this case, two different current paths with opposing current directions are present in bottom and top halves of the resonator. The rectangular shape of the resonators supports this mode of operation where two virtual nodes are defined along the gap of the resonator. It is shown that the presence of the node and the paths of circulating current are the same for the two-splits resonator with identical excitation conditions. The second split of the resonator was placed exactly at the second node so that the circulating current path is not altered. So, the magnetic resonance behavior of the resonators is the same regardless of the splits on the structure for a certain excitation condition. The resonators were fabricated on an FR4 substrate for experimental characterization and a pair of monopole antennas was used to excite the resonators. The results of the simulations verify the experiments. The results are in good agreement with a maximum deviation of 19% between the values of resonant frequencies. Experimental results show that the presented devices can effectively function as frequency selective media for varying excitation conditions.

In section 3, the design, simulation, fabrication, and characterization of the rectangular split-ring resonators operating at THz frequencies were presented. Five different types of rectangular split-ring resonators that operate between 0-3 THz were

designed. Similar to section 2, simulation results for different orientations of the electric and magnetic fields were obtained and discussed for each sample. Then three different types of devices were fabricated. In the first type of devices, split-ring resonators are made of copper and are patterned on a Silicon substrate. In the second type of devices, split-ring resonators are made of copper and patterned on a substrate of parylene and Silicon. However, in the third type of devices, the split-ring resonators are made of titanium and are patterned on substrate of parylene and Silicon. The fabricated samples were characterized in the transmission mode of a terahertz time domain spectroscopy. The experiment results were compared to the simulation results mostly for the excitations where the wave vector is perpendicular to the plane of the resonators. For the first type of devices, the experiment results were extracted by characterizing each designed samples individually. By comparing the corresponding simulation results and the experiment results, it can be stated that they are in a good agreement and the maximum deviation is 35.1%. The deviations between the simulation and the experiment results are due to several reasons. First, the simulation results in CST Studio are done in the most simplified case where the substrate is vacuum, whereas the actual substrate is Silicon. Second, electric and magnetic fields of the experiment setup are not controllable. Third, there are defects in the fabricated mask and also defects in the fabricated devices. These parameters lead to the deviations. Designed samples were again characterized individually in the second type of fabricated devices. By comparing the experiment result and the corresponding simulation results in this case, additional frequencies in sample three and sample four can be seen. It is believed that the additional frequencies are coming from the possibly trapped molecules in the parylene or are coming from the setup. The maximum deviation in this case is 51.25%. Therefore, in addition to the previously mentioned reasons for the difference in the simulation and experiment results, molecules being trapped over time or in the fabrication process by the parylene layer lead to additional errors. For the third type of the devices several of the designed samples were characterized at the same time. It means that the wafer was diced in larger pieces so that it contained multiple numbers of samples. Afterwards the whole piece of the chosen device was illuminated. By observing the experiment graphs, it can be deduced that the obtained experiment

result is the superposition of the frequency response of the individual samples present on the diced piece. Also, an extra layer of parylene was deposited on some of the samples and the samples were characterized afterwards. It can be inferred that additional layer of the parylene on the split-ring resonators affected the experiment results due to Fabry-Perot interference and also made one of the resonances more pronounced in the measured device. Bio-experiments for one of the samples in the second type of the fabricated devices were also done. The sample was characterized at first and then was dipped in a high-concentration solution of the glucose in DI water. After getting dried, it was characterized again. It can be stated that glucose shifted the second frequency by 42.86% and the value of the shift is 0.18 THz. Experimental results show that the presented devices have the potential to effectively function as biosensors in the future.

## REFERENCES

1. Shalaev, V. M., “Optical negative-index metamaterials”, *Nature photonics*, Vol. 1, No. 1, pp. 41–48, 2007.
2. Shelby, R. A., D. R. Smith and S. Schultz, “Experimental verification of a negative index of refraction”, *science*, Vol. 292, No. 5514, pp. 77–79, 2001.
3. Pendry, J. B., A. J. Holden, D. Robbins and W. Stewart, “Magnetism from conductors and enhanced nonlinear phenomena”, *IEEE transactions on microwave theory and techniques*, Vol. 47, No. 11, pp. 2075–2084, 1999.
4. Soukoulis, C. M., S. Linden and M. Wegener, “Negative refractive index at optical wavelengths”, *Science*, Vol. 315, No. 5808, pp. 47–49, 2007.
5. Pendry, J. B., D. Schurig and D. R. Smith, “Controlling electromagnetic fields”, *science*, Vol. 312, No. 5781, pp. 1780–1782, 2006.
6. Schurig, D., J. Mock, B. Justice, S. A. Cummer, J. B. Pendry, A. Starr and D. Smith, “Metamaterial electromagnetic cloak at microwave frequencies”, *Science*, Vol. 314, No. 5801, pp. 977–980, 2006.
7. Pendry, J. B., “Negative refraction makes a perfect lens”, *Physical review letters*, Vol. 85, No. 18, p. 3966, 2000.
8. Smolyaninov, I. I., Y.-J. Hung and C. C. Davis, “Magnifying superlens in the visible frequency range”, *Science*, Vol. 315, No. 5819, pp. 1699–1701, 2007.
9. Liu, Z., H. Lee, Y. Xiong, C. Sun and X. Zhang, “Far-field optical hyperlens magnifying sub-diffraction-limited objects”, *science*, Vol. 315, No. 5819, pp. 1686–1686, 2007.

10. Gokhale, V. J., O. A. Shenderova, G. E. McGuire and M. Rais-Zadeh, “Infrared absorption properties of carbon nanotube/nanodiamond based thin film coatings”, *Journal of Microelectromechanical Systems*, Vol. 23, No. 1, pp. 191–197, 2014.
11. Hong, J., D. Park, J. Yim, J. Park, J.-Y. Park, S. Lee and Y. Ahn, “Dielectric constant engineering of single-walled carbon nanotube films for metamaterials and plasmonic devices”, *The Journal of Physical Chemistry Letters*, Vol. 4, No. 22, pp. 3950–3957, 2013.
12. Chen, T., S. Li and H. Sun, “Metamaterials application in sensing”, *Sensors*, Vol. 12, No. 3, pp. 2742–2765, 2012.
13. Chang, Y.-T., Y.-C. Lai, C.-T. Li, C.-K. Chen and T.-J. Yen, “A multi-functional plasmonic biosensor”, *Optics express*, Vol. 18, No. 9, pp. 9561–9569, 2010.
14. Torun, H., F. C. Top, G. Dundar and A. Yalcinkaya, “An antenna-coupled split-ring resonator for biosensing”, *Journal of Applied Physics*, Vol. 116, No. 12, p. 124701, 2014.
15. Park, S., J. Hong, S. Choi, H. Kim, W. Park, S. Han, J. Park, S. Lee, D. Kim and Y. Ahn, “Detection of microorganisms using terahertz metamaterials”, *Scientific reports*, Vol. 4, 2014.
16. Debus, C. and P. H. Bolivar, “Frequency selective surfaces for high sensitivity terahertz sensing”, *Applied Physics Letters*, Vol. 91, No. 18, p. 184102, 2007.
17. Smith, D. R., J. B. Pendry and M. C. Wiltshire, “Metamaterials and negative refractive index”, *Science*, Vol. 305, No. 5685, pp. 788–792, 2004.
18. Sydoruk, O., E. Tatartschuk, E. Shamonina and L. Solymar, “Analytical formulation for the resonant frequency of split rings”, *Journal of Applied Physics*, Vol. 105, No. 1, p. 014903, 2009.

19. Veselago, V. G., “The electrodynamics of substances with simultaneously negative values of  $\epsilon$  and  $\mu$ ”, *Soviet physics uspekhi*, Vol. 10, No. 4, p. 509, 1968.
20. Smith, D. R., W. J. Padilla, D. Vier, S. C. Nemat-Nasser and S. Schultz, “Composite medium with simultaneously negative permeability and permittivity”, *Physical review letters*, Vol. 84, No. 18, p. 4184, 2000.
21. Shelby, R., D. Smith, S. Nemat-Nasser and S. Schultz, “Microwave transmission through a two-dimensional, isotropic, left-handed metamaterial”, *Applied Physics Letters*, Vol. 78, No. 4, pp. 489–491, 2001.
22. Pendry, J., A. Holden, D. Robbins and W. Stewart, “Low frequency plasmons in thin-wire structures”, *Journal of Physics: Condensed Matter*, Vol. 10, No. 22, p. 4785, 1998.
23. Al-Naib, I. A. I., C. Jansen and M. Koch, “Thin-film sensing with planar asymmetric metamaterial resonators”, *Applied Physics Letters*, Vol. 93, No. 8, p. 083507, 2008.
24. Kafesaki, M., T. Koschny, R. Penciu, T. Gundogdu, E. Economou and C. M. Soukoulis, “Left-handed metamaterials: detailed numerical studies of the transmission properties”, *Journal of Optics A: Pure and Applied Optics*, Vol. 7, No. 2, p. S12, 2005.
25. Penciu, R., K. Aydin, M. Kafesaki, T. Koschny, E. Ozbay, E. Economou and C. Soukoulis, “Multi-gap individual and coupled split-ring resonator structures”, *Optics express*, Vol. 16, No. 22, pp. 18131–18144, 2008.
26. Aydin, K., I. Bulu, K. Guven, M. Kafesaki, C. M. Soukoulis and E. Ozbay, “Investigation of magnetic resonances for different split-ring resonator parameters and designs”, *New journal of physics*, Vol. 7, No. 1, p. 168, 2005.
27. Pacheco, J., *Theory and application of left-handed metamaterials*, Ph.D. Thesis,

Massachusetts Institute of Technology, 2004.

28. Rohde, U. L. and A. K. Poddar, “Metamaterial Resonators: Theory and Applications”, *MICROWAVE JOURNAL*, Vol. 57, No. 12, pp. 74–+, 2014.
29. Bai, Y., L. Zhao, D. Ju, Y. Jiang and L. Liu, “Wide-angle, polarization-independent and dual-band infrared perfect absorber based on L-shaped metamaterial”, *Optics express*, Vol. 23, No. 7, pp. 8670–8680, 2015.
30. Linden, S., C. Enkrich, M. Wegener, J. Zhou, T. Koschny and C. M. Soukoulis, “Magnetic response of metamaterials at 100 terahertz”, *Science*, Vol. 306, No. 5700, pp. 1351–1353, 2004.
31. Enkrich, C., M. Wegener, S. Linden, S. Burger, L. Zschiedrich, F. Schmidt, J. Zhou, T. Koschny and C. Soukoulis, “Magnetic metamaterials at telecommunication and visible frequencies”, *Physical review letters*, Vol. 95, No. 20, p. 203901, 2005.
32. Rockstuhl, C., F. Lederer, C. Etrich, T. Zentgraf, J. Kuhl and H. Giessen, “On the reinterpretation of resonances in split-ring-resonators at normal incidence”, *Optics express*, Vol. 14, No. 19, pp. 8827–8836, 2006.
33. Klein, M. W., M. Wegener, N. Feth and S. Linden, “Experiments on second- and third-harmonic generation from magnetic metamaterials”, *Optics Express*, Vol. 15, No. 8, pp. 5238–5247, 2007.
34. Siegel, P. H. *et al.*, “Terahertz technology”, *IEEE Transactions on microwave theory and techniques*, Vol. 50, No. 3, pp. 910–928, 2002.
35. Chau, K. J., *Terahertz Time-Domain Spectroscopy of Metallic Particle Ensembles*, INTECH Open Access Publisher, 2010.
36. Federici, J. F., B. Schulkin, F. Huang, D. Gary, R. Barat, F. Oliveira and D. Zimdars, “THz imaging and sensing for security applications—explosives, weapons and

- drugs”, *Semiconductor Science and Technology*, Vol. 20, No. 7, p. S266, 2005.
37. Federici, J. F., D. Gary, R. Barat and D. Zimdars, “THz standoff detection and imaging of explosives and weapons”, *Defense and Security*, pp. 75–84, International Society for Optics and Photonics, 2005.
  38. Pawar, A. Y., D. D. Sonawane, K. B. Erande and D. V. Derle, “Terahertz technology and its applications”, *Drug Invention Today*, Vol. 5, No. 2, pp. 157–163, 2013.
  39. Berry, E., “Risk perception and safety issues”, *Journal of biological physics*, Vol. 29, No. 2, pp. 263–267, 2003.
  40. Savvas, M., *Characterization of terahertz bi-material sensors with integrated metamaterial absorbers*, Ph.D. Thesis, Monterey, California: Naval Postgraduate School, 2013.
  41. Stoik, C. D., M. J. Bohn and J. L. Blackshire, “Nondestructive evaluation of aircraft composites using transmissive terahertz time domain spectroscopy”, *Optics express*, Vol. 16, No. 21, pp. 17039–17051, 2008.
  42. Zhong, H., J. Xu, X. Xie, T. Yuan, R. Reightler, E. Madaras and X.-C. Zhang, “Nondestructive defect identification with terahertz time-of-flight tomography”, *IEEE Sensors Journal*, Vol. 5, No. 2, pp. 203–208, 2005.
  43. King, M. D., W. D. Buchanan and T. M. Korter, “Identification and quantification of polymorphism in the pharmaceutical compound diclofenac acid by terahertz spectroscopy and solid-state density functional theory”, *Analytical chemistry*, Vol. 83, No. 10, pp. 3786–3792, 2011.
  44. Kemp, M. C., P. Taday, B. E. Cole, J. Cluff, A. J. Fitzgerald and W. R. Tribe, “Security applications of terahertz technology”, *AeroSense 2003*, pp. 44–52, International Society for Optics and Photonics, 2003.

45. Lu, M., J. Shen, N. Li, Y. Zhang, C. Zhang, L. Liang and X. Xu, "Detection and identification of illicit drugs using terahertz imaging", *Journal of Applied Physics*, Vol. 100, No. 10, p. 103104, 2006.
46. Gowen, A., C. O'Sullivan and C. O'Donnell, "Terahertz time domain spectroscopy and imaging: emerging techniques for food process monitoring and quality control", *Trends in Food Science & Technology*, Vol. 25, No. 1, pp. 40–46, 2012.
47. Han, P., G. Cho and X.-C. Zhang, "Time-domain transillumination of biological tissues with terahertz pulses", *Optics Letters*, Vol. 25, No. 4, pp. 242–244, 2000.
48. Oh, S. J., J. Kang, I. Maeng, J.-S. Suh, Y.-M. Huh, S. Haam and J.-H. Son, "Nanoparticle-enabled terahertz imaging for cancer diagnosis", *Optics express*, Vol. 17, No. 5, pp. 3469–3475, 2009.
49. Chen, H., T.-H. Chen, T.-F. Tseng, J.-T. Lu, C.-C. Kuo, S.-C. Fu, W.-J. Lee, Y.-F. Tsai, Y.-Y. Huang, E. Y. Chuang *et al.*, "High-sensitivity in vivo THz transmission imaging of early human breast cancer in a subcutaneous xenograft mouse model", *Optics express*, Vol. 19, No. 22, pp. 21552–21562, 2011.
50. Tao, H., A. C. Strikwerda, K. Fan, W. J. Padilla, X. Zhang and R. D. Averitt, "MEMS based structurally tunable metamaterials at terahertz frequencies", *Journal of Infrared, Millimeter, and Terahertz Waves*, Vol. 32, No. 5, pp. 580–595, 2011.
51. Alves, F., D. Grbovic, B. Kearney, N. V. Lavrik and G. Karunasiri, "Bi-material terahertz sensors using metamaterial structures", *Optics express*, Vol. 21, No. 11, pp. 13256–13271, 2013.
52. Zhao, X., K. Fan, J. Zhang, H. R. Seren, G. D. Metcalfe, M. Wraback, R. D. Averitt and X. Zhang, "Optically tunable metamaterial perfect absorber on highly flexible substrate", *Sensors and Actuators A: Physical*, Vol. 231, pp. 74–80, 2015.

53. TYDEX, *THz Materials*, 2016, [http://www.tydexoptics.com/pdf/THz\\_Materials.pdf](http://www.tydexoptics.com/pdf/THz_Materials.pdf), accessed on July 2016.
54. Lewis, R. A., *Terahertz physics*, Cambridge University Press, 2012.
55. Danylov, A., “THz laboratory measurements of atmospheric absorption between 6% and 52% relative humidity”, *Submillimeter-Wave Technology Laboratory University of Massachusetts Lowell*, Vol. 175, 2006.
56. Topsakal, E., T. Karacolak and E. C. Moreland, “Glucose-dependent dielectric properties of blood plasma”, *General Assembly and Scientific Symposium, 2011 XXXth URSI*, pp. 1–4, IEEE, 2011.
57. Upadhyaya, P., Y. Shen, A. Davies and E. Linfield, “Terahertz time-domain spectroscopy of glucose and uric acid”, *Journal of Biological Physics*, Vol. 29, No. 2-3, pp. 117–121, 2003.
58. Lee, D.-K., J.-H. Kang, J.-S. Lee, H.-S. Kim, C. Kim, J. H. Kim, T. Lee, J.-H. Son, Q.-H. Park and M. Seo, “Highly sensitive and selective sugar detection by terahertz nano-antennas”, *Scientific reports*, Vol. 5, 2015.

## APPENDIX A: LAYOUTS AND DETAILED SIMULATIONS RESULTS

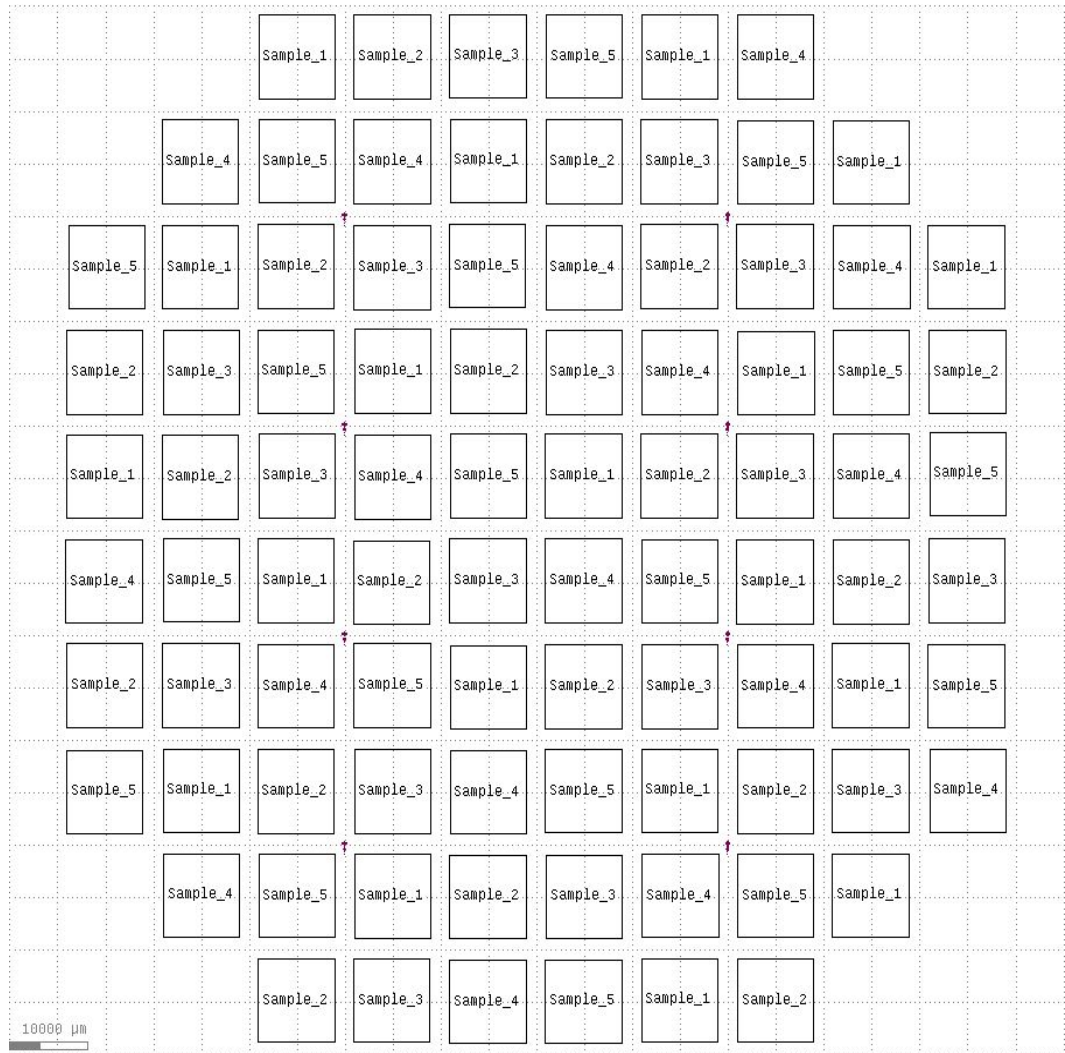


Figure A.1. The layout of the designed mask.

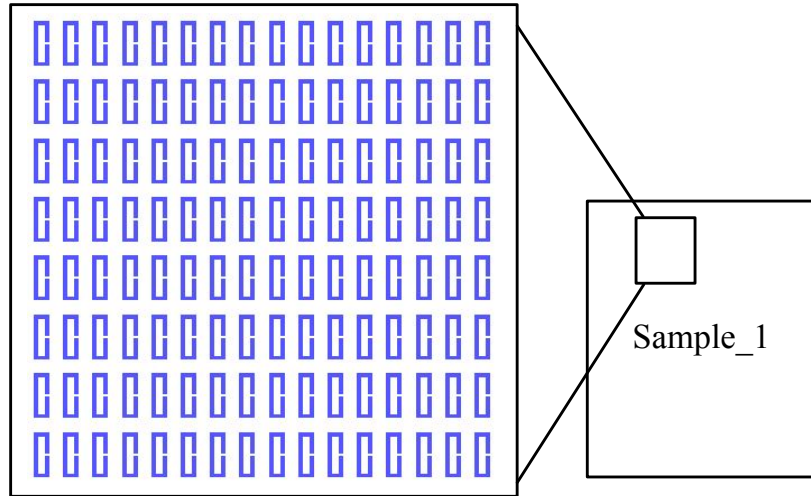


Figure A.2. The layout of the dies containing sample one.

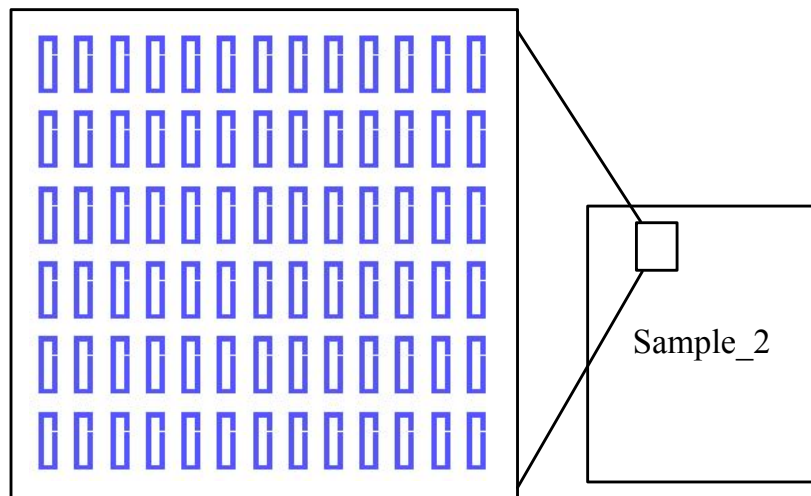


Figure A.3. The layout of the dies containing sample two.

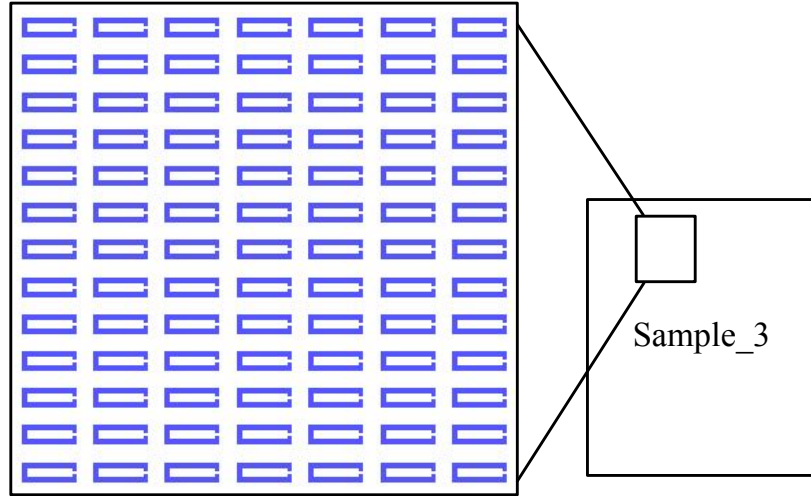


Figure A.4. The layout of the dies containing sample three.

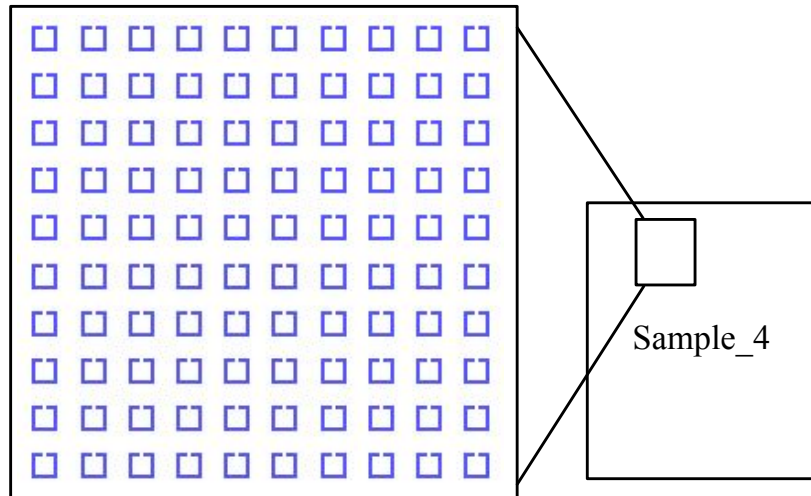


Figure A.5. The layout of the dies containing sample four.

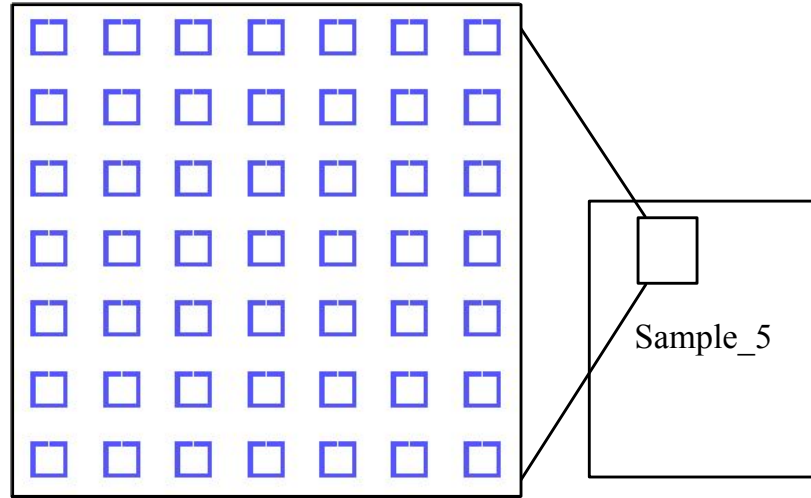


Figure A.6. The layout of the dies containing sample five.

### A.1. Detailed Simulation Results for Sample One

Figures below show the simulation results of the designed samples in section 3 with more details. The distribution of the current density for magnetic resonances, and the distribution of the electric field for electric resonances are presented respectively.

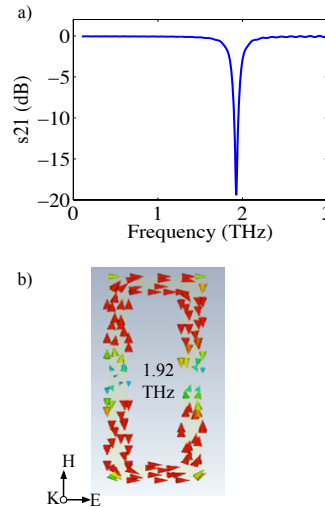


Figure A.7. a)  $s_{21}$  Spectrum of the sample one for the excitation setting shown in the figure. b) Distribution of current density at 1.92 THz.

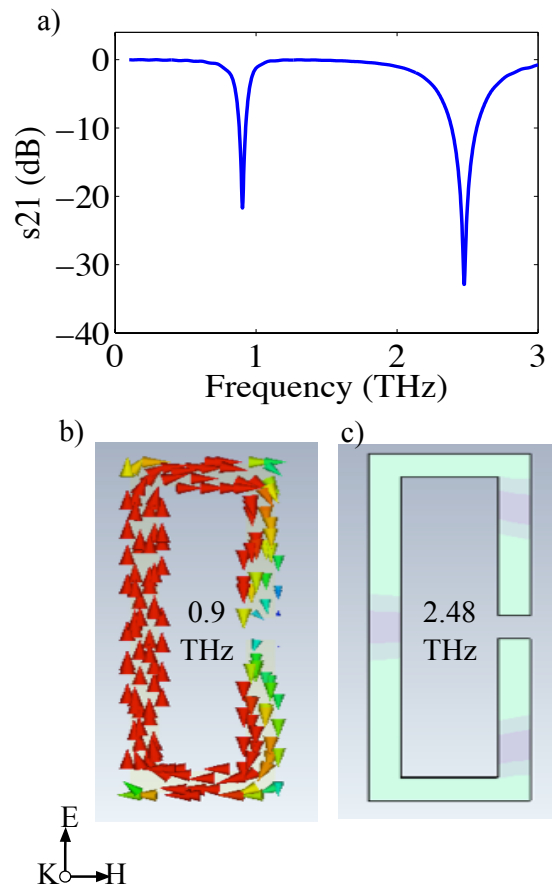


Figure A.8. a)  $s_{21}$  Spectrum of the sample one for the excitation setting shown in the figure. b) Distribution of current density at 0.9 THz. c) Distribution of electric field at 2.48 THz.

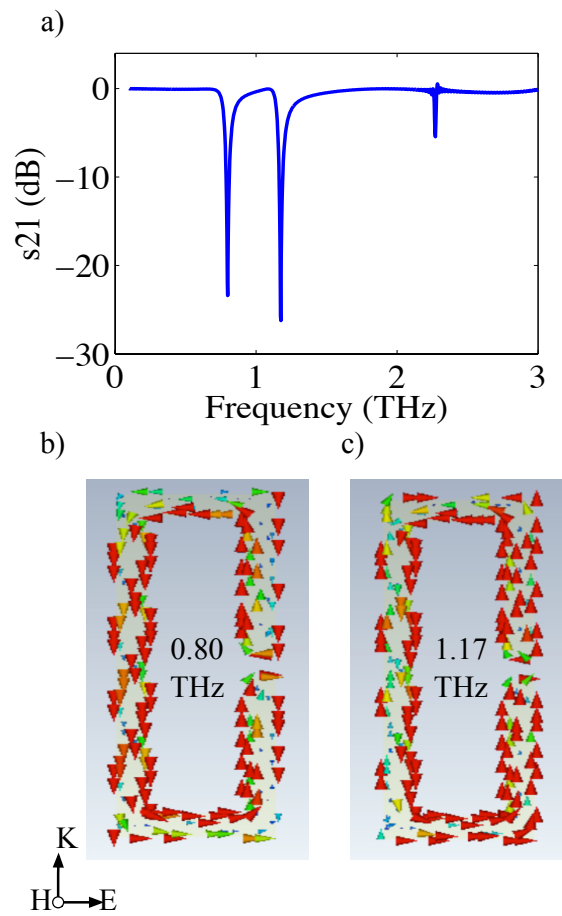


Figure A.9. a)  $s_{21}$  Spectrum of the sample one for the excitation setting shown in the figure. Distribution of current density at b) 0.8 THz and c) 1.17 THz.

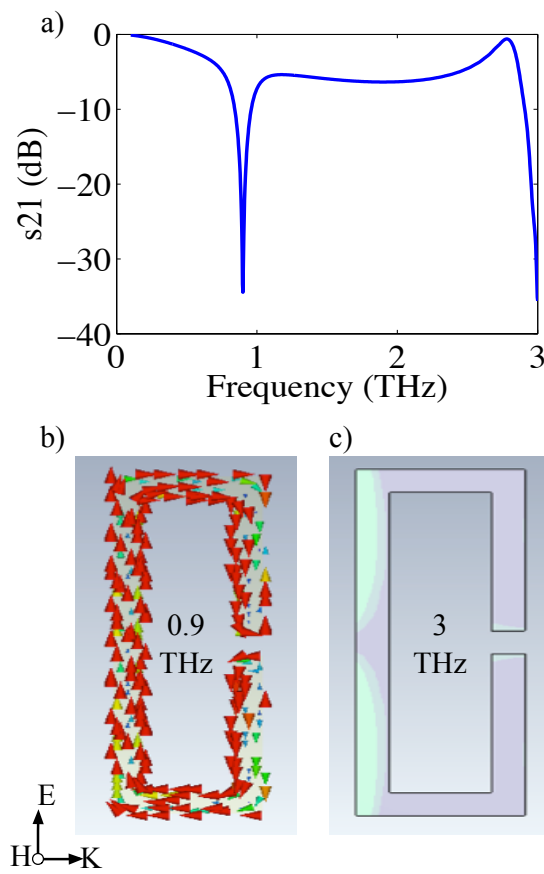


Figure A.10. a)  $s_{21}$  Spectrum of the sample one for the excitation setting shown in the figure. b) Distribution of current density at 0.9 THz. c) Distribution of electric field at 3 THz.

### A.2. Detailed Simulation Results for Sample Two

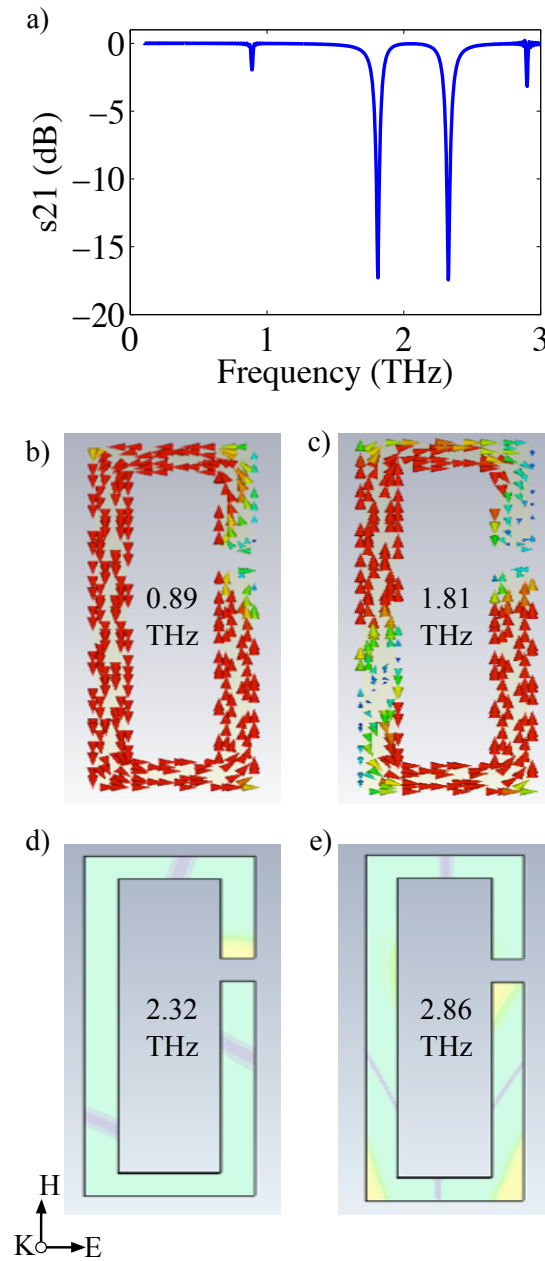


Figure A.11. a)  $s_{21}$  Spectrum of the sample two for the excitation setting shown in the figure. Distribution of current density at b) 0.89 THz and c) 1.81 THz.

Distribution of electric field at d) 2.32 THz and e) 2.86 THz.

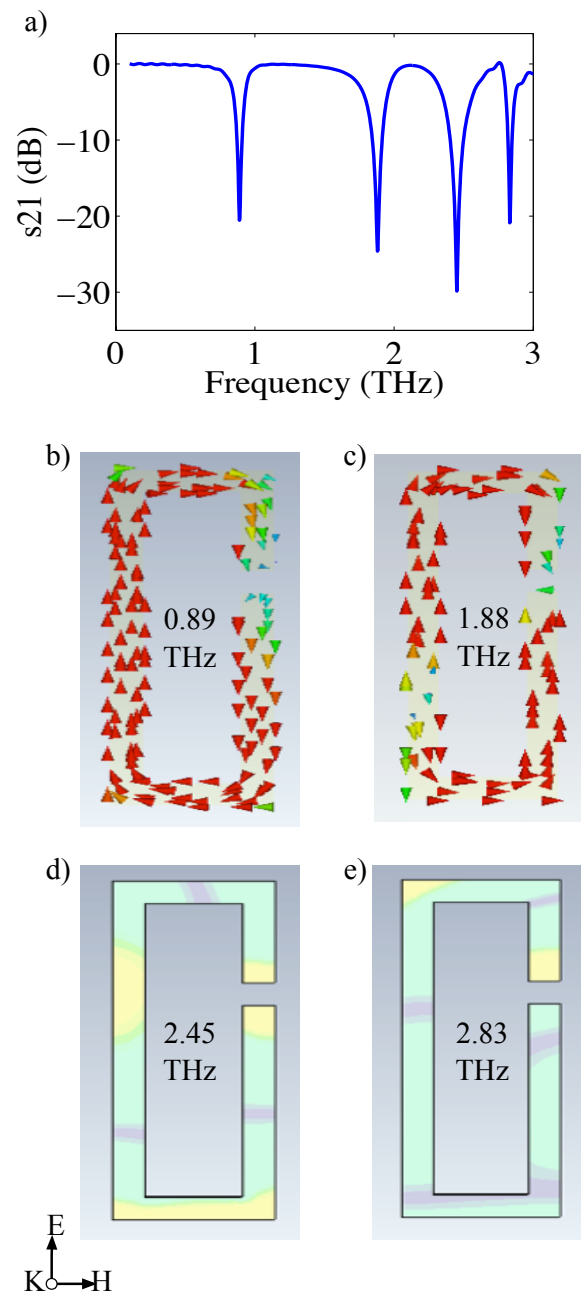


Figure A.12. a)  $s_{21}$  Spectrum of the sample two for the excitation setting shown in the figure. Distribution of current density at b) 0.89 THz and c) 1.88 THz. Distribution of electric field at d) 2.45 THz and e) 2.83 THz.

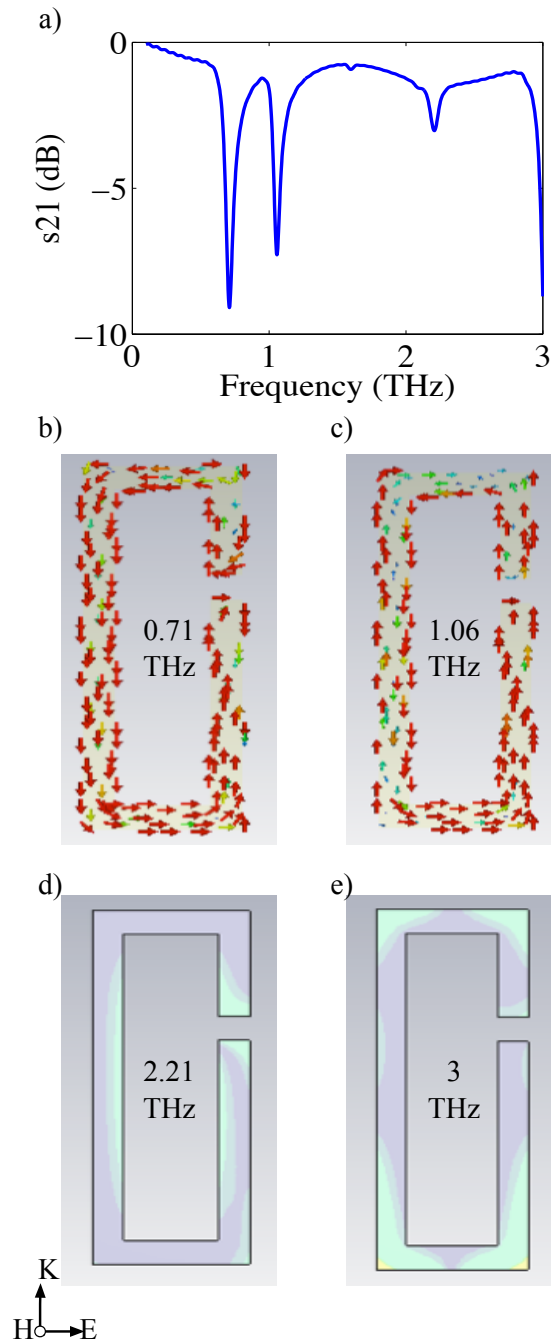


Figure A.13. a)  $s_{21}$  Spectrum of the sample two for the excitation setting shown in the figure. Distribution of current density at b) 0.71 THz, c) 1.06 THz. Distribution of electric field at d) 2.21 THz, e) 3 THz.

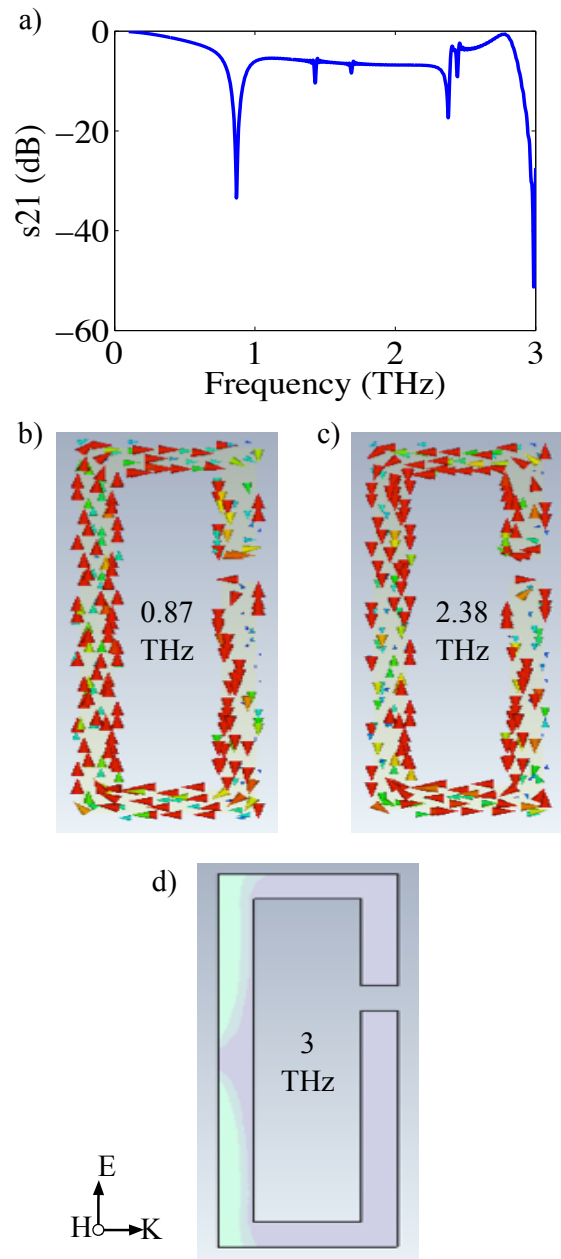


Figure A.14. a)  $s_{21}$  Spectrum of the sample two for the excitation setting shown in the figure. Distribution of current density at b) 0.87 THz and c) 2.38 THz. d) Distribution of electric field at 3 THz.

### A.3. Detailed Simulation Results for Sample Three

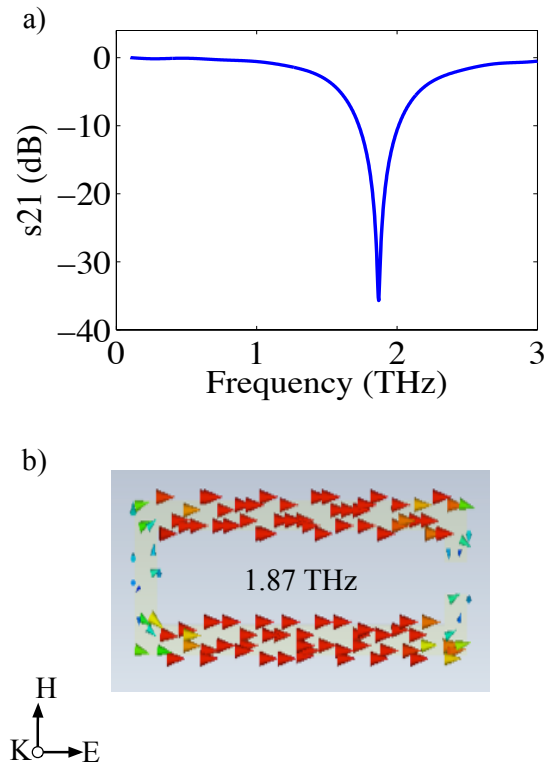


Figure A.15. a)  $s_{21}$  Spectrum of the sample three for the excitation setting shown in the figure. b) Distribution of current density at 1.87 THz.

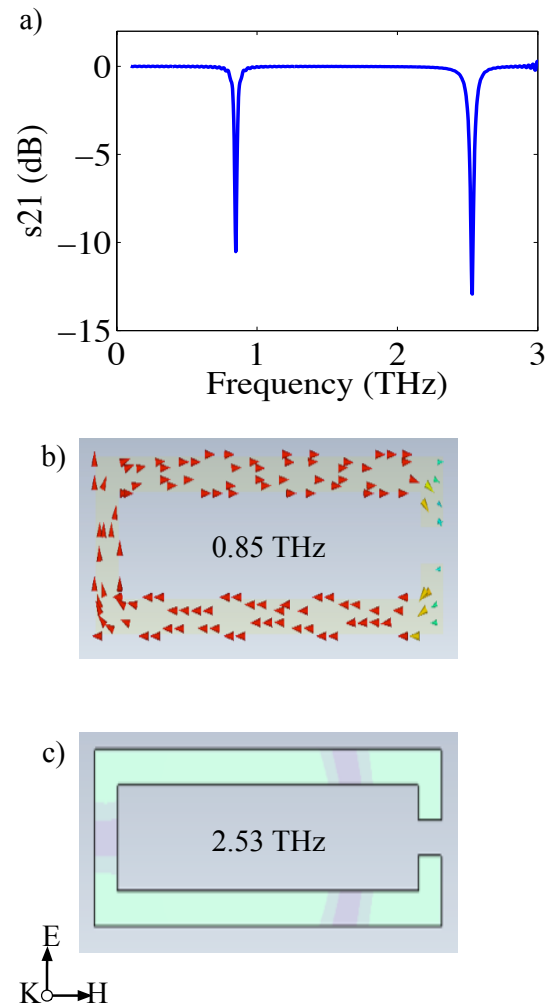


Figure A.16. a)  $s_{21}$  Spectrum of the sample three for the excitation setting shown in the figure. b) Distribution of current density at 0.85 THz. c) Distribution of electric field at 2.53 THz.

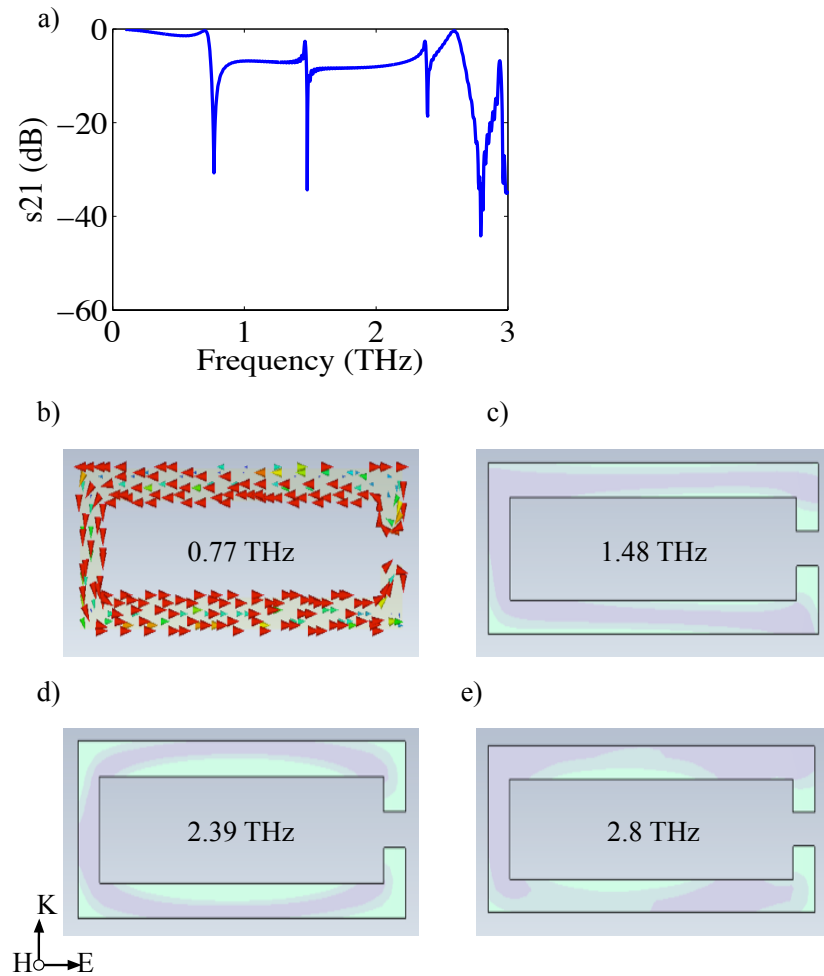


Figure A.17. a)  $s_{21}$  Spectrum of the sample three for the excitation setting shown in the figure. b) Distribution of current density at 0.77 THz. Distribution of electric field at c) 1.48 THz, d) 2.39 THz, and e) 2.8 THz.

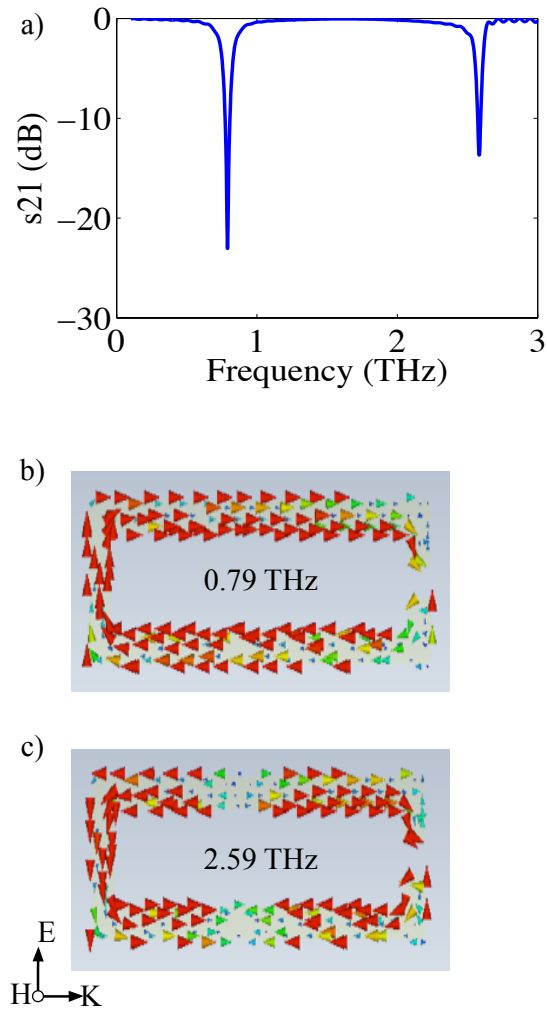


Figure A.18. a)  $s_{21}$  Spectrum of the sample three for the excitation setting shown in the figure. Distribution of current density at b) 0.79 THz and c) 2.59 THz.

#### A.4. Detailed Simulation Results for Sample Four

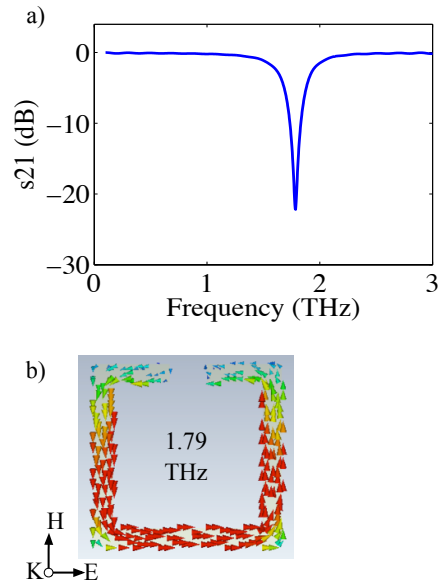


Figure A.19. a)  $s_{21}$  Spectrum of the sample four for the excitation setting shown in the figure. b) Distribution of current density at 1.79 THz.

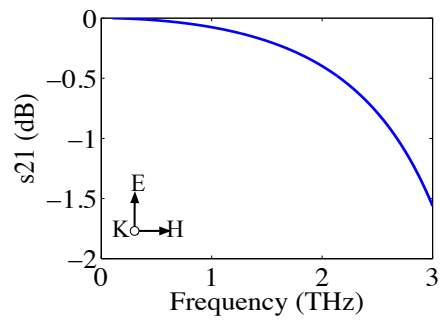


Figure A.20.  $s_{21}$  Spectrum of the sample four for the excitation setting shown in the figure.

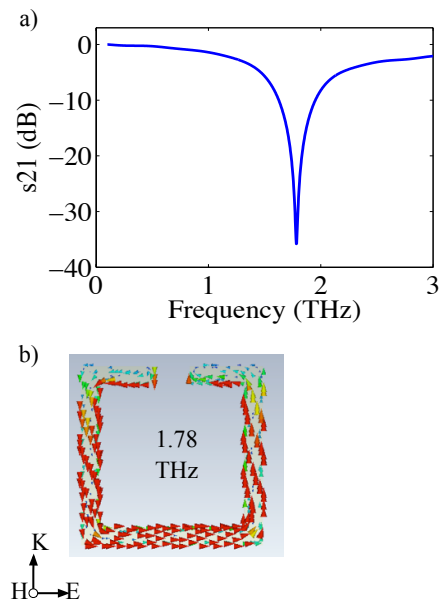


Figure A.21. a)  $s_{21}$  Spectrum of the sample four for the excitation setting shown in the figure. b) Distribution of current density at 1.78 THz.

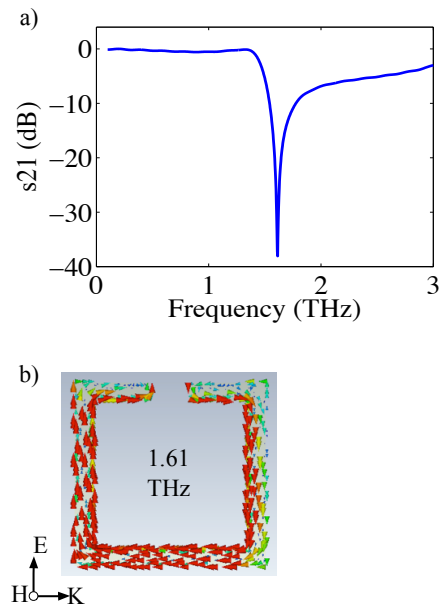


Figure A.22. a)  $s_{21}$  Spectrum of the sample four for the excitation setting shown in the figure. b) Distribution of current density at 1.61 THz.

### A.5. Detailed Simulation Results for Sample Five

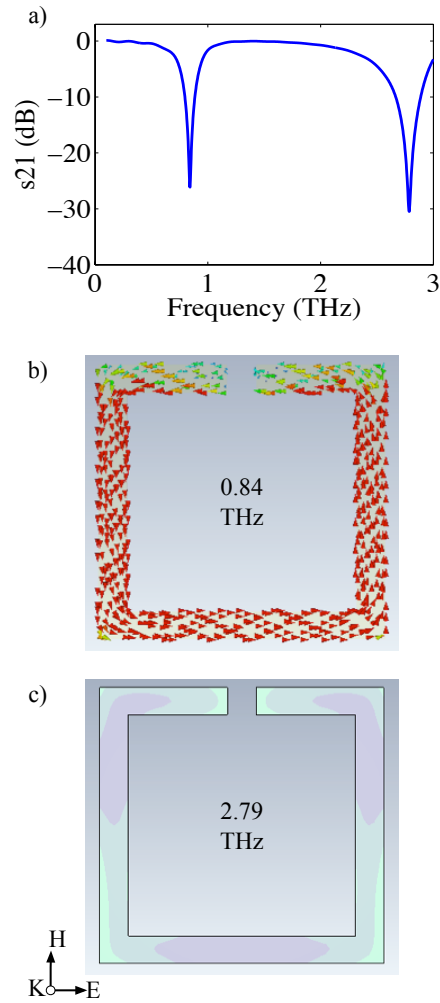


Figure A.23. a)  $s_{21}$  Spectrum of the sample five for the excitation setting shown in the figure. b) Distribution of current density at 0.84 THz. c) Distribution of electric field at 2.79 THz.

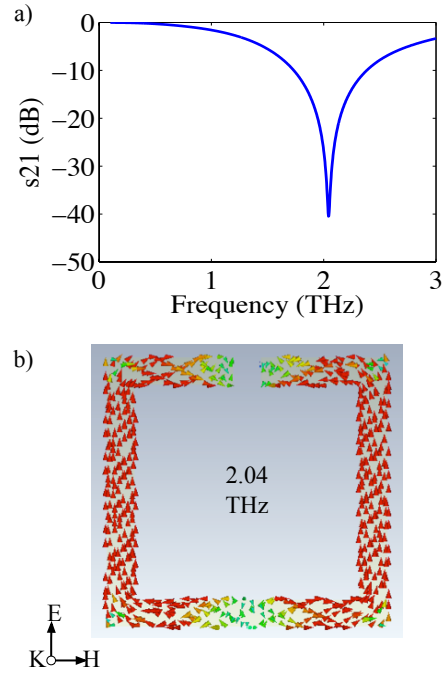


Figure A.24. a)  $s_{21}$  Spectrum of the sample five for the excitation setting shown in the figure. b) Distribution of current density at 2.04 THz.

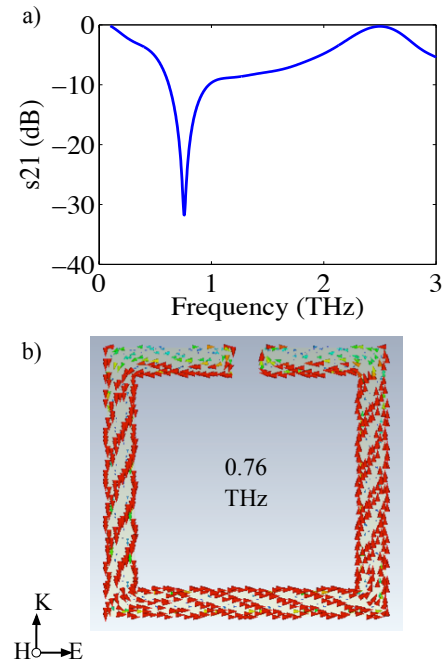


Figure A.25. a)  $s_{21}$  Spectrum of the sample five for the excitation setting shown in the figure. b) Distribution of current density at 0.76 THz.

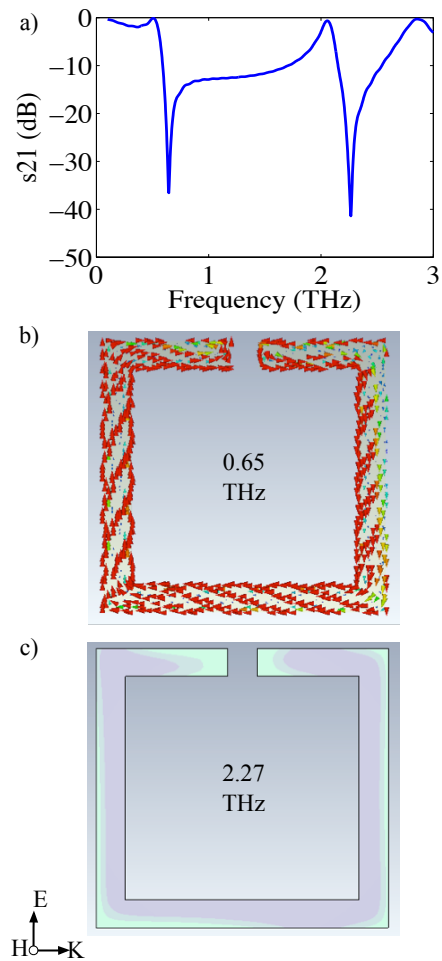


Figure A.26. a)  $s_{21}$  Spectrum of the sample five for the excitation setting shown in the figure. b) Distribution of current density at 0.65 THz. c) Distribution of electric field at 2.27 THz.